STUDIES OF IMAGE RECONSTRUCTION METHODS FOR ELECTRICAL IMPEDANCE TOMOGRAPHY

Submitted in partial fulfilment of the requirements
for the degree of Doctor of Philosophy in the
Faculty of Medicine, to the University of
Newcastle-upon-Tyne
by

C. J. Kotre
BSc.(ENG), MSc., ACGI, MIEE, C.Eng

March 1993

ABSTRACT

Electrical impedance tomography (EIT) is a technique in which images representing the cross-sectional distribution of electrical impedance within a three-dimensional object are reconstructed from measurements on the object surface. In this work, some developments of image reconstruction algorithms aimed at increasing the value of this technique in the field of medical diagnosis are studied.

The electrical properties of biological tissue and the possibilities for medical applications of EIT are first reviewed. The physical and mathematical basis for EIT is then examined with particular regard for the assumptions required. Following a review of published work on image reconstruction methods, a set of specifications thought useful to advance the utility of EIT as a clinical imaging modality is proposed, together with an approach to image reconstruction designed to fulfil these specifications. A series of computer simulations of the image reconstruction problem is then used to investigate the performance of this reconstruction approach on simple, known, impedance distributions, and to develop the method to the stage of a complete reconstruction algorithm. The algorithm is then tested on a series of data sets produced by measurements on a physical phantom, and on a set of measurements made on a volunteer human subject.

A mathematician, a scientist and an engineer were competing for the favours of the beautiful daughter of a professor of mathematics. Not approving of any of them, he stipulated that, while they may see his daughter, the distance that any of them would be allowed to move towards her at any time must be no greater than half the distance remaining. When informed of this constraint, the mathematician left immediately. The scientist, after experimentally performing a couple of moves left also. The engineer, however, stayed, saying to himself: "I'll get close enough.....".

(A joke told by one of my undergraduate lecturers,
and sometimes a surprisingly productive philosophy.)

CONTENTS

Page

1. Introduction to electrical impedance tomography

2. The reconstruction of electrical impedance tomograms

Page

3. The development of a computer simulation for electrical impedance tomography

4. Reconstruction algorithm development

Page

5. Reconstructions of physical phantom and in-vivo test data

6. Conclusions

List of Symbols

Symbol	Chapter	Meaning
a	5	Distance from first current drive electrode
b	5	Distance from second current drive electrode
A	3	Amplitude of resistivity perturbation
$B(f_u)$	4	Fourier transform of surface potential gradient distribution due to point perturbation
c	4	Normalised radial distance in image
d	5	Radius of hemispherical electrode
E	4	Rate of change of potential in U direction
f	4	Spatial frequency
f_u	4	Spatial frequency in U direction
f	2	Impressed current source distribution
F_{eq}	4	Local scale factor for equi-potential space transformation
F_{tp}	4	Local scale factor for true-position space transformation
F	2	Forward transformation matrix
F^{-1}	2	Inverse transformation matrix
G_x	3	Potential gradient in x direction
G_y	3	Potential gradient in y direction
$H(f)$	4	Fourier transform of point spread function
i	4	Position increment in radial direction
I	2,3,4,5	Current
I	2	X-ray intensity
I_0	2	Incident x-ray intensity
k	3,4	Multiplicative scale factor (continuous distribution)
k'	3	Multiplicative scale factor (discrete distribution)

Symbol	Chapter	Meaning
l	3,4,5	Index identifying plane of electrodes
m	2,3,4,5	Index identifying current drive electrode pair
n	2,3,4,5	Index identifying voltage sense electrode pair
N	1,5	Number of electrodes per plane
P	4	Amplitude of point spread function
P(x,y,z)	3,4,5	Pixel value distribution
q	2	Distance of point perturbation from boundary
r_{eq}	4	Radial distance in equi-resolution space
r_{or}	4	Radial distance in original image space
r_{tp}	4	Radial distance in true-position space
R	2,3,4	Logarithmic resistivity
R(x,y,z)	2,3,4	Discrete distribution of log resistivity
$\boldsymbol{R}$	2	Vector resistivity distribution
$\boldsymbol{R}_p$	2	Perturbed log resistivity distribution
$\boldsymbol{R}_r$	2	Reference log resistivity distribution
$S_{l,m,n,x,y,z}$	2,3,4,5	Sensitivity coefficient
S_{norm}	4,5,6	Normalised total sensitivity at point
S_{total}	4,5	Total sensitivity at point
U	2	Bounded volume of conductor
U	3	Transformed space direction
u	2	Volume of element within conductor
$V_{m,n}$	2	Surface voltage measurement
V(l,m,n)	3,4,5	Surface voltage measurement
V	2	Vector surface voltage distribution
W(f)	4	Filter function in frequency space
x	2,3,4,5	Cartesian coordinate

Symbol	Chapter	Meaning
x'	3	Rotated cartesian coordinate
x''	3	Rotated cartesian coordinate
x_p	3,4,5	x position of point perturbation
x_m	4	x position of minimum total sensitivity
y	2,3,4,5	Cartesian coordinate
y'	3	Rotated cartesian coordinate
y''	3	Rotated cartesian coordinate
y_p	3,4,5	y position of point perturbation
y_m	4	y position of minimum total sensitivity
z	2,3,4,5	Cartesian coordinate
$Z_{m,n}$	2,5	Mutual impedance
δ	2,3,4,5	A small change
ϵ_r	1	Relative permittivity (dielectric constant)
ρ	2	Resistivity
σ	2	Conductivity, conductivity distribution
$\sigma(x,y,z)$	2	Discrete conductivity distribution
τ	4,5	Wiener filter noise level parameter
Φ	2	Potential distribution
Φ_r	2	Reference potential distribution
Φ_p	2	Perturbed potential distribution
∇	2	Gradient operator

CHAPTER 1

INTRODUCTION TO ELECTRICAL IMPEDANCE TOMOGRAPHY

1.0 Introduction

The objective of electrical impedance tomography (EIT) is to reconstruct images which represent the cross-sectional spatial distribution of electrical impedance within a three-dimensional object from measurements on its surface. The application of this technique to medical imaging is the main driving force behind its development, but applications in geophysics (Dines and Lytle, 1981), archaeology (Barber and Brown, 1983), geophysics and industrial non-destructive testing have also been suggested. Parallels between the relationships which govern the physics of current flow in volume conductors and those which govern field behaviour in electrostatics, magnetostatics, fluid diffusion, heat flow, molecular diffusion and gravitation (Seagar et al, 1987b) suggest that solutions for the electrical impedance problem could find application in these areas also.

The introduction of increasingly sophisticated computing into medical imaging which started in the early 1970's has resulted in a great increase in the number of diagnostic imaging techniques commonly available. In the field of tomographic imaging specifically, the greatest advances have been the development of X-ray computed tomography (CT) (Hounsfield, 1973) and nuclear magnetic resonance imaging (Lauterbur, 1973). In their fully developed form these imaging modalities are capable of delivering images with high spatial resolution and sensitivity to their imaged parameters, but this does not imply that no other imaging modalities are desirable. Single photon emission computed tomography, for example, is capable of only modest spatial resolution, but is still a valuable tool because of the nature of the imaged parameter (spatial distribution of a radiopharmaceutical) which can be linked to the physiological function of a number of organs in the body. Thus poor quality images of parameters which are sensitive to local pathology can be complementary to high quality images which are able to demonstrate details of the anatomy. Due to the physics of current flow in volume conductors, EIT images would be expected to be difficult to reconstruct and of low spatial resolution, but because of the wide range of tissue impedances found within the body and the link between the dielectric properties of tissue and its structure at the cellular and even molecular level, EIT could still emerge as a valuable complementary imaging modality.

In this work, the basis of EIT will be examined with particular regard to the assumptions required, and published image reconstruction methods reviewed. A set of specifications thought useful to advance the utility of EIT as a clinical imaging modality will be proposed together with an approach to image reconstruction designed to fulfil these specifications, whilst remaining practicable in terms of computational effort. Computer simulations will be used to investigate this reconstruction approach and develop it to the stage of a complete reconstruction algorithm which will then be tested on physical phantom and in vivo data.

1.1 Electrical properties of biological tissue

To a first approximation, biological tissue can be said to comprise a densely packed distribution of cells surrounded by inter-cellular electrolyte and containing an intra-cellular electrolyte. Cell membranes are composed of a lipid bilayer with a thickness around 6 nm into which protein molecules are incorporated (Pethig, 1984) and tend to act in a capacitive manner. This leads to a variation in tissue bulk impedance with frequency as well as structure. At low frequencies, current cannot flow through the cellular membranes and the impedance of the tissue will depend largely on the proportions and distribution of the cells and on the size of the conductive pathways between them. At higher frequencies, a proportion of the current will flow through the cells so that the measured impedance will depend on the conductivities of both the inter- and intra-cellular electrolytes. This results in a general reduction in the bulk impedance of biological tissues with increasing frequency.

The magnitude of the reactive (capacitive) component of the impedance is governed by the relative permittivity (or dielectric constant), ϵ_r, of the tissue at the frequency being considered. Tissue relative permittivity decreases with frequency in three stages (figure 1.1), labelled α, β and γ dispersions (Schwan, 1957). The α dispersion (approximately 10Hz to 10kHz) is caused by electric field induced

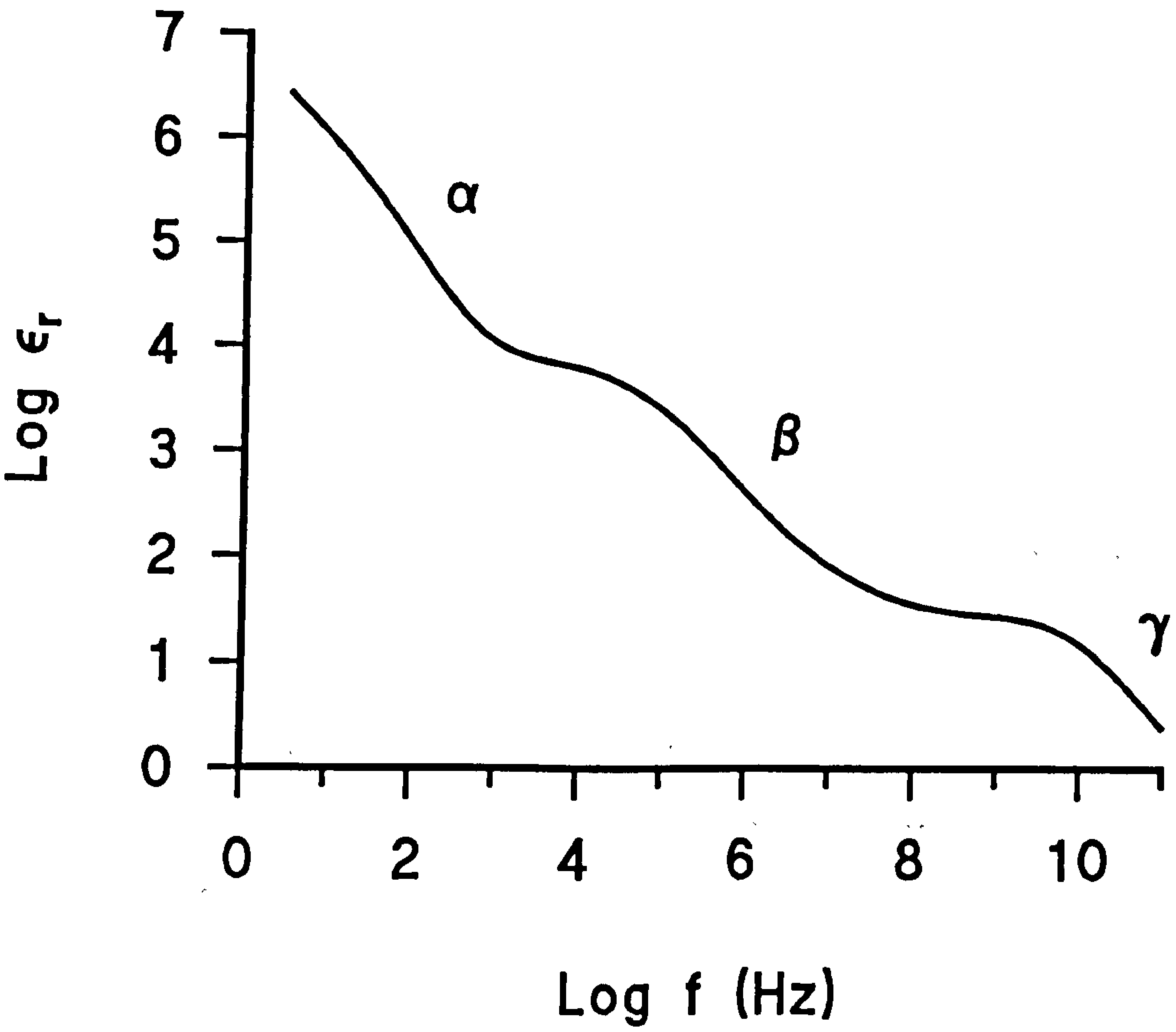

Figure 1.1

The variation of the relative permittivity with frequency for a typical biological tissue (after Schwan, 1957).

diffusions of ions and other charged species, the β dispersion (100 kHz to 10 MHz) is caused by the membrane capacitance progressively short-circuiting the membrane resistance, and the γ dispersion (1 to 100 GHz) is caused by the relaxation of the dipolar water molecules in the intra-cellular fluid. At the frequencies commonly employed for EIT, the conduction current is generally much greater than the displacement current, but the link between the permittivity of tissue and its physiological and physical properties has led to developments in multi-frequency and phase-sensitive EIT.

A further structural effect encountered particularly with skeletal muscle and to a lesser extent cardiac muscle is anisotropic resistivity. This is due to the cellular structure of the tissues consisting of long parallel fibres in one direction. Changes in bulk tissue resistivity with temperature of the order of 2% per °C (Conway, 1987) also contribute to the difficulties in obtaining reliable data on the electrical properties of biological tissue. Table 1.1 (reproduced from Barber and Brown, 1984) shows the result of a survey of published resistivity values for mammalian tissues. Due to the various complicating factors outlined above, the values would be expected to include significant errors, but the data does show that the range of tissues of interest are clearly separated on a scale of resistivity. This implies that good tissue contrast should be possible in EIT imaging.

Changes in the conductive and dielectric properties of various biological tissues with physiological changes have been reported by a number of authors.

Changes in the resistivity of canine lung tissue during respiration were measured by Witsoe and Kinnen (1967). They found the changes to be relatively large and linearly related to lung air volume.

Changes in resistivity between moving and stationary blood have been reported (Frewer, 1972), although the effect is not significant above very low flow rates making the use of EIT unlikely for blood flow measurements using this effect. The resistivity of blood also depends on its composition in terms of haematocrit content (Hill and Thompson, 1975).

In the brain, changes in the bulk impedance of the cerebral cortex have been correlated with the onset of brain oedema (Fujita et al, 1972). This is thought to be caused by fluid accumulation in the extra-cellular space of the white matter. Since it is known that small impedance changes result from neuronal discharges in the brain, the idea of mapping areas of neural activity with EIT is very attractive although the changes are probably too small to detect with present technology

Tissue	Resistivity (Ωm)
Cerebro-spinal fluid	0.65
Blood	1.5
Liver	3.5
Skeletal muscle	1.25 (longitudinal) 18.0 (transverse)
Cardiac muscle	1.6 (longitudinal) 4.3 (transverse)
Neural tissue	5.8
Grey matter	2.84
White matter	6.82
Lung	7.2 (expiration) 23.6 (inspiration)
Fat	27.2
Bone	166.0

Table 1.1

A survey of published resistivity values for mammalian tissue, reproduced from Barber (1989).

(Holder and Gardner-Medwin, 1988).

Changes in the low-frequency dielectric properties of a range of tissues with time following death have been observed (Surowiec et al, 1985) and an application of this effect to assess the degree of myocardial ischemia to the arrested and bypassed heart during surgery has been suggested (Gersing et al, 1983).

The impedance of breast tissue has been shown to be changed by the presence of a tumour (Fricke and Morse, 1926; Singh et al, 1979). As the highly vascularised tissue surrounding a breast tumour will have a low resistivity with respect to the avascular tissue of the tumour, good contrast in the spatial distribution of electrical impedance in a true plane through the tumour might be expected.

1.2 Electrical safety considerations

As well as the passive electrical properties of biological tissue which form the parameter to be imaged in EIT, it is also necessary to consider the possible hazard posed by the technique in terms of the stimulation of irritable tissues. The threshold of sensation for low frequency currents applied via skin surface electrodes is known to increase with frequency due to the relationship between the current density required for stimulation and the duration of the stimulus (Geddes and Baker, 1975). To avoid stimulation, frequencies in excess of 20 kHz are normally employed. In this frequency range, the current density required to cause neural stimulation is such that heating of the tissue is the dominant biological effect. The British Standard relating to the safety of medical electrical equipment, BS5724 (British Standards Institute, 1989) allows a patient auxiliary current (in milliamperes) of 0.1 times the frequency in kHz up to a limit of 10 mA. The same limit appears in a number of other national and international standards (Ghahary, 1990).

This current limitation is important not only from the safety point of view, but also because it governs the signal-to-noise ratio of the data obtained for any given measurement strategy and therefore sets a fundamental limit for the imaging performance of EIT applied to medical imaging.

1.3 The four-electrode impedance measurement method

To produce data related to the impedance distribution within the body it is necessary to inject currents via skin surface electrodes or induce currents by suitable magnetic fields. Although the latter approach has been reported (Purvis et al, 1990; Scaife et al, 1990; Gençer et al, 1992), the much more common technique of injecting a constant amplitude alternating current between pairs of skin surface ECG-type electrodes will be used in this work.

The skin surface electrode forms a transducer between ionic current flow in tissue and electronic flow in the measuring system. Various equivalent circuits for the electrode-skin interface have been suggested (Rabbat, 1990), all of which exhibit a fall of impedance with frequency. Above about 100 kHz the effects of stray capacitances in the measurement equipment will tend to become significant, so measurements in the 20 - 50 kHz region are most commonly employed. Even at these frequencies, however, the magnitude of the electrode impedance is likely to be similar to that of the impedance to be measured. It is therefore necessary to use a four-electrode approach to minimise the effect of electrode impedances.

The four-electrode method applied to EIT is illustrated in figure 1.2 which shows a body section around which a number of skin surface electrodes have been attached. To make an impedance measurement, a constant current is injected via one pair of electrodes while a voltage measurement is made at another pair using a high impedance voltmeter. For an ideal constant current generator and infinitely high impedance voltmeter, the measurement will be independent of the electrode contact impedances. The four-electrode method derives from the non-imaging technique of electrical impedance plethysmography in which the constant current is applied along the length of a segment of body extremity by an outer pair of band electrodes and the voltage measurement is made between an inner pair (Geddes and Baker, 1975).

1.4 Data collection strategies

Clearly, in EIT with typically 16 electrodes around the body segment to be imaged, there are a large number of current drive and voltage sense configurations possible. To exploit the advantage of relative insensitivity to electrode contact impedance offered by the four-electrode method, it is necessary to restrict voltage

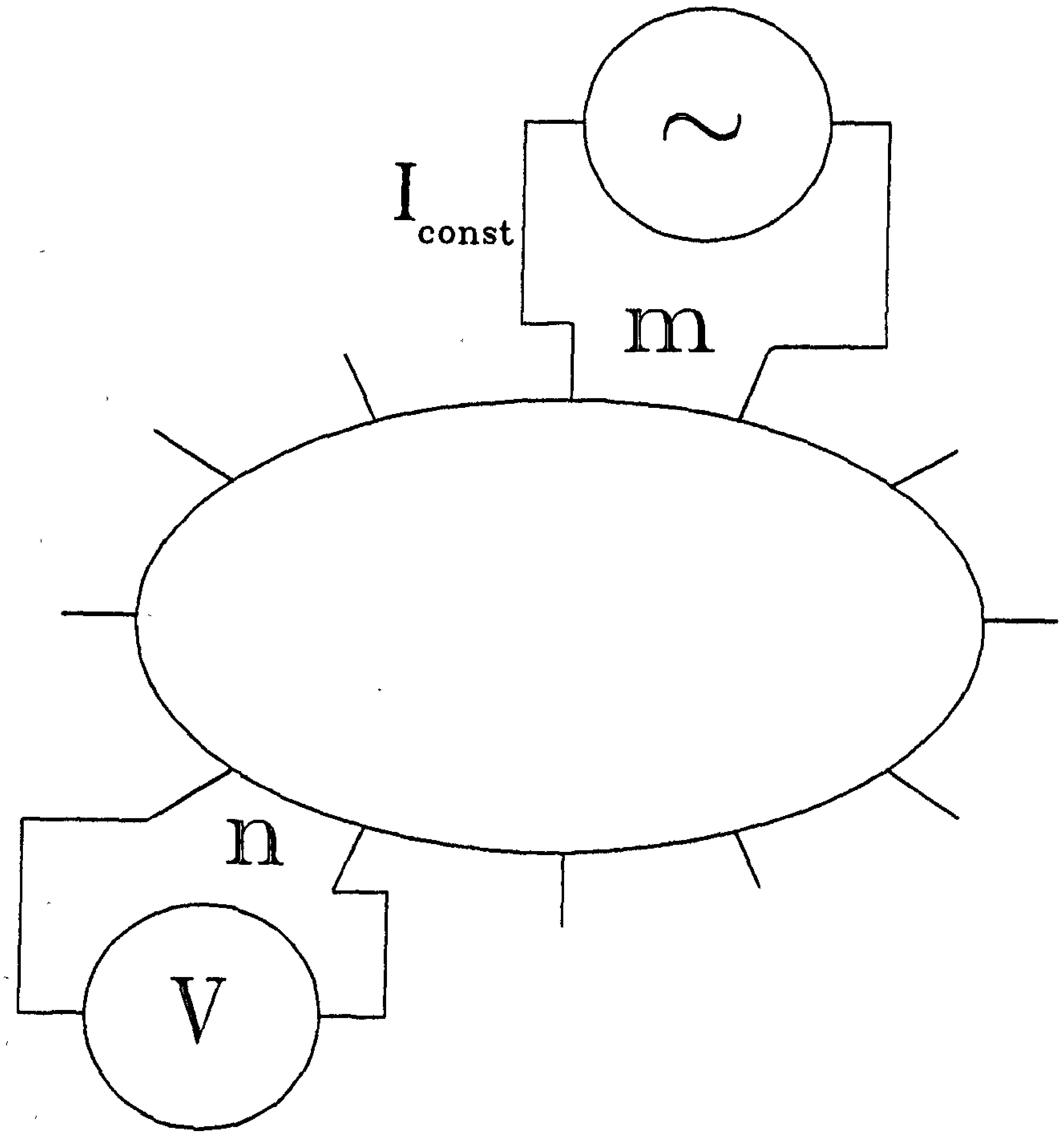

Figure 1.2

Four-electrode impedance measurement method

1.5 Electrode placement

The present generation of EIT systems are designed to use either a ring of 16 ECG electrodes around the plane to be imaged, or a flexible electrode belt on which the electrodes are etched. In either case, data at one plane only are available and the positions in space of the electrodes are not directly measured. (A method for calculating the positions of electrodes from the measured data set has, however, been proposed by Kiber et al (1990)).

The reconstruction algorithm investigated in this work will operate on data from the present generation of EIT systems (section 5.4) but is principally intended for 3-dimensional operation on multiple plane data sets with accurately known electrode positions. Provided that it is not intended to inject current between electrode planes, the data collection strategies discussed above will still apply. Such an approach also avoids the need to collect all planes of data simultaneously. To produce multiple plane data sets in clinical practice with accurate and rapid electrode placement would require an electrode carrier as envisaged by Smith (1985). An electrode carrier of this type has already been developed for EIT imaging of the breast (Jossinet, 1988) although this design does not include simultaneous measurement of electrode position or make specific provision for the collection of multiple plane data sets.

1.6 Data sets for electrical impedance tomography

Two major approaches to EIT can be defined; static imaging, in which the desired result is a distribution of absolute values of impedance, and dynamic imaging, in which a distribution of changes in impedance is to be imaged. Static imaging requires a data set of absolute measurement values and necessarily requires an iterative approach to image reconstruction. Dynamic imaging can, however, be carried out using as a data set the normalised change between two sets of impedance measurements, and approximate linear reconstruction methods can be employed provided the changes to be imaged are small. Other advantages to the dynamic approach are insensitivity to errors caused by electrode contact impedance and electrode placement inaccuracy (Barber and Brown, 1988). The linear reconstruction method explored in this work is intended for use in dynamic EIT.

Pairs of data sets for dynamic imaging can be produced in a number of ways. Where a temporal change in impedance, such as during respiration or within the cardiac cycle is to be imaged, data sets separated in time are required. One of the strengths of EIT is its temporal resolution, as the time taken to acquire a set of impedance measurements can be quite short. Data acquisition times as short as 39 ms have been reported (Sinton et al 1992) making possible runs of images at video frame rates.

Data sets for dynamic imaging can also be produced by exploiting the frequency dependent properties of tissue both in terms of its bulk impedance and its complex component. Dual frequency images of the forearm have been produced using frequencies of 40.96 and 81.92 kHz (Zhang and Griffiths, 1987) and simulations have demonstrated the feasibility of producing separate images of resistivity and relative permittivity if the complex components of the data sets at two frequencies are available (Griffiths and Ahmed, 1987).

A further option for dynamic imaging is to use as a reference data set a set of real or computed measurements from an object with the same boundary shape as the object being imaged, but with homogeneous resistivity. The dynamic imaging approach can then be used to produce a quasi-static image of changes from a uniform reference. With appropriate calibration, it would be expected that this approach could produce a similar result to true static imaging, although the changes being imaged are unlikely to be small enough to justify the use of linear reconstruction techniques except as an approximation.

1.7 Data acquisition systems for electrical impedance tomography

A detailed review of the design and construction of data acquisition systems for EIT will not be attempted as this is a major subject in its own right, and not directly relevant to the investigation of the reconstruction method presented in this work. Reviews of the general design requirements for EIT systems have been given by Brown and Seagar (1987), and Murphy and Rolfe (1988).

1.8 A review of clinical applications

Although the technique of electrical impedance tomography is still under development, a number of preliminary trials of prospective clinical applications have been carried out using prototype EIT systems. Further possible applications of EIT based on known electrical properties of tissue have been suggested. All of the applications listed employ the dynamic imaging approach and all are based on an assumption of 2-dimensional geometry.

In EIT of the chest, two main time varying impedance changes can be detected, related to respiration and to the cardiac cycle. Dynamic imaging of the lungs has shown clear demarcation between the left and right lungs and a linear relationship between the reconstructed pixel value in the lung and the volume of air inspired (Harris et al, 1987). Emphysema of the lung has also been shown to be detectable. It is suggested that EIT should be sensitive to the volume of fluid in the lungs and therefore be of use in following the course of treatment in established cases of pulmonary oedema, and in monitoring any change in oedema following cardiac failure (Brown et al, 1985).

Because the impedance changes related to the cardiac cycle are of low amplitude, it is necessary to carry out signal averaging synchronised to the electrocardiogram (Eyüboglu and Brown, 1988; Silva et al 1990). The signals related to the cardiac cycle can also be separated from the respiratory signals by (temporal) frequency filtering, which reduces the amount of signal averaging necessary (Zadehkoochak et al, 1992). This technique has also been used successfully at high frame rates (Smith et al, 1990). A comparison between EIT and radioisotope lung perfusion scans showed detectable clinical abnormalities in the EIT images, but only with the foreknowledge provided by the radioisotope images (McArdle et al, 1988).

Using an array of electrodes encircling the abdomen, the high impedance contrast between water and physiological tissue has been exploited to perform studies of gastric clearance. A reference set of data before ingestion of the test drink or meal, and a sequence of data sets following ingestion are used to generate a sequence of dynamic images. By plotting the change in mean pixel value over the stomach with time, a gastric emptying profile can be produced. Good correlation between the EIT method and the equivalent examination carried out using a radioisotope technique has been demonstrated (Mangnall et al 1987, 1988), although the acidity of the stomach contents are known to affect the results (Evans and Wright, 1990). Measurement of gastric emptying using EIT has been applied to the diagnosis of infantile hypertrophic pyloric stenosis (Lamont et al, 1988). Changes in impedance due to acid and stomach volume changes have also been imaged and associated with changes in activity of the migrating motor complex

(Wright and Evans, 1990). Further up the digestive tract, measurements of pharyngeal transit time have been made using an array of electrodes around the neck to image fluid being swallowed (Liu et al, 1992).

The use of EIT in the head is complicated by the presence of the skull which tends to distort the images and reduce the signal amplitude (Brown, 1990). By using ECG gated EIT data acquisition over a large number of cardiac cycles, however, images appearing to show bilateral changes in impedance associated with brain perfusion have been produced (Barber, 1990). Consideration of the amplitude of impedance changes expected to arise during neuronal discharge in the brain suggests that the changes are probably too small to be detected with the present generation of EIT systems, although the changes associated with the pathological condition of spreading depression are larger and possibly suitable for EIT imaging (Holder and Gardner-Medwin, 1988). The monitoring of neonates to detect intraventricular haemorrhage using EIT has been investigated, and dynamic images have been produced of the displacement of cerebro-spinal fluid in the ventricle by blood (Murphy et al 1987).

Dynamic EIT has been used to image fluid shifts in women with pelvic venous congestion following a change from the supine to the erect position. The results appear to show a different distribution between confirmed cases and a control group (Thomas et al, 1991). Fluid shifts during short periods of weightlessness have been imaged using a portable EIT system. It is thought that this technique could have applications in monitoring longer term fluid shifts in orbiting astronauts (Lindley et al, 1992).

The impedance contrast between blood and physiological saline has been used to measure blood flow in vitro and in vivo in the peripheral vascular system using a dilution technique. The saline is injected as a tracer and the area under the impedance change with time curve related to blood flow (Brown et al, 1992).

It has been suggested that the relationship between impedance change in tissue and temperature could be exploited to provide a method for non-invasive temperature mapping in hyperthermia treatment by EIT (Conway, 1987; Persson et al, 1990; Conway et al, 1992). This application has produced a number of in vitro and in vivo results, but has not been reported as being used in the clinical environment.

EIT has been used to monitor the process of bone healing following fractures of the upper arm. The geometry of this problem is conducive to EIT using a 2-

dimensional approximation as the cross-section of the arm does not change rapidly with axial distance from the electrode plane. The presence of a contralateral limb for comparison is also useful. Quasi-static images using a cylindrical saline tank to provide a reference data set have been produced (Kulkarni et al, 1990). The resulting images, although of poor quality, do appear to show changes associated with the process of bone healing and are reported to show the difference between normal bone, a united fracture and a non-union (Ritchie and Kulkarni, 1990).

EIT imaging of the breast is an attractive proposition because of the known changes in the dielectric properties of breast tissue with pathology, and because of the accessibility for electrode placement and simple geometry of the breast. Non-tomographic electrical imaging of the breast has been reported (Sollish et al, 1979; Man et al, 1979; Sollish et al, 1981) and systems for electrode placement and data acquisition directed at breast imaging have been described (Jossinet et al, 1981; Skidmore et al, 1987; Jossinet, 1988) but no in vivo EIT images have been presented.

Significant changes in the dielectric properties of physiological tissue following cell death are known to occur. A possible imaging application using this effect might be to follow the course of radiotherapy (Brown, 1990) but this has not yet been attempted. A cross-sectional image related to the delivered radiotherapy dose distribution would be very valuable as a means to confirm that a prescribed dose distribution had been achieved.

1.9 Summary of chapter 1

The background to electrical impedance tomography applied to medical imaging has been given in terms of the physical parameter to be imaged and its dependence on tissue type, physiology and in some cases pathology. The overall strategy for data collection using the four-electrode technique has been described, with particular emphasis on dynamic imaging, i.e imaging changes in impedance. The possibility of using multiple plane 3-dimensional data sets for the reconstruction of 3-dimensional impedance distributions has been discussed, and a range of possible clinical applications of EIT reviewed.

CHAPTER 2

THE RECONSTRUCTION OF ELECTRICAL IMPEDANCE TOMOGRAMS

2.0 Introduction

In this chapter some of the fundamental relationships which form the basis for electrical impedance tomography will be examined. This will lead to a specification of a reconstruction algorithm together with a list of assumptions required for its operation. A review of published reconstruction methods will be undertaken in order to clarify the requirement for, and specification of the proposed reconstruction algorithm.

2.1 Fundamental relationships relating to current flow in a volume conductor

The influence of the resistivity distribution within a volume conductor on the current flow within the conductor can be expressed by Poissons' Equation,

$$\nabla.(\sigma\nabla\Phi) - f \qquad (2.1)$$

where σ, Φ and f are the conductivity, potential and impressed current source distributions within the bounded volume conductor, and ∇ is the gradient operator. Where the volume conductor contains no current sources, this equation reduces to,

$$\nabla.(\sigma\nabla\Phi) - 0 \qquad (2.2)$$

For the special case of a homogeneous conductivity distribution, σ is a constant and the relationship further reduces to Laplace's Equation,

$$\nabla^2\Phi - 0 \qquad (2.3)$$

Where the conductivity distribution is non-uniform but isotropic, equation 2.2 reduces to

$$\nabla^2\Phi = -\left(\frac{1}{\sigma}\right)\nabla\sigma.\nabla\Phi \qquad (2.4)$$

which may be expressed in the simpler form

$$\nabla^2\Phi = \nabla R.\nabla\Phi \qquad (2.5)$$

by defining a logarithmic resistivity, $R = -\ln \sigma$ (Barber and Brown, 1984).

Certain simplifying assumptions are required to justify the use of the above relationships in the context of electrical impedance tomography applied to medical imaging. These initial assumptions are:

Assumption 1) Quasi-static conditions hold. As described in section 1.2, alternating currents are used in EIT, but the quasi-static assumption can be justified provided that the wavelength of the potential distribution within the bounded volume is large compared with the maximum dimension of the volume so that the current everywhere in the volume varies in synchrony. This is the case for EIT where the drive current frequency is normally in the range 20 - 50 kHz.

Assumption 2) Current flow in the conductivity distribution, σ, is due to pure conduction and has no displacement component. In general, displacement currents in tissue are normally much smaller than conduction currents (e.g Witsoe and Kinnen, 1967). Larger proportions of displacement current have been reported for skeletal muscle in the transverse direction (Zheng et al, 1984) although current flow in the longitudinal direction (along the muscle fibres) was found to be predominantly resistive.

Assumption 3) There are no current sources within the bounded volume. This statement can be said to be true in practice since, although the human body contains various electrical sources, these do not operate in the frequency range used by EIT and would be filtered out by a practical EIT measurement system.

Assumption 4) The conductivity distribution, σ, is isotropic. The conductivity of skeletal muscle is, in fact, known to be highly anisotropic (Rush et al, 1963) due to its fibrous structure, but due to the added complications involved in allowing for anisotropy, the assumption of isotropy is made by most workers (e.g Seagar et al, 1987b; Barber, 1989a).

Equation 2.5 represents a non-linear relationship between Φ and R because of the occurrence of $\nabla\Phi$ on the RHS of the equation. This implies that the solution to the inverse problem of calculating the distribution of log resistivity, R, from the voltage distribution measurable at the boundary will, in general be an iterative process (Murai and Kagawa, 1985). It is possible, however, to formulate the problem in a linear fashion provided a further assumption is made:

Assumption 5) The imaged parameter is related to the spatial distribution of small changes in conductivity. As discussed in section 1.6, these changes may be temporal or related to the frequency of the applied current and this approach would be expected to deliver only conductivity changes rather than absolute values of conductivity i.e dynamic rather than static images. The assumption of small changes is equivalent to the assumption that the current flow pattern in the conductivity distribution is not significantly disturbed after the distribution of changes is applied.

Following the approach of Barber and Seagar (1987) and considering the case of a reference distribution of R, R_r, and a perturbed distribution, $R_r + R_p$, if Φ_r is the solution to the equation

$$\nabla^2\Phi_r = \nabla R_r.\nabla\Phi_r \tag{2.6}$$

and $\Phi = \Phi_r + \Phi_p$ is the solution to the equation

$$\nabla^2\Phi = (\nabla R_r+\nabla R_p).\nabla\Phi \tag{2.7}$$

then

$$\nabla^2\Phi_p + \nabla^2\Phi_r = \nabla R_r.\nabla\Phi_p + \nabla R_r.\nabla\Phi_r + \nabla R_p.\nabla\Phi_p + \nabla R_p.\nabla\Phi_r \tag{2.8}$$

If the perturbation, R_p, is small, then the terms in $\nabla\Phi_p$ can be eliminated as being small compared with the terms in $\nabla\Phi_r$ to give

$$\nabla^2\Phi_p + \nabla^2\Phi_r = (\nabla R_p + \nabla R_r).\nabla\Phi_r \tag{2.9}$$

Substituting for $\nabla R_r.\nabla\Phi_r$ from equation 2.6,

$$\nabla^2\Phi_p = \nabla R_p.\nabla\Phi_r \tag{2.10}$$

This equation shows that there is a linear relationship between small perturbations of log resistivity, R_p, and the resulting perturbations of the potential distribution within the volume conductor, Φ_p, including the potential distribution along the boundary. For sets of measurements of the boundary potential for the log resistance distribution, R_r, and for the perturbed distribution, $R_r + R_p$, there will therefore be a set of linear equations relating the changes in log resistivity, R_p, to changes in boundary potential. The reconstruction of images of change in log resistivity, R_p, requires the inversion of this set of equations.

2.2 Sensitivity coefficients

A set of linear equations defining the 'forward problem' of calculating voltage changes at the boundary of an object from knowledge of its internal conductivity distribution can be established using the sensitivity theorem developed from electrocardiography lead theory by Geselowitz (1971) and independently proved by Lehr (1972).

For the situation illustrated in figure 2.1a, which shows a volume conductor of uniform conductivity, σ, carrying a constant current I_m impressed via the electrode pair, m, which gives rise to a voltage $V_{m,n}$ measured at electrode pair, n. Conversely (figure 2.1b), a current I_n, impressed via electrode pair, n, results in a voltage $V_{n,m}$ across the pair, m. The mutual impedance, $Z_{m,n}$, between the electrode pairs m and n is, by definition,

$$Z_{m,n} = \frac{V_{m,n}}{I_m} = \frac{V_{n,m}}{I_n} \tag{2.11}$$

the second equality being a consequence of the reciprocity theorem. The sensitivity theorem states that when the conductivity distribution changes from σ to $(\sigma+\delta\sigma)$, the mutual impedance change, $\delta Z_{m,n}$, for the pairs of current drive and voltage sense electrodes m and n can be given as

$$\delta Z_{m,n} = -\int_U \delta\sigma \frac{\nabla\Phi_m(\sigma)}{I_m} . \frac{\nabla\Phi_n(\sigma+\delta\sigma)}{I_n} .dU \tag{2.12}$$

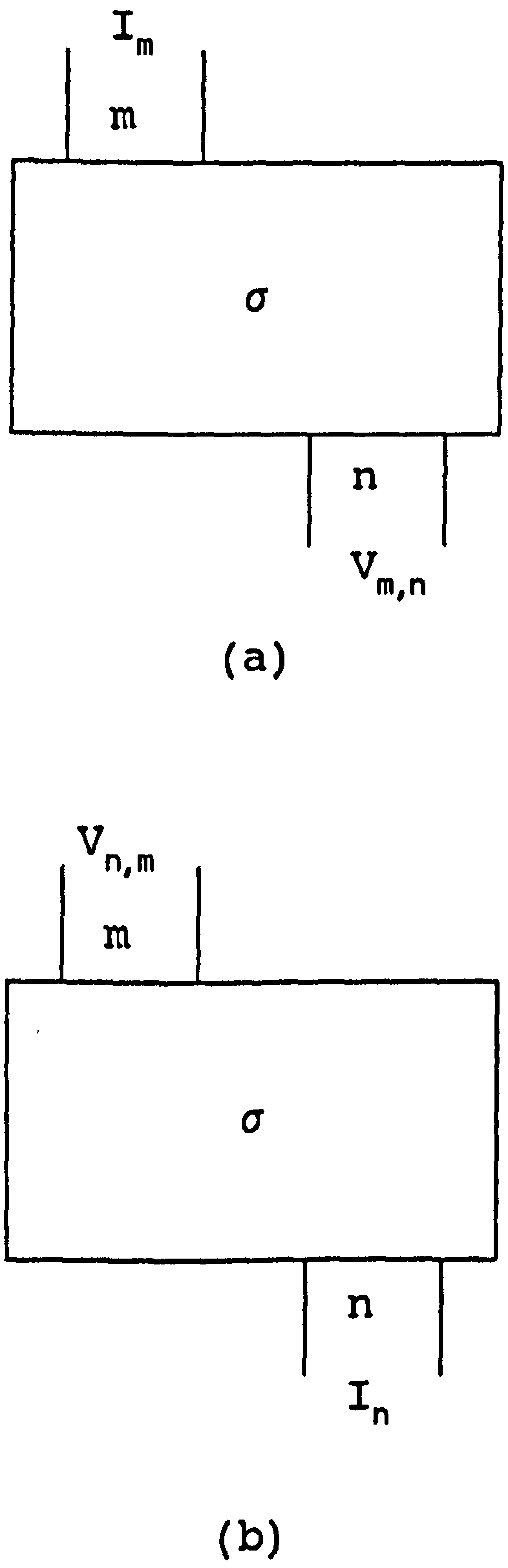

Figure 2.1

A volume conductor of uniform conductivity, σ, (a) carrying a current, I_m impressed by electrode pair, m, and (b) I_n impressed by electrode pair, n. Refer to equation 2.11.

In this equation $\Phi_m(\sigma)$ is the potential distribution over the bounded volume when the current I_m is applied via the electrode pair, m, and σ indicates the conductivity distribution when $\Phi_m(\sigma)$ is established for I_m. $\Phi_n(\sigma+\delta\sigma)$ is the potential distribution when the current I_n is applied via the electrode pair, n, and $(\sigma+\delta\sigma)$ indicates the conductivity distribution when $\Phi_n(\sigma+\delta\sigma)$ is established for I_n. The integration is carried out over the whole of the bounded volume, U.

Using a truncated Taylor expansion, the term $\nabla\Phi_n(\sigma+\delta\sigma)$ can be expanded with respect to $\delta\sigma$ (Murai and Kagawa, 1985) to give

$$\nabla\Phi_n(\sigma+\delta\sigma) = \nabla\Phi_n(\sigma) + \nabla(\delta\sigma\Phi'_n(\sigma)) + \ldots\ldots\ldots \qquad (2.13)$$

Equation 2.12 can then be expressed as

$$\delta Z_{m,n} = -\int_U \delta\sigma \frac{\nabla\Phi_m(\sigma)}{I_m}.\frac{\nabla\Phi_n(\sigma)}{I_n}\,dU + 0((\delta\sigma)^2) \qquad (2.14)$$

where $0((\delta\sigma)^2)$ indicates the higher order terms in $\delta\sigma$. If $\delta\sigma$ is small enough (assumption 5), these higher order terms can be neglected (Nakayama et al, 1981; Murai and Kagawa, 1985). Breckon and Pidcock (1987) show that a similar relation holds for the mutual impedance, $Z_{m,n}$, for the case of the unperturbed conductivity distribution, σ,

$$Z_{m,n} = \int_U \sigma \frac{\nabla\Phi_m(\sigma)}{I_m}.\frac{\nabla\Phi_n(\sigma)}{I_n}.dU \qquad (2.15)$$

If the conductivity and conductivity change distributions, σ and $\delta\sigma$, are divided into volume elements within which the conductivity remains constant, $\sigma(x,y,z)$ and $\delta\sigma(x,y,z)$, then equations 2.14 and 2.15 can be rewritten in terms of a summation over all the volume elements making up the bounded volume

$$\delta Z_{m,n} = -\sum_x\sum_y\sum_z \delta\sigma(x,y,z).\int_u \frac{\nabla\Phi_m(\sigma)}{I_m}.\frac{\nabla\Phi_n(\sigma)}{I_n}.du \qquad (2.16)$$

$$Z_{m,n} = \sum_x \sum_y \sum_z \sigma(x,y,z) \int_u \frac{\nabla\Phi_m(\sigma)}{I_m} . \frac{\nabla\Phi_n(\sigma)}{I_n} .du \tag{2.17}$$

The integration is now over the volume of the element, u. It is convenient to define a sensitivity coefficient, $S_{m,n,x,y,z}$, such that

$$S_{m,n,x,y,z} = \int_u \frac{\nabla\Phi_m(\sigma)}{I_m} . \frac{\nabla\Phi_n(\sigma)}{I_n} .du \tag{2.18}$$

In the case of the four-electrode technique applied to EIT (section 1.2), a constant current is applied for all current drive orientations, so $I_m = I_n = I$. It is still useful, however, to include this current term in the definition of the sensitivity coefficient to make it compatible with work in electro-cardiography (where the quantity $\nabla\Phi(\sigma)/I$ is called the 'lead field') and to make the sensitivity coefficients independent of the current which will vary between measurement systems. Interpreted physically, the sensitivity coefficient, $S_{m,n,x,y,z}$ relates the magnitude of voltage change measured at a voltage sense electrode pair, n, to a small perturbation in conductivity occurring at the point (x,y,z) when a constant current I is being injected by the current drive electrode pair, m.

Dividing equations 2.16 and 2.17, and substituting from 2.18, an expression for the fractional change in mutual impedance can be given as

$$\left(\frac{\delta Z}{Z}\right)_{m,n} = - \frac{\sum_x \sum_y \sum_z S_{m,n,x,y,z} \delta\sigma(x,y,z)}{\sum_x \sum_y \sum_z S_{m,n,x,y,z} \sigma(x,y,z)} \tag{2.19}$$

This can be further simplified provided that a further assumption is made:

Assumption 6) The initial, unperturbed conductivity distribution is one of constant conductivity. The conductivity distribution σ(x,y,z) can then be replaced with a constant, σ. This assumption will be violated in most medical imaging applications, but there is evidence that this does not prevent the formation of images in practice (Barber and Brown, 1986; Barber, 1990).

Noting that, for a constant current, from 2.11,

$$\left(\frac{\delta Z}{Z}\right)_{m,n} = \left(\frac{\delta V}{V}\right)_{m,n} \tag{2.20}$$

and that, from the definitions of conductivity and resistivity,

$$\frac{\delta\sigma}{\sigma} = -\frac{\delta\rho}{\rho} \tag{2.21}$$

and, provided that $\delta\rho << \rho$ (assumption 5),

$$\frac{\delta\rho}{\rho} = \ln\left(1+\frac{\delta\rho}{\rho}\right) = \ln(\rho+\delta\rho)-\ln(\rho) = \delta R \tag{2.22}$$

where R is log resistivity as defined in section 2.1, equation 2.19 can be re-written as

$$\left(\frac{\delta V}{V}\right)_{m,n} = \frac{\sum_{x}\sum_{y}\sum_{z} S_{m,n,x,y,z}\,\delta R(x,y,z)}{\sum_{x}\sum_{y}\sum_{z} S_{m,n,x,y,z}} \tag{2.23}$$

This expression represents in an explicit form a set of equations relating small perturbations of log resistivity to changes (in this case normalised) in the boundary potential, the general form of which was given as equation 2.10.

2.3 A short review of EIT image reconstruction methods

Following the publication of results showing low resolution projection images of the human chest produced using a 10 x 10 array of current sensing electrodes (Henderson and Webster, 1978) the potential advantages of producing cross-sectional images of electrical impedance were discussed by Price (1978a, b). Price predicted that the use of a two-electrode impedance measurement technique with extra guard electrodes would produce a "beam of current" which could be swept across the section to be imaged, to give measurements which could then be reconstructed using techniques based closely upon those of X-ray CT. It soon emerged, however, that the question of image reconstruction would not be so straightforward when Bates et al (1980) produced an analysis showing that it is, in general, impossible to uniquely reconstruct conductivity distributions using methods designed to produce straight and parallel current streamlines.

A more feasible approach was used by Kim et al (1983) and Murai and Kagawa (1985), who defined the forward problem of relating a conductivity distribution to resulting transfer impedance by using the sensitivity theorem of

Geselowitz (1971), previously used in electrocardiography. Using this approach, the boundary potential distribution can be related to the conductivity distribution by a forward transformation matrix calculated using the sensitivity theorem. In general, the inverse problem of static EIT image reconstruction can then be approached by inverting the forward transformation matrix. The matrix inversion problem is, however, non-linear and ill-conditioned (i.e small changes in boundary potential can be associated with very large changes in the conductivity distribution) making the inversion quite difficult. The non-linearity of the problem requires that an iterative solution is used, and its ill-conditioned nature requires additional constraints to be applied to ensure convergence in the presence of noise.

The strategy for achieving this kind of iterative solution is to assume an initial conductivity distribution, then using a numerical solution to Poisson's equation to calculate the current or voltage distribution at the surface of the object expected to result from the application of the known current or voltage distribution produced by the measurement apparatus. The predicted surface distribution is then compared with the actual measurements, and the differences used to adjust the conductivity values in the model so that they move towards the true values. The process is repeated until the predicted values of current or voltage are sufficiently close to their measured values. Iterative approaches mainly differ in the way the conductivity values are adjusted at each iteration. A comparison of several iterative approaches and suggested improvements have been made by Yorkey et al (1986) and Yorkey and Webster (1987).

Although not restrained to two dimensions by definition, most work on schemes for iterative inversion of the forward transformation matrix have been carried out assuming a simplification to two dimensions. The three-dimensional problem has been specifically addressed by Wexler (1988) and Liu et al (1988).

Iterative, non-linear EIT reconstruction methods, although justified by the nature of the problem, suffer from some disadvantages in practice. Iterative methods require the forward problem of estimating the boundary voltages expected for a given conductivity distribution to be accurate to 1% or 2% (Barber, 1989a) if the method is to converge. This is difficult to achieve unless the knowledge of the surface shape of the object and the electrode positions are known very accurately. The amount of data storage and overall calculation time required for iterative reconstruction schemes can also be quite large (Woo, 1990). Where generalised, three-dimensional boundary shapes such as the human body are being considered it is not clear how the conductivity distribution used to produce the forward problem transformation matrix will be chosen to maximise the spatial information available in the measured data, as it is known that the spatial resolution in the final image will vary with position and boundary shape. Although some results from physical phantoms have been produced using iterative reconstruction methods (Kim and Woo, 1987; Sakamoto et al, 1987; Wexler, 1988) and crude in vivo static images from a one-step version of an iterative approach (Isaacson et al, 1992), no clinically useful images have so far been presented.

An alternative type of iterative EIT image reconstruction approach known as the adaptive current method has been suggested by Gisser et al (1987, 1988) and McLeod et al (1990). Using this approach, the measurement instrumentation is itself part of the iterative process as it adjusts the configuration of the current pattern it applies until it satisfies the requirement that it is the "best" current distribution to recover information about the conductivity distribution being imaged.

To simplify the EIT reconstruction problem, Nakayama et al (1981) and Sakamoto and Kanai (1983) considered the problem of imaging small changes in a conductivity distribution (dynamic images). For such small changes, the current distribution within the object can be considered to be unchanged by by the conductivity change, and the Geselowitz sensitivity theorem can be used to formulate a linear relationship between the conductivity change and the change in potential distribution at the boundary of the object. Using this approximation, non-iterative methods can be used to perform the image reconstruction task.

A number of workers have addressed the linearised EIT image reconstruction problem via analogy with the method of filtered backprojection used successfully in X-ray CT (e.g Barrett and Swindell, 1981). Unlike X-ray CT, where the ray paths of the X-ray beam are unchanged by the object shape and distribution of linear attenuation coefficients (see figure 2.4), the current distributions used to make measurements in EIT are strongly dependent on the object shape and the unknown conductivity distribution. By making appropriate assumptions, however, approximate solutions can be obtained using this approach which will be followed in the reconstruction method described in this work.

The most successful EIT reconstruction method to date has been that of Barber et al (1983) which employs the backprojection of normalised changes in boundary potential gradient along the equipotential lines of the voltage distributions produced by a range of orientations of applied currents (figure 2.2). The geometry

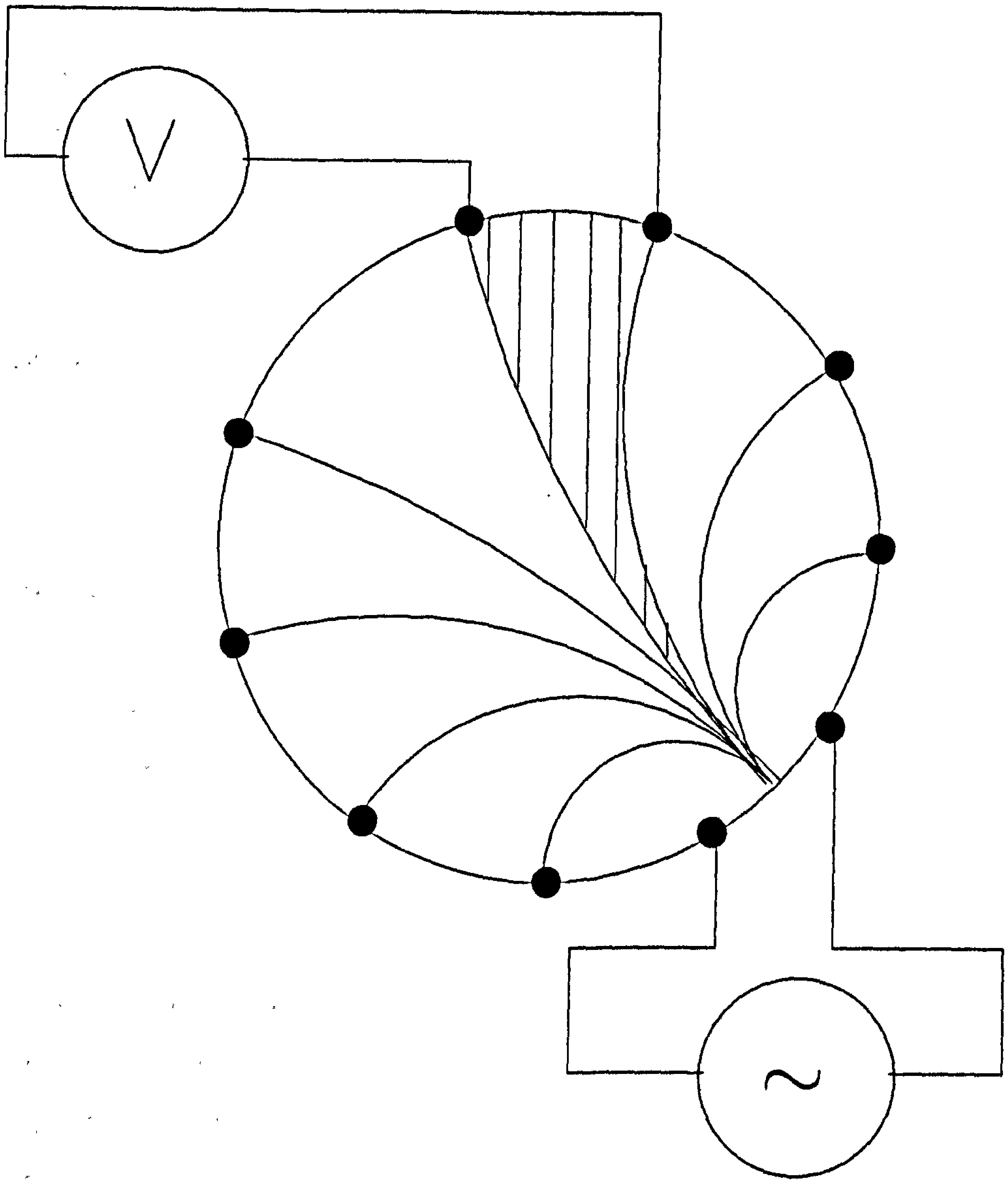

Figure 2.2

Backprojection between equipotential lines for 2-D circular region.

is fixed as a two-dimensional circular region with equally spaced electrodes. Adjacent electrode current drive is used which is approximated to a dipole in the reconstruction, so that the equipotentials can be taken as arcs of circles (Barber and Brown, 1986). Geometrically calculated weighting factors are used in the backprojection, and spatial frequency filtering in a geometrically transformed space is used to improve the appearance of the images (Barber and Seagar, 1987). A recent development of this method has used backprojection weights calculated from a consideration of the approximate matrix inversion properties of this type of backprojection (Barber and Brown, 1990). The equipotential backprojection method has been shown to be very robust, and capable of producing phantom and in vivo dynamic images from both two and three dimensional objects with non-circular (or non-cylindrical) boundary shapes. The method does, however, suffer from some restrictive assumptions. Due to the fixed circular geometry, reconstructed images are often severely distorted and it is difficult to see how the method could be extended to incorporate three-dimensional data sets, true electrode positions and alternative drive current strategies.

Tarassenko and Rolfe (1984) used sensitivity coefficients calculated for a two-dimensional circular region by perturbing each element of the region in turn and calculating the resulting boundary potentials using a finite elements method. Images were reconstructed by backprojecting the ratios of the voltage gradients measured before and after a change in the conductivity distribution (dynamic image) weighted by the calculated sensitivity coefficients. The speed of the method was improved by using only the most significant sensitivity coefficients for each measurement/element combination. Images of a physical phantom and in vivo images have been presented (Tarassenko et al, 1985; Gadd et al, 1992).

The reconstruction algorithm proposed by Zadehkoochak et al (1990) is a single step method derived from the iterative method of Yorkey et al (1986), and related to backprojection in X-ray CT. Posed as an approximate matrix inversion method, the inverse matrix is formed using as an approximation a weighted transpose of the sensitivity coefficient matrix. Phantom and in vivo images have been sucessfully reconstructed using this method.

The reconstruction algorithm to be described in this work also uses a sensitivity coefficient weighted backprojection approach with the inverse matrix approximated by a weighted transpose of the sensitivity coefficient matrix. Early phantom and in vivo results using a two-dimensional model in conjunction with an empirical spatial frequency filter were reported in Kotre (1989a,b).

Figure 2.3 shows a diagrammatic interpretation of the relationships between the various EIT image reconstruction methods that have been reported, together with a representation of the computational effort required by the various methods and their imaging specification. The time scale is approximate by publication date. The algorithm developed in this work is intended to fill the gap in specification between the fast, two-dimensional circular bounded, dynamic imaging approach offered by the successful method of Barber and Brown (1986), and the more sophisticated, but as yet unproven, two- and three-dimensional iterative methods. The proposed algorithm introduces a three-dimensional approach which is capable of dealing with body contour boundary shapes, but which does not require the heavy computational effort of three-dimensional iterative methods.

2.4 A specification for an electrical impedance tomography reconstruction algorithm

As can be seen from the range of EIT reconstruction methods reviewed above, the implementation of a reconstruction algorithm requires a compromise between the specification of the algorithm (and hence the number of assumptions permissable) and the computational effort required to execute it. The reconstruction algorithm developed in this work is based upon a set of requirements which are intended to advance the utility of EIT as a clinical imaging modality, whilst remaining practicable in terms of computational effort. These requirements are as follows:

1) **The algorithm should produce dynamic images.** The analysis of section 2.1 would suggest that the appropriate parameter to be imaged is change in log resistivity.

2) **The algorithm should be non-iterative.** Provided that the application of the algorithm is restricted to the imaging of small changes in log restivity, an approximate linear reconstruction method should be appropriate.

3) **The algorithm should be defined in three dimensions.** The EIT reconstruction problem is intrinsically three-dimensional. Where data is derived from a single plane of electrodes, the algorithm should be capable of approximating the effects of out-of-plane current flow. When multiple plane data sets are available, the method should be capable of utilising this data to produce three-dimensional

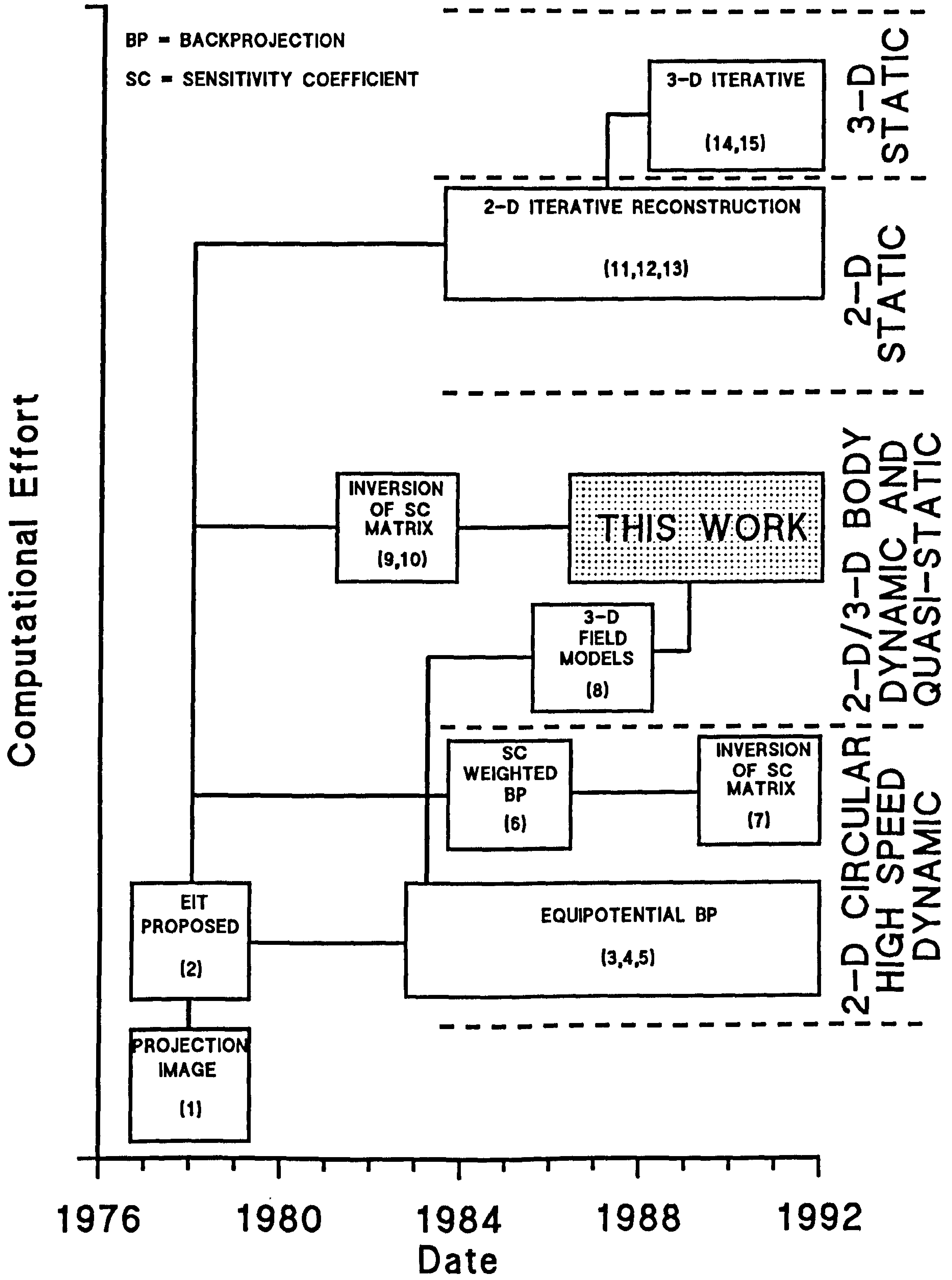

Figure 2.3

Relationships between various reported reconstruction methods.

(References over)

References to Figure 2.3

(1) Henderson and Webster, 1978.
(2) Price, 1978a, b.
(3) Barber et al, 1983.
(4) Barber and Brown, 1986.
(5) Barber and Brown, 1990.
(6) Tarassenko and Rolfe, 1984.
(7) Zadehkoochak et al, 1990.
(8) Kotre, 1988.
(9) Nakayama et al, 1981.
(10) Sakamoto and Kanai, 1983.
(11) Kim et al, 1983.
(12) Murai and Kagawa, 1985.
(13) Yorkey et al, 1986.
(14) Wexler, 1988.
(15) Liu et al, 1988.

reconstructions.

4) The algorithm should be capable of employing boundary conditions corresponding to measured body cross-sections. The positions in space of the electrodes could, in principle, be measured. This information could then be used to set the boundary conditions for the reconstruction algorithm provided it is sufficiently flexible in this respect. To meet this requirement, the algorithm should not make use of any parameters defined for an unrealistic fixed geometry (e.g radial distance from the centre of a circular image), but should relate to measured electrode positions and an assumed boundary simply connecting the known points.

5) The algorithm should be capable of employing a range of current drive configurations. Whilst a large proportion of previously published work has employed adjacent electrode current drive, this is not universally recognised as the optimal approach for all applications (Patel, 1990; Cheney and Isaacson, 1992). In addition, developments using induced rather than directly injected currents may lead to data sets containing more independent measurements (Gençer et al, 1992), so an algorithm capable of being adapted for this situation would be desirable.

6) The algorithm should be capable of operating on an image matrix containing a larger number of elements than there are independent measurements in the data set. It is known that the spatial resolution obtainable with EIT is variable with position in the image. If spatial frequency information present in the measured data set is not to be lost when using variable boundary conditions, it will be necessary to operate with a reconstruction matrix capable of representing the maximum spatial frequency expected in the image at all points.

2.5 A sensitivity coefficient weighted backprojection approach to EIT image reconstruction

It is possible to use the concept of sensitivity coefficients, which relate the spatial distribution of changes in the imaged parameter to changes in the measured data set, to draw an analogy between the technique of filtered backprojection used successfully in X-ray CT (e.g Barrett and Swindell, 1981) and the EIT reconstruction problem. Figure 2.4 shows the essential features of the two situations; figure 2.4a for one (parallel beam) ray measurement in CT where one element has a changed linear attenuation coefficient, and figure 2.4b for one impedance measurement in EIT where one element has a changed resistivity. The

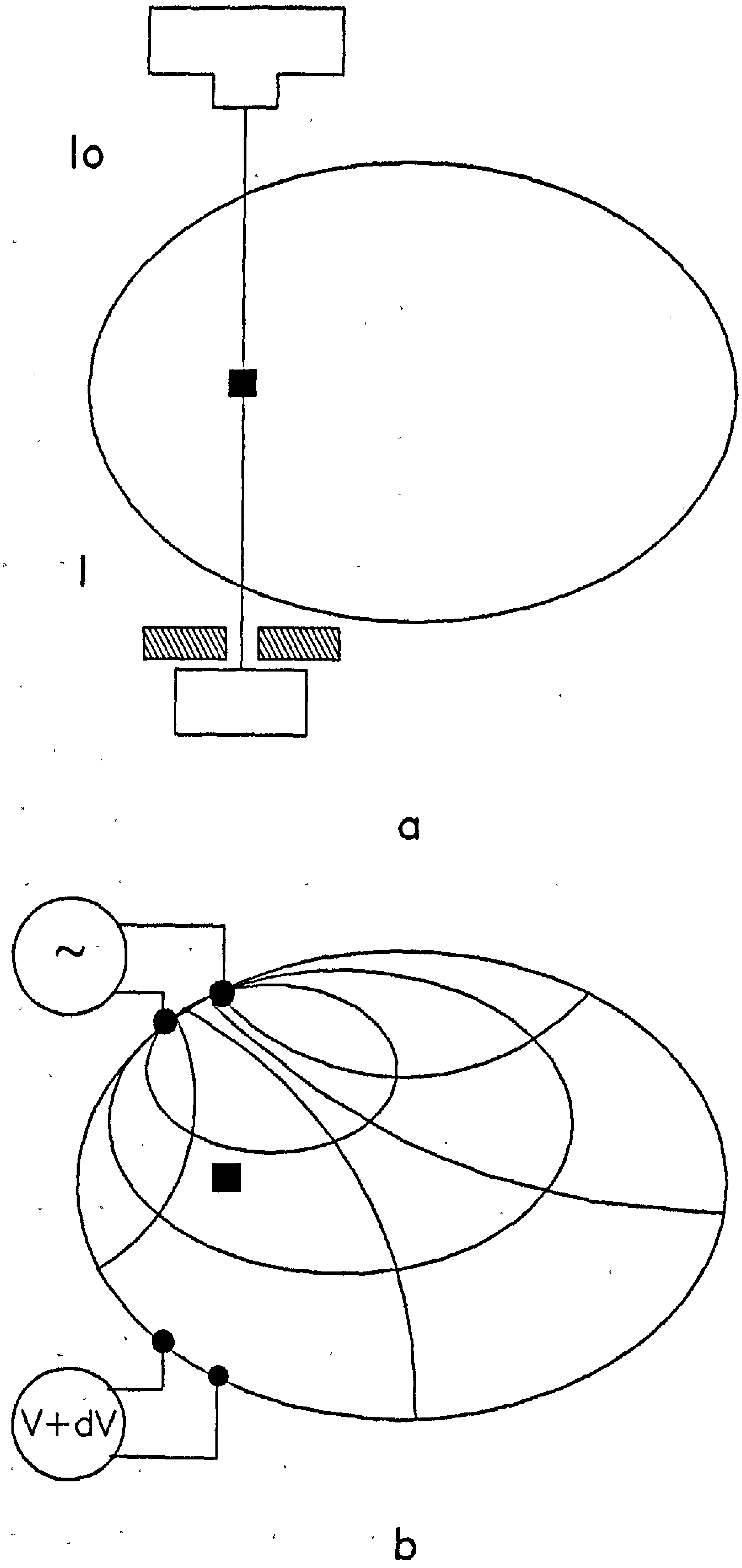

Figure 2.4
Comparison of measurement geometry for (a), computed tomography, where the highlighted pixel has a different linear attenuation coefficient to the background (incident x-ray intensity, Io; measured, I) and (b) EIT, where the pixel has a different resistivity (measured voltage, V+dV).

fundamental difference between the two cases is that, while the path of the pencil X-ray beam is known to be a straight line between source and detector, the current flow for the impedance measurement is distributed throughout the bounded volume. Both cases can be described in terms of sensitivity coefficients.

For the CT case, each measurement of $\ln(I_0/I)$ will be related to a set of sensitivity coefficients which have some constant value along the ray path (since a change in any of these pixels will affect the measured ray sum by the same amount) and a value of zero elsewhere. The operation of parallel beam backprojection can then be thought of as a multiplication of each measurement by all of the sensitivity coefficients to which it is related. The process is repeated for each measurement and the result summed into an image array. This operation is known to produce a blurred image which can be recovered by spatial frequency filtering because the blur is characterised by a Point Spread Function (PSF) which is constant with position and has a known form.

For the EIT case, each measurement of $(\delta V/V)$ will be related to a set of sensitivity coefficients which can be calculated from knowledge of (or assumptions about) the current density distribution within the object (equation 2.18), and which will have a range of values spatially distributed throughout the volume conductor. If a backprojection operation is defined similarly to the CT case, i.e each measurement of $(\delta V/V)$ multiplied by all the sensitivity coefficients to which it relates, then this operation will result in a weighted summation into a three-dimensional array. It is here proposed that this type of backprojection operation can also be used to produce blurred images in EIT which can then be further processed to reduce the effect of a now spatially variant PSF. This approach forms the basis for the reconstruction method to be developed in this work.

The problem of EIT image reconstruction can be simply stated using matrix notation. If the forward problem of calculating surface voltages from a known resistivity distribution and current excitation is defined as

$$FR = V \tag{2.24}$$

where R is a vector describing the resistivity distribution, V is a vector describing the surface voltage distribution, and F is the forward transformation matrix, then the inverse, image reconstruction, problem can be stated as

$$F^{-1} V - R \tag{2.25}$$

where F^{-1} is the inverse of the matrix F. If the problem is redefined in terms of small changes of log resistivity and normalised voltage gradient changes, $(\delta V/V)$, then the matrix F can be assembled from the appropriate sensitivity coefficients using equation 2.23 and the image reconstruction problem is then to find the inverse of this matrix. The backprojection operation defined above is equivalent, in its basic form, to using the transpose of the forward transformation matrix F^T, as an approximation to F^{-1}. There is no reason to assume that this approximation should work for the general matrix inversion case, and objections have been raised to its use in the specific case of EIT image reconstruction (Barber, 1989b), although images have have produced using related methods (Tarassenko and Rolfe, 1984; Zadehkoochak et al, 1990). The reconstruction method to be investigated in this work will concentrate on the use of the sensitivity coefficients in a weighted backprojection scheme rather than in any generalised matrix inversion sense.

2.6 Summary of chapter 2

In this chapter some of the fundamental relationships forming the basis of the EIT problem have been examined. By the application of a number of simplifying assumptions, a linear approximation governing the relationship between small perturbations in log resistivity and the resulting perturbations in the boundary potential distribution was arrived at. The sensitivity theorem was then used to produce a definition of the sensitivity coefficient and an explicit relationship between normalised boundary potential perturbations and perturbations of log resistivity. In order to clarify the position of the proposed reconstruction algorithm with respect to previously published work, a short review of EIT reconstruction methods was undertaken and a set of specifications for the proposed algorithm stated. An approach to EIT image reconstruction based on sensitivity coefficient weighted backprojection was described. Some parallels between this method and the successful method of filtered backprojection used in X-ray CT were indicated.

CHAPTER 3

THE DEVELOPMENT OF A THREE-DIMENSIONAL COMPUTER SIMULATION OF ELECTRICAL IMPEDANCE TOMOGRAPHY

3.0 Introduction

To investigate the properties of the proposed image reconstruction approach in isolation from the effects of the measurement process, a long series of computer simulations was carried out. The simulations were based on a physical system consisting of a cylindrical tank containing a conductive liquid into which objects of various sizes, shapes and resistivities can be introduced. A number of workers have made measurements on this type of system to investigate the effects of the introduction into the tank of insulating rods (Barber and Brown, 1986), conductive spheres (Jossinet and Kardous, 1987) and insulating planes (Rabbani and Kabir, 1991). In most cases measurements have been made between electrodes equally spaced in a plane at half the tank height. The simulation, however, makes provision for the case of multiple planes of electrodes spaced at equal distances along the axis of the cylinder in accordance with the specifications of 2.4, and treats the cylinder as extending to infinity above and below the plane of the image. So that the form of point spread functions could be examined, the resolution of the simulation was chosen to be considerably higher than the expected resolution of the images.

3.1 Simulation geometry

Figure 3.1 illustrates the geometry of the computer simulation used throughout chapters 3 and 4. A uniformly conducting cylinder is modelled as 63 layers of volume elements where each layer is of diameter 63 elements. This

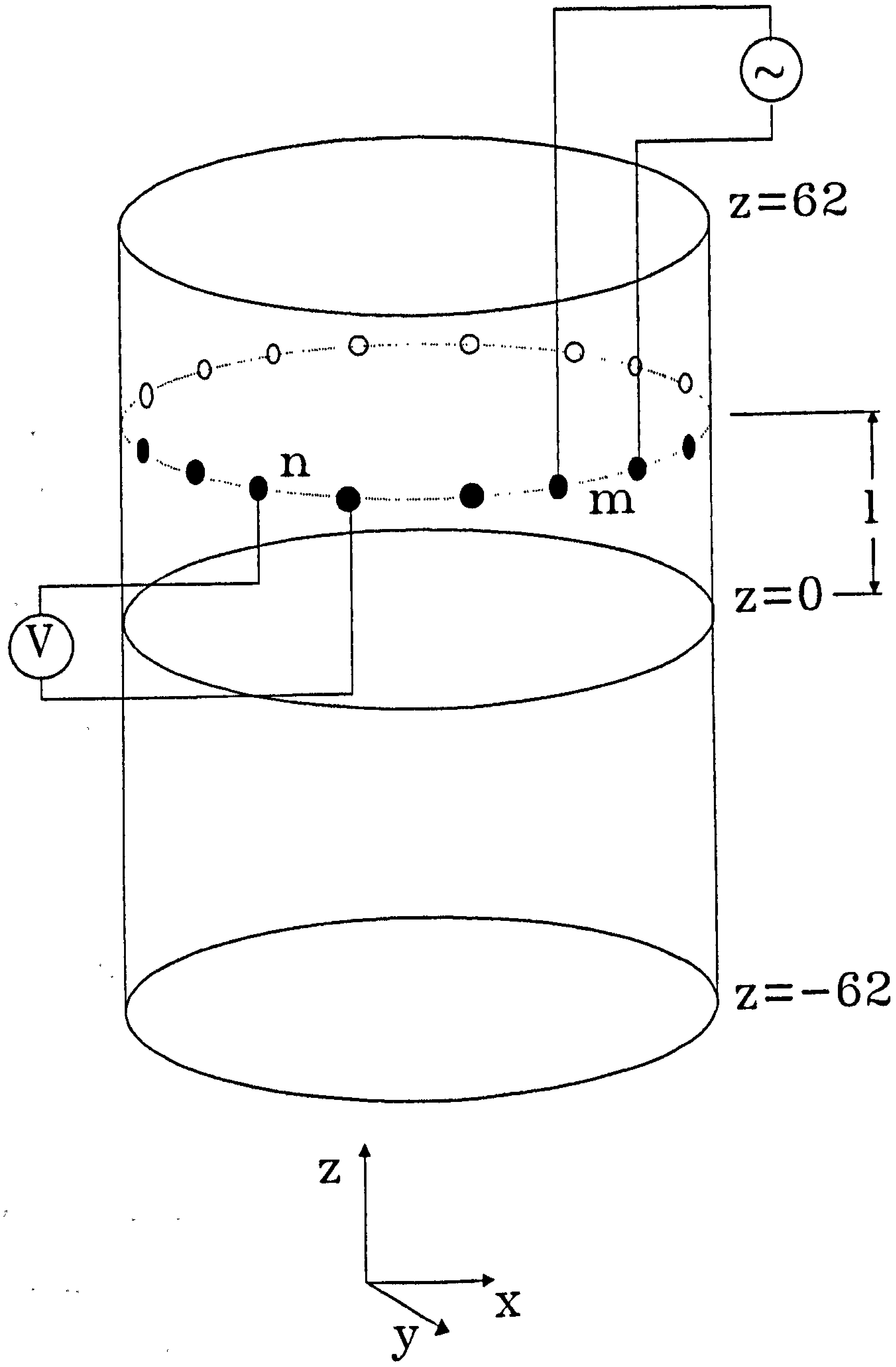

Figure 3.1

Geometry of
computer simulations

diameter was chosen so that the symmetrical case of an object exactly on the axis of the cylinder can be easily simulated. The position of each volume element is given by the cartesian coordinates (x,y,z). The origin of the coordinate system is on the axis of the cylinder in the plane of the image to be reconstructed. By symmetry about this plane, provided the test impedance change distribution is uniform in cross-section throughout the cylinder, the effect of including the layers -1 to -62 can be achieved by doubling the contributions made to the reconstruction from layers 1 to 63, so that the total simulation effectively refers to a cylinder twice as long as its diameter. It is assumed that the effect on the image of resistivity changes further than one image diameter away from the plane of the image is negligible, and conversely that measurements made in planes further away than one diameter from the image plane make no measurable contribution to the reconstructed image.

Sixteen equally spaced point electrodes are assumed to be in contact with the boundary for each of the planes $z = -62$ to $z = 62$. The electrode contact impedance is assumed to be zero so that all electrodes are considered to be available for voltage measurements. In accordance with the measurement approach described in section 1.3, a constant current is applied between adjacent electrode pairs, m, and voltage measurements are made between adjacent electrode pairs, n. The values of m and n are in the range 0 to 15. (In section 5.3 the effect of applying the constant current between other pairs of electrodes will be investigated in which case m applies across the larger electrode spacings.) The measurement process is repeated for each plane of electrodes, l.

3.2 Simulated test objects

For the majority of simulations that follow, the test object is a volume of raised or lowered resistivity one pixel in cross-section and extending through all the planes in the cylindrical test volume so that it appears at the same x,y position for all planes. The spatial resolution of the simulation is high with respect to the spatial resolution expected in the reconstructed images, so it is reasonable to regard this single pixel cross-section perturbation as an impulse from which the Point Spread Function (PSF) of the system in the plane of the image can be measured. Since this test resistivity distribution is of uniform cross-section, and can be considered to extend infinitely above and below the plane of the image, the set of voltage measurements for all electrode planes, l, will be identical. To calculate this set of voltages for the simulation, it is therefore only necessary to consider a section of the cylinder extending to one diameter above and below the plane of measurement assuming that the effect of resistivity changes beyond this will be negligible.

Because the set of voltage measurements for all planes, l, are identical, the effect of combining the influences of a large number of measurement planes into the reconstruction at the image plane z = 0 can be achieved by only considering the set of measurements at z = 0, but then forming the image as the sum of all the image planes in the simulation, effectively from l = -62 to l = 62. This can be thought of as leaving the electrode array stationary and then integrating the effect as the image plane moves down the axis of the cylinder passing through the plane of the electrodes. The overall result will be equivalent to reconstructing a single image plane from multiple electrode plane data sets. Because the sets of voltage gradients, V(l,m,n), and voltage gradient changes, δV(l,m,n) are in this case the same for all electrode layers, the index l is not really required. It will be retained, however, to be consistent with the 3-dimensional approach being considered.

For the investigation of the effect of out-of-plane perturbations on the reconstructed image (section 4.7), a single volume element of increased resistivity at various distances from the plane of the image is used.

3.3 Potential field calculation

In order to evaluate the sensitivity coefficients required for image reconstruction (section 2.2) it is necessary to know the potential at each volume element in the cylindrical volume under consideration when a constant current is applied between an electrode pair m at a distance l from the plane of the image. Since it is being assumed (section 2.5) that the initial unperturbed resistivity distribution is uniform, the potential field required is the solution to the Laplace equation (2.3) for the boundary conditions given by the geometry of the simulation. Since the Laplace equation cannot be solved analytically for other than simple boundary conditions, a numerical method is required. The choice lies between the Finite Difference Method (FDM) and the Finite Element Method (FEM) (e.g Ferrari, 1975). Finite difference methods utilise directly an approximation to the differential equation governing the system to relate potentials at nodal points on a fixed rectangular mesh which are then solved in an iterative process. In contrast, finite element methods derive nodal potentials by expressing the unknown voltages in terms of interpolation functions within each finite element. The basic grid mesh is usually formed from sets of interconnected triangles whose vertex coordinates may be varied to optimise the mesh for the appropriate geometry.

Although it is generally accepted that the FEM is superior to the FDM for arbitrarily shaped boundaries (Hua and Woo, 1990), the FEM is considerably more complicated to implement, and most users of the FEM use as a starting point an existing software package for mesh generation and field calculation. This is especially the case when 3-dimensional field calculation is required. Due to the difficulty of obtaining access to such a package and the attractive simplicity of the FDM it was decided to write a program specifically matched to the geometry of the simulation using the FDM.

The geometry of the boundary conditions used was similar to that shown in figure 3.1 with the plane of the current drive electrodes at $z = 0$. The symmetry of the field about $z = 0$ was again used to reduce the number of volume elements required, and the further symmetry of the field about the zero voltage equipotential plane was also employed. The geometry for the boundary conditions at $z = 0$ is shown in figure 3.2. In the figure, the semi-circular wall of the tank constitutes the Neumann portion of the boundary (where the condition of zero potential gradient normal to the boundary applies), and the shaded pixels along the zero voltage equipotential and the 'electrode' pixel constitute the Dirichlet (fixed voltage) portions. The point of electrode contact is thus modelled as being flush with the wall of the tank rather than intruding into it. To complete the definition of the boundary conditions, the planes $z = 0$ and $z = 62$ are defined as Neumann boundaries.

For guaranteed convergence the FDM program was run without employing overrelaxation to increase the convergence speed, and for improved accuracy in dealing with the sometimes very small potential differences between adjacent volume elements, double precision floating point (64 bit) arithmetic was specified. The stopping criterion ending the iteration process was chosen to be when the maximum potential difference detected between iterations anywhere in the data array was less than 1 part in 10^{11}. This was considered to give more than adequate accuracy for the field calculation, and resulted in a convenient overnight calculation time on the Sun Sparcstation 330 computer used in this work. The completed potential field array was then stored on disk.

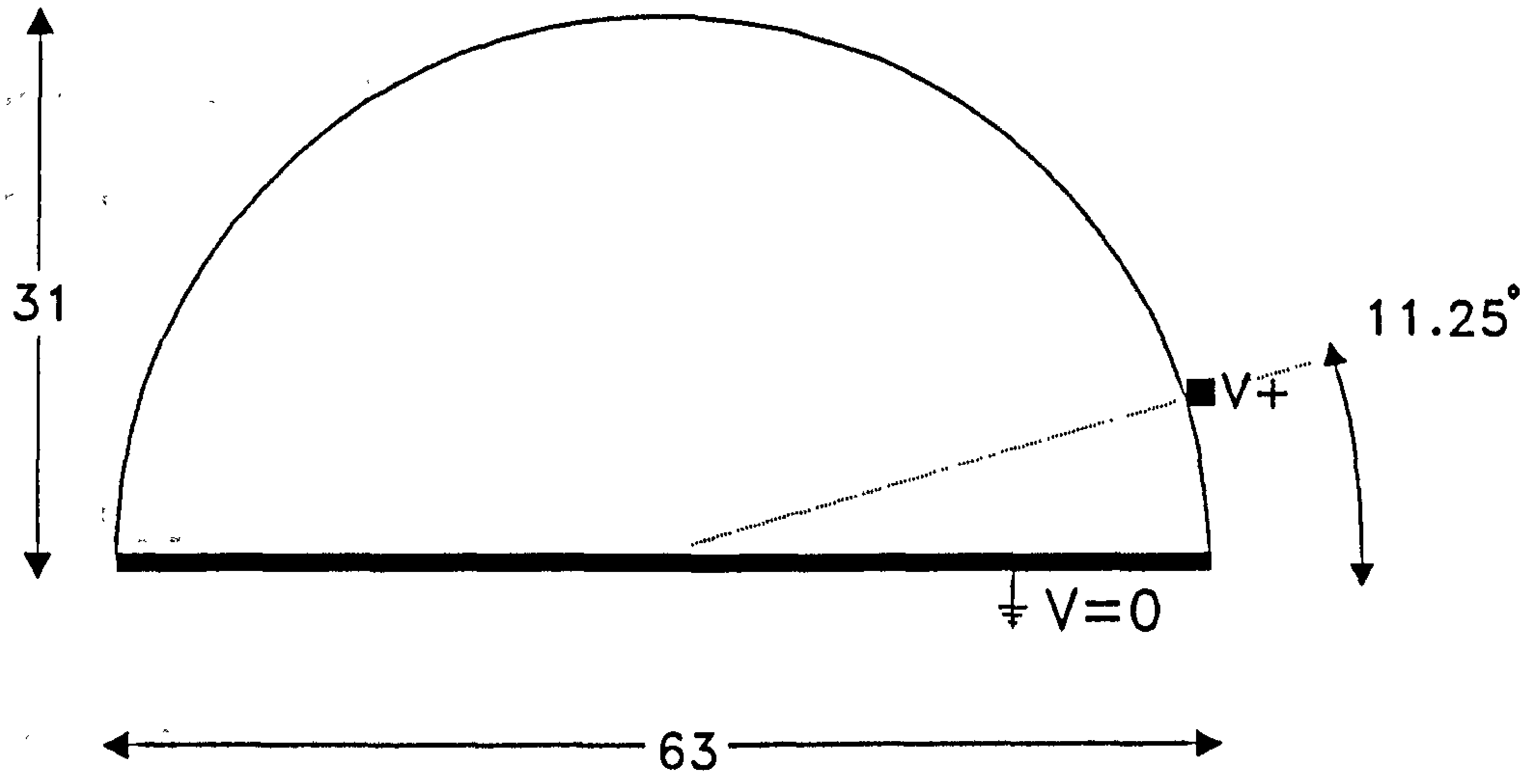

Figure 3.2

Geometry of boundary conditions for potential field calculation at z = 0.

The accuracy of the resulting potential distribution was checked by comparing the calculated boundary potentials with those previously measured on a real saline filled tank using a constant current 20 KHz signal source and a high input impedance true RMS averaging voltmeter (Kotre, 1988). The 3-dimensional distribution of the field was checked by displaying the equipotential patterns at various axial distances from the plane of the electrodes.

3.4 Sensitivity coefficient calculation

The sensitivity coefficient, $S_{l,m,n,x,y,z}$ at a point (x,y,z) for a current drive electrode pair, m, and a voltage sense electrode pair, n, in the electrode layer, l, is given by

$$S_{l,m,n,x,y,z} = \int_u \frac{\nabla\Phi_{l,m}}{I_{l,m}} . \frac{\nabla\Phi_{l,n}}{I_{l,n}} .du \qquad (3.1)$$

where the potential field $\Phi_{l,m}$ is due to the pair (l,m) and the potential field $\Phi_{l,n}$ is that which would have been produced if the pair (l,n) had been carrying the current (section 2.2). The integration is over the volume of the element which is constant. It is assumed that the value for the sensitivity coefficient in the simulation is constant throughout the volume element at (x,y,z). In EIT where constant currents are used, $I_{l,m} = I_{l,n} = I$, a constant which for the simulation will be taken as unity.

For the reasons given above (section 3.2), the plane of the electrodes can be taken as z = 0, and l = z. Thus the potential field calculated using the FDM can be used for all the sensitivity coefficient calculations required by rotating the coordinate system of the simulation by the appropriate number of inter-electrode angles, m and n, so that it coincides with the stored field. The polarity of the potential fields $\Phi_{l,m}$, and $\Phi_{l,n}$ also needs to be considered. If the polarity of $\Phi_{l,m}$, the current drive field is considered to be fixed, then the polarity of $\Phi_{l,n}$ will be the same where m = n but of opposite polarity in all other cases so that the most positive of the voltage sense pair is always closest to the positive current drive electrode.

The algorithm for the calculation of a sensitivity coefficient is shown in figure 3.3. The coordinate system rotations are made on a nearest-neighbour basis. Where the rotation results in a position x',y',z' or x",y",z" outside the defined

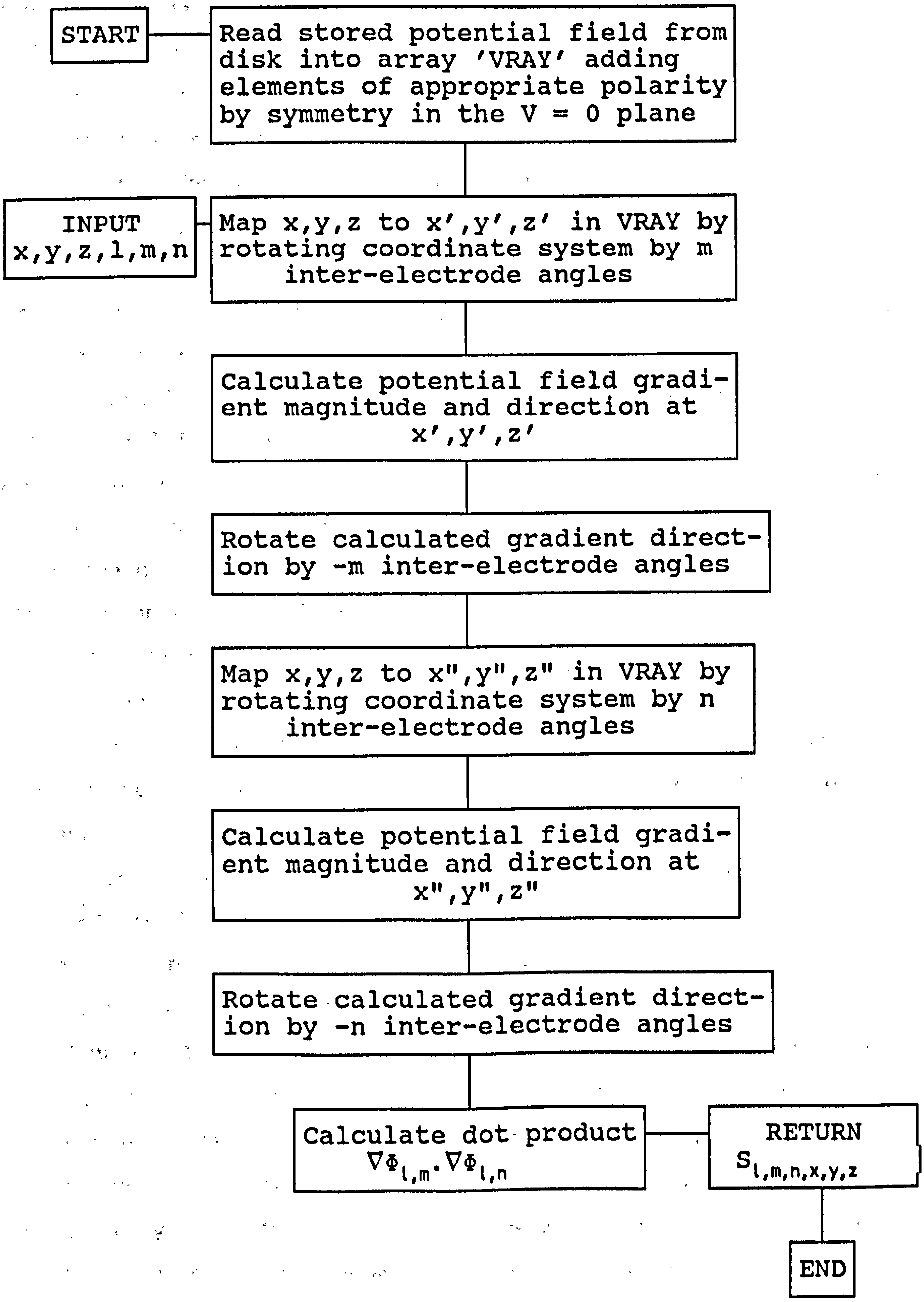

Figure 3.3
Sensitivity coefficient calculation algorithm.

boundary because of the quantisation of the boundary shape, a sensitivity coefficient of zero is returned. Various schemes of interpolation to the nearest point inside the boundary were tried, but were not found to produce any significant improvement whilst increasing the calculation time. The potential gradient is calculated at a point by taking the difference between the two adjacent potential values in the x, y, and z directions and combining the components to give the vector magnitude and direction (figure 3.4). At the Neumann boundaries, the gradient normal to the boundary is zero by definition. The calculations were carried out using double precision floating point arithmetic.

Figure 3.5 shows three examples of sensitivity distributions calculated for the plane l = 0. Because the sensitivity coefficients are signed and have a very large dynamic range, it is necessary to compress the data so that it can be displayed. The images of figure 3.5 were produced by taking the modulus and then the logarithm of the sensitivity coefficient values. Figure 3.5a shows the sensitivity distribution for m = n = 0, which is everywhere positive and, for unit drive current, takes the value (from equation 2.18) of $|\Phi_{l,m}|\,|\Phi_{l,n}|$. Figure 3.5b shows the distribution for m = 0 and n = 4 which demonstrates null lines joining the current drive and voltage sense electrodes. Between the null lines, the sensitivity values are positive and outside the lines, negative. Figure 3.5c shows the distribution for m = 0 and n = 8 and demonstrates the null lines more clearly. The sensitivity values are again positive between the null lines and negative elsewhere. Figures 3.5b and 3.5c can be compared to the sensitivity distributions obtained by Jossinet and Kardous (1987) as a result of physical experiments using a similar geometry, in which the same features are evident.

A numerical test of the validity of the sensitivity coefficient algorithm was carried out using equations 2.11, 2.17 and 2.18 applied to the case of a uniform multiplicative change in resistivity throughout the bounded volume. In this case, for constant current drive, the potential fields $\Phi_{l,m}$ and $\Phi_{l,n}$ are unaltered apart from being scaled by the multiplying factor, and the voltage gradient profile $\delta V(m,n)$ calculated will be related to the unperturbed voltage gradient profile V(l,m,n) by the scaling constant, k. Thus,

$$V(l,m,n) - k\int_x\int_y\int_z S_{l,m,n,x,y,z}\ .dxdydz \qquad (3.2)$$

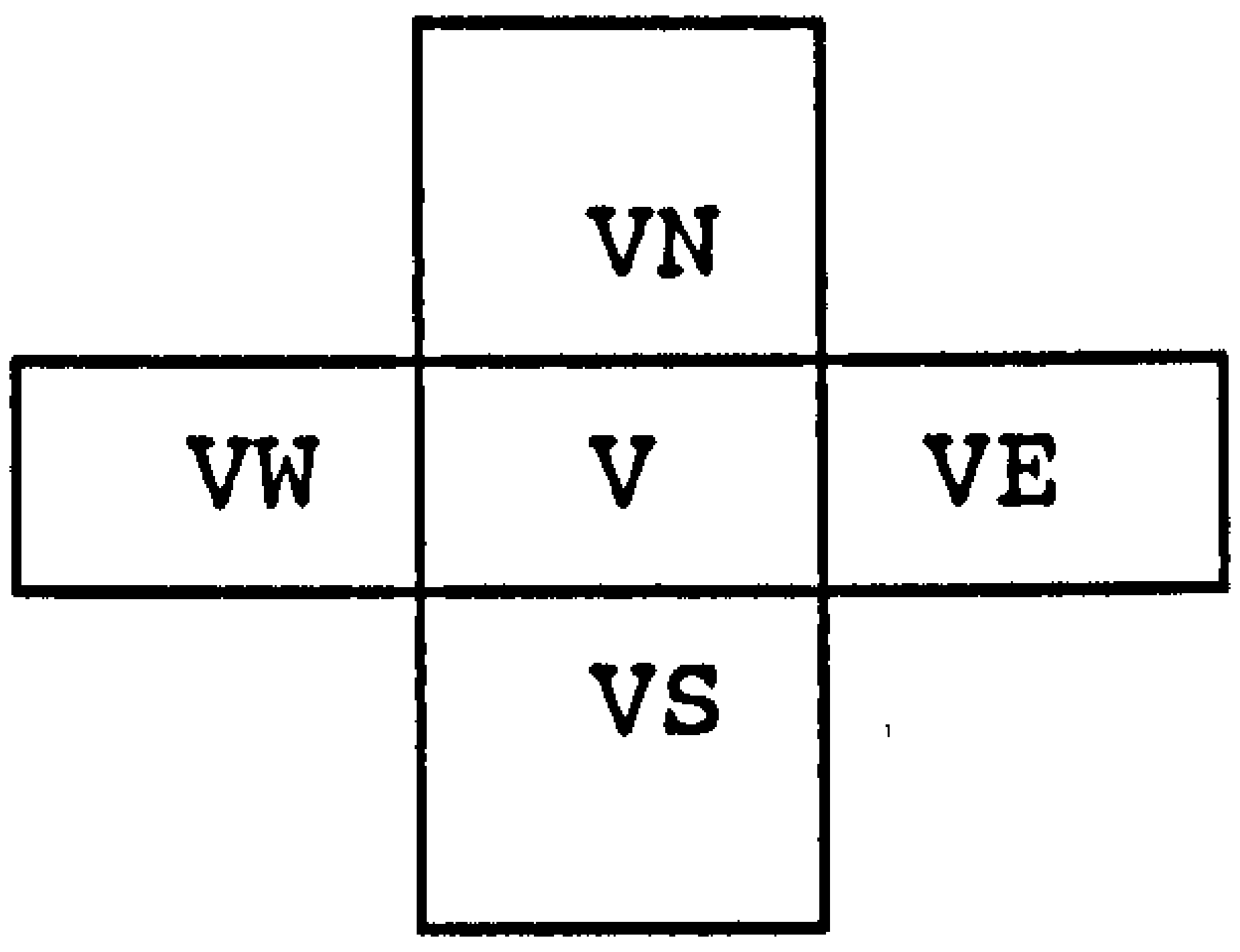

X gradient $G_x = VW - VE$

Y gradient $G_y = VN - VS$

Gradient magnitude = $\sqrt{G_x^2+G_y^2}$

Gradient directon = $\tan^{-1}\left(\frac{G_y}{G_x}\right)$

At (say E) Neumann boundary:

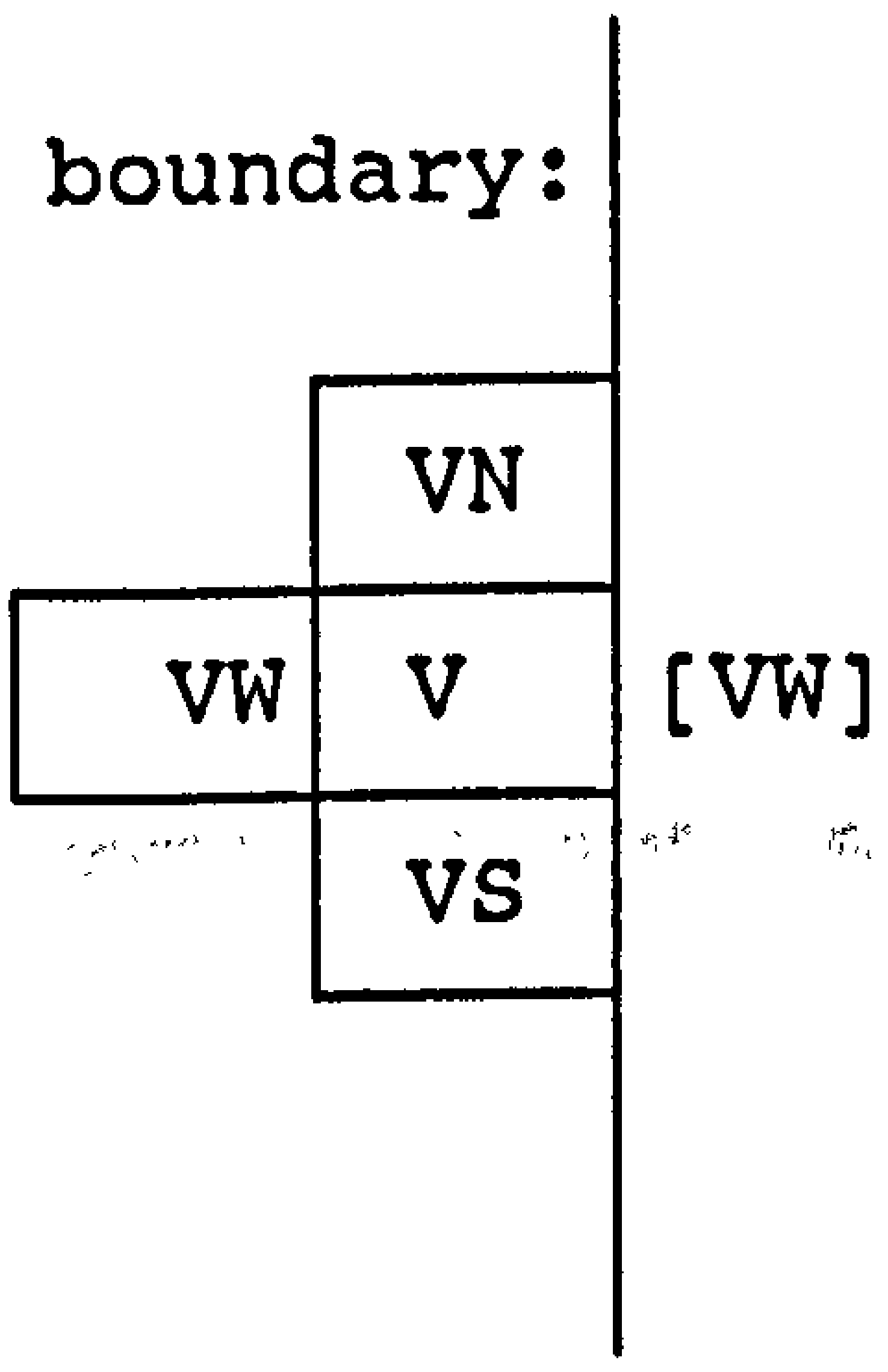

X gradient $G_x = VW - VW = 0$

Figure 3.4

Geometry of potential field gradient calculation (2-D).

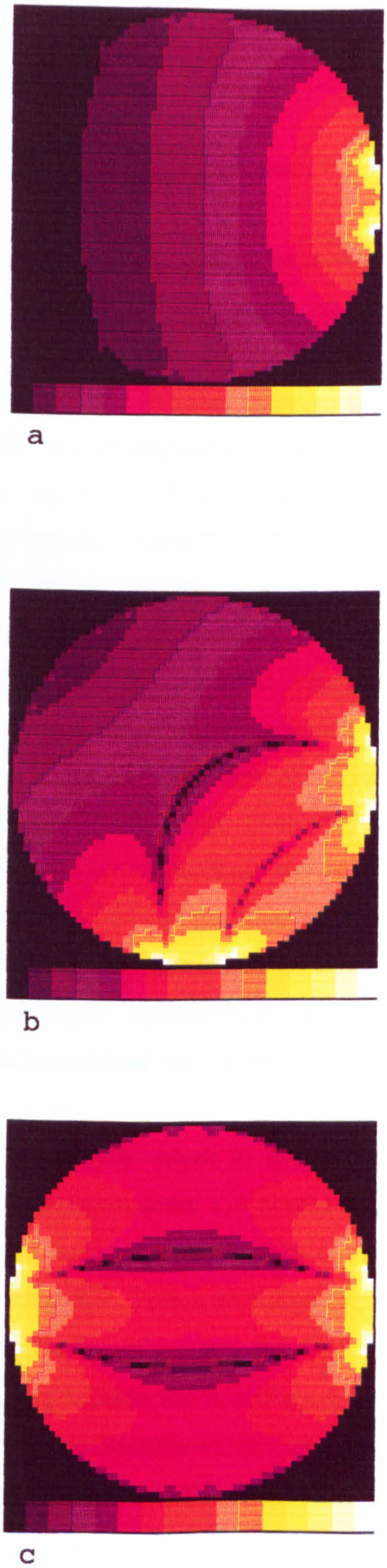

Figure 3.5
Sensitivity distributions for the plane l=0 calculated for (a) m=0 n=0, (b) m=0 n=4 and (c) m=0 n=8.

which can be approximately evaluated as

$$V(l,m,n) - k' \sum_{x} \sum_{y} \sum_{z} S_{l,m,n,x,y,z} \qquad (3.3)$$

using the simulation program, where k' is a new scaling constant which takes account of the now finite dimensions of the volume element in the x, y and z directions.

Table 3.1 shows a comparison between V(l,m,n) as calculated using the sensitivity coefficients, and V(l,m,n) as calculated using the FDM for m = 0 to 3. By symmetry, the results repeat for m > 3. The values calculated by the FDM have been scaled to make direct comparison more convenient.

It is clear from the table that the profiles calculated using equation 3.3 are in poor agreement with those produced by the FDM. A closer examination of the calculation process revealed that the final calculated voltage gradient values were the sum of numerically much larger positive and negative sensitivity coefficient values, especially at positions close to the current drive and voltage sense electrodes where the field gradients are steepest. Thus an error in a few peripheral sensitivity coefficient values is enough to produce the effect seen in table 3.1. Such errors are almost unavoidable when using a field generated using the FDM in an application where the coordinate system must be rotated, as the cartesian coordinate system is not rotationally symmetrical, and the FDM produces a approximation to the field which is constant throughout each volume element rather than known at a true point.

Linear interpolation between data values in the x,y plane of the potential distribution (not needed in the z direction since z = l) was added to the sensitivity coefficient calculation algorithm but was not found to produce a significant improvement on the results of table 3.1. This was not unexpected as the problem was clearly being caused at positions very close the tank wall boundary of the simulation and no extra field values outside the boundary are available to make the required interpolation. Due to the considerable extra computation time required by the interpolation this step in the calculation was dropped.

FDM	m = 0	m = 1	m = 2	m = 3
73438.9	477209.6	783289.6	470884.3	783289.6
36384.4	87738.5	198107.6	198107.6	87738.5
208.8	-188.4	-339.1	-188.4	-350.5
55.7	31.8	31.8	2.1	2.1
24.5	44.6	32.6	30.8	32.6
14.0	5.9	5.8	5.8	5.9
9.6	-7.1	-13.4	-7.1	-14.5
7.7	7.8	7.8	5.9	5.9
7.2	18.9	15.1	14.6	15.1

Table 3.1
Comparison between voltage gradient profile produced by finite differences method and profiles produced using calculated sensitivity coefficients (equation 3.2) for current drive electrode pairs, m = 1 to 3.

3.5 Calculation of voltage gradient profiles and voltage gradient perturbations

Given that the results of table 3.1, together with the detailed examination of the calculation process, indicate that sensitivity coefficient values produced by the simulation program for positions on or very close to the boundary may be inaccurate, the problem with evaluating the voltage gradient profiles, V(l,m,n), can be circumvented simply by using the values obtained directly from the stored potential field i.e column 1 in table 3.1. For the single pixel cross-section test object described in section 3.2, the changes in these profiles, δV(l,m,n), can be evaluated simply as

$$\delta V(l,m,n) - A\sum_{z} S_{l,m,n,x_p,y_p,z} \tag{3.4}$$

where (x_p,y_p) is the position in the plane of the extended point object and A is its amplitude. Since it is being argued that no resistivity changes take place elsewhere within the bounded volume, the amplitude, A, cannot be used to simulate a relative change in resistivity between the object and the background as this is always infinity. A merely scales δV(l,m,n) with respect to V(l,m,n).

Using this approach, it can be seen that provided the position of the object (x_p,y_p) is not brought too close to the boundary, δV(l,m,n) can be evaluated without involving suspect sensitivity coefficient values.

3.6 Summary of chapter 3

The 'forward problem' in electrical impedance tomography is that of calculating a set of voltage and voltage perturbation profiles from knowledge of the conductivity distribution of the object and the currents applied to it. In this chapter, a three-dimensional software simulation of the forward problem has been developed which should allow the behaviour of the type of image reconstruction approach proposed in section 2.5 to be studied.

CHAPTER 4

RECONSTRUCTION ALGORITHM DEVELOPMENT

4.0 Introduction

Having implemented a simulation of the 'forward problem' of creating sets of voltage profile data from a defined distribution of resistivity changes, the foundation has been laid for a quantitative assessment of the performance of algorithms intended to approximately solve the 'inverse problem' of reconstructing a cross-sectional image through the distribution of resistivity changes from the voltage profile data. The class of algorithms under study in this section is based upon the concept of weighted backprojection using sensitivity coefficients introduced in section 2.5. All the reconstructions are dynamic (i.e reconstructions of a distribution of resistivity changes), single pass (i.e the potential fields from which the sensitivity coefficients are derived are not re-evaluated using the reconstructed resistivity distribution) and, except where specifically stated, include the effects of multiple plane data sets.

4.1 Initial trials of reconstruction algorithms employing sensitivity coefficients for weighted backprojection

An extended point object of amplitude $A = 1$ was reconstructed initially at eight positions corresponding to 0, 4, 8, 12, 16, 20, 24 and 28 pixels from the centre of the image along the radius $y = 0$. All reconstructed images are nominally for the plane $z = 0$ as defined in figure 3.1. The reconstructed quantity is denoted as pixel value, $P(x,y,z)$, the dimensionality of which is not analysed at this stage.

The resulting images were stored both as scaled 8-bit values for display purposes and in their original 64-bit floating point form for further analysis. The images were displayed using the 8-bit versions transformed via a 'hot iron' colour scale often used in nuclear medicine, which was found to give a better dynamic range of display than monochrome grey-scale. The images shown as figures were produced using a 16-level version of the hot iron colour scale adapted to suit a colour printer. Because the truncation of the image data to 8-bits was carried out by mapping the minimum value in the image to 0 and the maximum value to 255, it is not possible to directly compare amplitudes between images (this data is supplied in tabular form) and images containing negative going resistivity changes are displayed with an elevated zero level.

The most simplistic implementation of the weighted backprojection concept of section 2.5 is one in which the reconstructed value, P(x,y,z), is related to the set of normalised voltage gradient changes (from equation 2.23) as

$$P(x,y,z) = \sum_{l}\sum_{m}\sum_{n} S_{l,m,n,x,y,z}\left(\frac{\delta V}{V}\right)_{l,m,n} \tag{4.1}$$

This algorithm, not surprisingly, does not produce a recognisable image due to the very large range of sensitivity coefficient values encountered as the radial distance from the centre of the image changes. To counteract this effect, and to produce a backprojection where the total sensitivity to the voltage profile data for each volume element is normalised to unity, it is necessary to include as a denominator the sensitivity coefficient total for each volume element to give

$$P(x,y,z) = \frac{\sum_{l}\sum_{m}\sum_{n} S_{l,m,n,x,y,z}\left(\frac{\delta V}{V}\right)_{l,m,n}}{\sum_{l}\sum_{m}\sum_{n} S_{l,m,n,x,y,z}} \tag{4.2}$$

Images reconstructed using this algorithm are shown in figure 4.1 a-h and the image statistics are given in table 4.1. The images show an area of raised resistivity approximately corresponding to the position of the object. For objects close to the boundary, negative resistivity changes associated with the positive change at the position of the object can also be seen. Table 4.1 shows that negative resistivity changes are recorded for all object positions, but their magnitude only becomes significant with respect to the (positive) object amplitude close to the boundary. The reconstructed PSF amplitudes (given by the maximum pixel values) are reasonably constant except for a rise at $x_p = 28$.

A comparison between the nominal and reconstructed object positions in table 4.1 shows that there is a distortion of the image plane which takes the form of drawing objects near the centre of the image further in towards the centre whilst leaving the positions of objects close to the boundary unchanged. This is not a

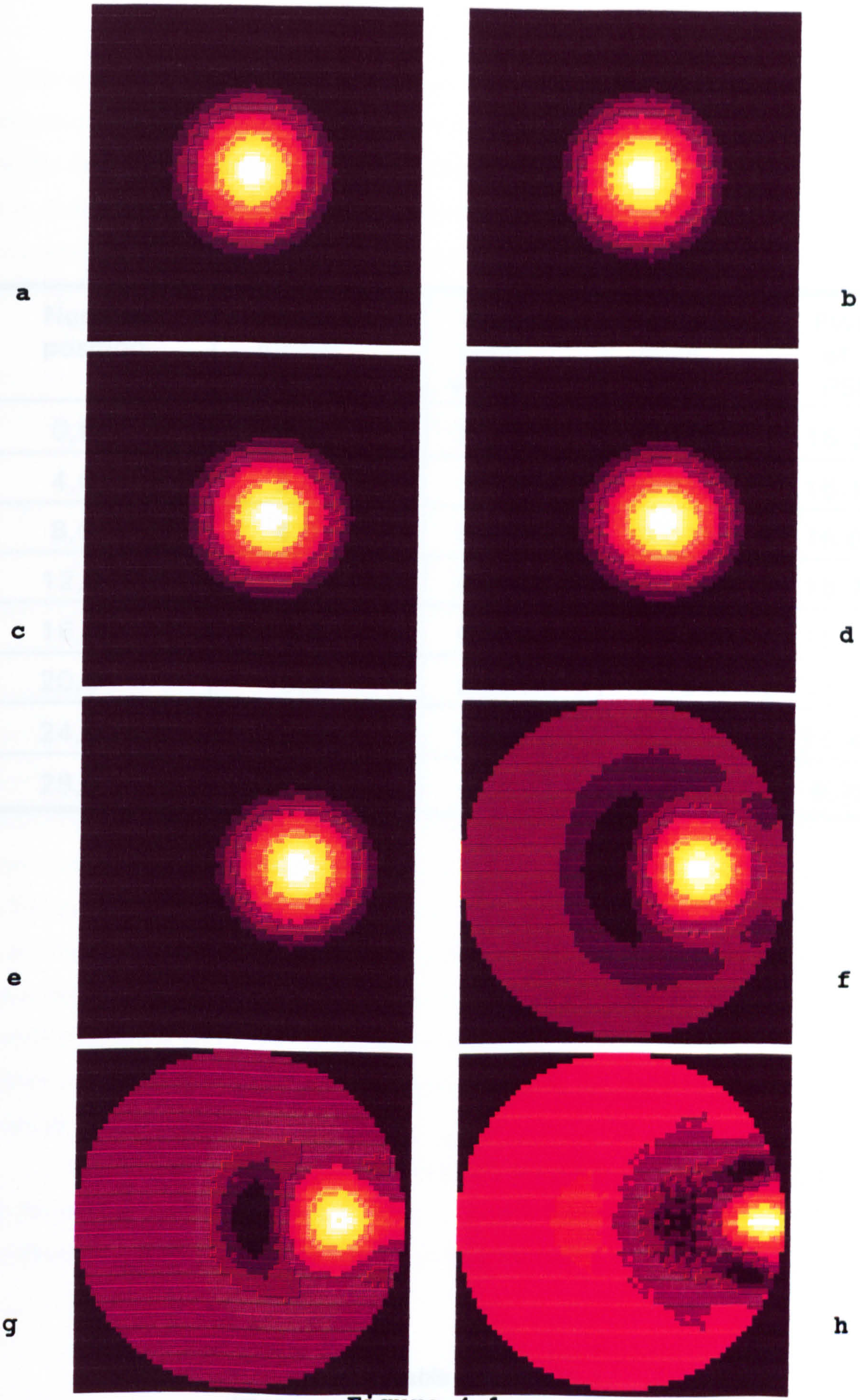

Figure 4.1

Images of a simulated point test object at nominal distances (a-h) 0, 4, 8, 12, 16, 20, 24 and 28 pixels from the axis of the cylindrical boundary. Reconstructed using equation 4.2.

Nominal position	Reconstructed position	Maximum pixel value	Minimum pixel value	FWHM of PSF
0,0	0,0	0.9887	-0.0131	16.22
4,0	2,0	0.9733	-0.0136	16.15
8,0	4,0	0.9382	-0.0152	16.07
12,0	7,0	0.8882	-0.0190	15.79
16,0	11,0	0.8656	-0.0335	15.07
20,0	15,0	0.8254	-0.1341	13.75
24,0	20,0	0.9851	-0.3593	11.44
28,0	28,0	1.4632	-0.6888	8.78

Table 4.1
Image statistics for the images of figure 4.1 which were reconstructed using the algorithm of equation 4.2.

fundamental flaw of the algorithm, since there is no reason to assume that the image space obtained as the result of this weighted backprojection operation should be the final image space of the complete reconstruction process. What must be true, however, is that there exists a one-to-one position mapping between the image space resulting from the application of the weighted backprojection operation and the object space, a requirement which is satisfied by the results obtained.

The FWHM column of table 4.1 shows a decrease in PSF width towards the boundary, although the measurement accuracy close to the boundary is somewhat compromised by the presence of the adjacent areas of negative resistivity change.

4.2 Trials of alternative weighted backprojection strategies

Although the images obtained by the application of the weighted backprojection operation defined by equation 4.2, were considered to be encouraging, an investigation of a large number of related weighted backprojection strategies was carried out to see if any improvement could be obtained. Of particular interest were the areas of negative resistivity change associated with large positive changes (and vice versa, the production of positive changes by the application of a large negative change: this effect was confirmed by setting the object amplitude, A, to a negative value) and the increase in point amplitudes close to the boundary. These effects were considered to represent a serious impediment to any attempt to apply spatial frequency filtering techniques to the images, since these techniques can only be applied to linear systems in which the PSF is shift-invariant. This condition clearly cannot be met for the images of figure 4.1 by any spatial transformation due, to the varying amplitude with object position of the spurious negative resistivity changes.

The first area of investigation concerned the amplitude correction term, i.e the denominator, of equation 4.2. Since it is clear from the earlier studies of the sensitivity coefficient calculation (section 3.4) that the sum

$$\sum_{l}\sum_{m}\sum_{n} s_{l,m,n,x,y,z} \tag{4.3}$$

can be made up of individually much larger magnitude positive and negative sensitivity coefficient values, it does not seem self evident that this term represents the "overall sensitivity" of the volume element at (x,y,z) to the voltage measurement data set. Various modifications, including root-mean-square mean, sum of moduli, and decomposition into separate positive and negative sensitivity coefficient images were tried without producing any improvement. Table 4.2 lists some of the algorithms tried and summarises the main features of the resulting PSF images.

Other variations tried included rearrangements of the whole backprojection algorithm and amplitude normalisations of the voltage gradient profiles for each current drive orientation. Some of these algorithms are listed in table 4.3 together with the main features of the resulting PSF images.

A third approach was based on the analysis of Barber and Brown (1986, 1987) of the 2-dimensional case with dipole current drive. This analysis employs a transformation to a coordinate system in which distances along the boundary are expressed in a direction, U, in which dV/dU is a constant, E. The modulus of the Fourier transform, $B(f_u)$, of the voltage gradient produced by a small perturbation in log resistivity at a point a distance q from the boundary is given as

$$B(f_u) = \frac{1}{2}E|f_u|\pi e^{-q|f_u|} \qquad (4.4)$$

where f_u is the spatial frequancy variable. This expression includes a term, $|f_u|$, whose response in spatial frequency space increases linearly with frequency. This is equivalent to the application of a 'ramp' spatial frequency filter to the point response profile. As this ramp filter is known to be applicable as the inverse to the spatial frequency modification that takes place as the result of the backprojection operation used in X-ray computed tomography (e.g Barrett and Swindell, 1981), the result of this analysis has been interpreted as being advantageous to an EIT reconstruction based on a backprojection method. This interpretation is based on the unsubstantiated assumption that the 'built-in' ramp filter is also appropriate to EIT reconstruction. The result could also, however, be interpreted as the cause of the negative overshoots seen in figure 4.1 and therefore as an effect to be removed if possible.

The existence of negative overshoots in the simulated boundary voltage gradients was established by observing the normalised voltage gradient changes

Algorithm	Comments
$P(x,y,z) = \frac{\sum_{l}\sum_{m}\sum_{n} S_{l,m,n,x,y,z}\left(\frac{\delta V}{V}\right)_{l,m,n}}{\sum_{l}\sum_{m}\sum_{n}\lvert S_{l,m,n,x,y,z}\rvert}$	Amplitude increases to periphery. Positional accuracy quite good.
$P(x,y,z) = \frac{\sum_{l}\sum_{m}\sum_{n} S_{l,m,n,x,y,z}\left(\frac{\delta V}{V}\right)_{l,m,n}}{\sqrt{\sum_{l}\sum_{m}\sum_{n} S^{2}_{l,m,n,x,y,z}}}$	Amplitude decreases to periphery. Positional accuracy poor.
$P(x,y,z) = \frac{\sum_{l}\sum_{m}\sum_{n} S_{l,m,n,x,y,z}\left(\frac{\delta V}{V}\right)_{l,m,n}}{\sqrt[3]{\sum_{l}\sum_{m}\sum_{n} S^{2}_{l,m,n,x,y,z}}}$	Amplitude increases to periphery. Positional accuracy quite good.
$P(x,y,z) = \frac{\sum_{l}\sum_{m}\sum_{n} S_{l,m,n,x,y,z}\,\delta V(l,m,n)}{\sqrt{\sum_{l}\sum_{m}\sum_{n} S^{2}_{l,m,n,x,y,z}}}$	Amplitude increases steeply towards periphery. Positional accuracy quite good.

Table 4.2

Some examples of weighted backprojection algorithms with alternative amplitude normalisation terms, with comments on the main features of the resulting PSF images.

Algorithm	Comments
$P(x,y,z) = \frac{\sum_{l}\sum_{m}\sum_{n} S_{l,m,n,x,y,z}\,\delta V(l,m,n)}{\sum_{l}\sum_{m}\sum_{n} S_{l,m,n,x,y,z}}$	Amplitude increases sharply to periphery. Positional accuracy good.
$P(x,y,z) = \frac{\sum_{l}\sum_{m}\sum_{n} S_{l,m,n,x,y,z}\left[\frac{\delta V(l,m,n)}{\sqrt{\sum_{n}\left(\frac{\delta V}{V}\right)^{2}_{l,m,n}}}\right]}{\sqrt{\sum_{l}\sum_{m}\sum_{n} S^{2}_{l,m,n,x,y,z}}}$	Amplitude increases to periphery. Positional accuracy poor.
$P(x,y,z) = \frac{\sum_{l}\sum_{m}\sum_{n} S_{l,m,n,x,y,z}\left[\frac{\delta V(l,m,n)}{\sqrt{\sum_{N}\delta V(l,m,n)^{2}/N}}\right]}{\sqrt{\sum_{l}\sum_{m}\sum_{n} S_{l,m,n,x,y,z}}}$	Amplitude decreases to periphery. Positional accuracy good.
$P(x,y,z) = \frac{\sum_{l}\sum_{m}\sum_{n} S_{l,m,n,x,y,z}\left[\frac{\delta V(l,m,n)}{\sum_{N}\left(\frac{\delta V}{V}\right)^{2}_{l,m,n}}\right]}{\sqrt{\sum_{l}\sum_{m}\sum_{n} S^{2}_{l,m,n,x,y,z}}}$	Amplitude varies. Will not image simultaneous central and peripheral points.

Table 4.3
Some examples of experimentally investigated alternative weighted backprojection algorithms, with comments on the main features of the resulting PSF images.

$(\delta V/V)_{l,m,n}$ for a fixed current drive orientation of m = 0 and an extended point object at various positions along the line y = 0. Some examples of the resulting profiles are shown in figure 4.2. In an attempt to attenuate these negative overshoots, a convolution filter kernel equivalent to 1/U (the inverse of the ramp filter) was applied to the $(\delta V/V)_{l,m,n}$ profiles, but the resulting images showed little if any improvement in the negative overshoots and displayed increased PSF widths due to the blurring effect of the 1/U filter. The convolution step was therefore dropped.

Despite the numerous and increasingly complex attempts to improve on the performance of the weighted backprojection algorithm of equation 4.2, no such improvement was found and the development of this algorithm was resumed.

4.3 A more detailed examination of the preferred weighted backprojection algorithm

In section 2.1 it was established that the parameter imaged in dynamic EIT should be change in log resistivity, $R(x,y,z)$. Restating the 'forward problem' in terms of the relationship between the distribution of small perturbations in $R(x,y,z)$ to normalised changes in boundary potential given in equation 2.23 now for the case of a multiple layer electrode array,

$$\left(\frac{\delta V}{V}\right)_{l,m,n} = \frac{\sum_x \sum_y \sum_z s_{l,m,n,x,y,z}\, \delta R(x,y,z)}{\sum_x \sum_y \sum_z s_{l,m,n,x,y,z}} \tag{4.5}$$

and the proposed approximation to the 'inverse problem'- the weighted backprojection algorithm given in equation 4.2,

$$P(x,y,z) = \frac{\sum_l \sum_m \sum_n s_{l,m,n,x,y,z} \left(\frac{\delta V}{V}\right)_{l,m,n}}{\sum_l \sum_m \sum_n s_{l,m,n,x,y,z}} \tag{4.6}$$

it can be seen that a strong symmetry exists between the two.

Considering the case of a small uniform multiplicative change in resistivity, ρ, by a factor, k, throughout the bounded volume, from equation 2.22,

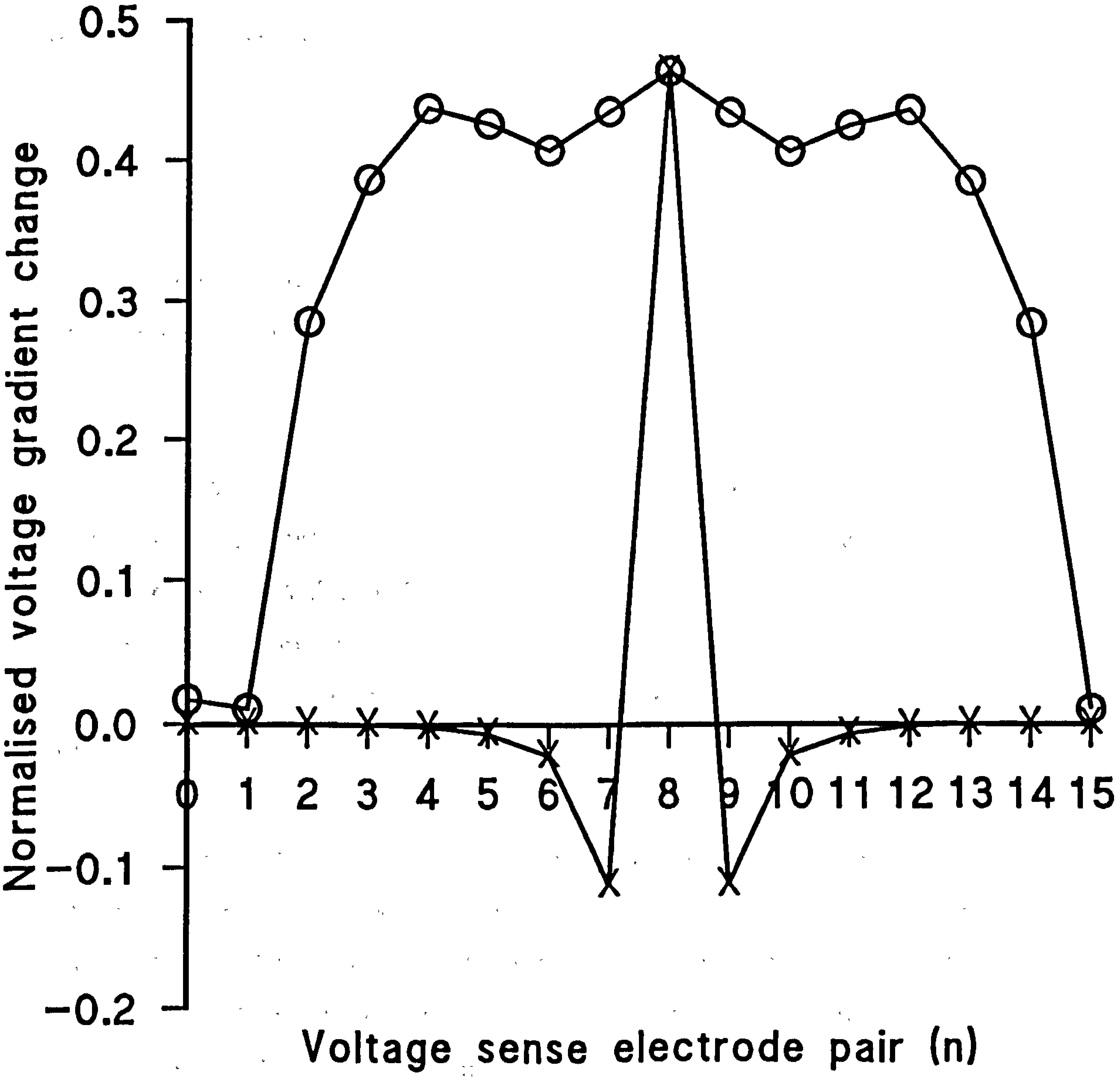

Figure 4.2

Normalised voltage gradient changes for insulating object close to current drive electrodes (O), and object close to voltage sense electrodes (X).

$$\delta R(x,y,z) = \frac{\delta\rho}{\rho} = k-1 \tag{4.7}$$

Since the mutual impedance for any measurement, $Z_{l,m,n} \propto \rho$, for a constant current from equation 2.11, V(l,m,n) $\propto \rho$, and for the case of a multiplicative change,

$$\left(\frac{\delta V}{V}\right)_{l,m,n} = k-1 \tag{4.8}$$

a constant for all l,m,n. Substituting for $(\delta V/V)_{l,m,n}$ in equation 4.6, the sensitivity coefficient terms can be cancelled, and substituting from 4.7,

$$P(x,y,z) = k-1 = \delta R(x,y,z) \tag{4.9}$$

For the general case of a non-homogeneous change in resistivity, the images of figure 4.1 suggest that the distribution of P(x,y,z) is an approximation to δR(x,y,z) with each value of P(x,y,z) being affected by its surroundings due to the point spread functions in the image plane and between image planes.

In section 2.5, a set of specifications on which the image reconstruction process would be based were stated. Amongst these were that the reconstruction algorithm would in the first instance be 'single pass' (i.e the potential fields from which the sensitivity coefficients are derived would not be re-evaluated using the reconstructed resistivity distribution) and that the algorithm would therefore only apply to small changes in log resistivity (i.e changes so small that the potential fields within the bounded volume would not be significantly changed from the case of uniform resistivity). These assumptions are clearly not being satisfied when using the extended point object in this simulation. As explained in section 3.5, the amplitude of the point object in this case acts only as a scaling factor and does not change the contrast of the object. Since the sensitivity coefficient calculation is based on the use of stored Laplace potential fields, the current flow within the bounded volume is fixed. This will result in the calculated perturbation profile δV(l,m,n) having an anomalously large response to the change in resistivity at the object position, and an anomalously small response to the background resistivity surrounding the object, both due to the assumption that the pattern of current flow is unchanged from the case of uniform resistivity. The real physical situation is that the introduction of an insulating rod into the test tank will cause a large reduction in current flow at the position of the rod and an increase close to it corresponding to the displaced current. This effect is seen in the perturbation profiles shown in figure 4.2.

The overshoot effect seen in figure 4.1 is clearly consistent with departure from the assumption of small resistivity changes. This conclusion is reinforced by the image statistics in table 4.1 which show that the reconstructed object amplitude is anomalously high where it is close to the electrodes and subjected to the highest current densities, and that objects close to the electrodes produce the greatest amount of overshoot for the same reason. Since the assumption of unchanged current flow has been invoked both for the calculation of the voltage profile data, and for its reconstruction into an image, the resulting artifacts would be expected to be less severe for non-simulated data and to become negligible for the small resistivity changes for which the algorithm was defined.

4.4 Transformation of the image space as a preliminary to spatial frequency filtering

By analogy with X-ray computed tomography, where the backprojection process produces an image containing a non-uniform distribution of spatial frequencies (e.g Barrett and Swindell, 1981), it would be expected that the weighted backprojection operation described in the preceding sections will also need to be accompanied by some form of spatial frequency filtering operation. For such an operation to be applicable, the system PSF must be shift-invariant, a requirement clearly not met by the images of figure 4.1. Disregarding the overshoot effect which is explained above, the values of FWHM for the reconstructed PSFs (table 4.1) show a change with distance from the electrodes. To make a filtering operation possible it is therefore necessary to transform the existing image space to one in which the width of the PSF, and hence the spatial resolution, is constant at all points. This will be termed the equi-resolution space.

The most straightforward way to make such a transformation would be to relate the resolution (defined for this discussion as the reciprocal of the PSF FWHM) to radial position within the image space and from this to produce an appropriately transformed radial position in the equi-resolution space. This approach, however, contravenes one of the requirements for the reconstruction algorithm listed in section 2.4, namely that the algorithm should not be constrained by the imposition of artificial boundary conditions. Thus the concept of a radial position in either space does not apply when generalised body shapes are being considered. An approach more consistent with the overall requirements of the reconstruction algorithm is to find a causal relationship between the resolution at any point in the image space and some parameter which can be evaluated purely from knowledge of the real boundary conditions, and then to make the transformation to the equi-resolution space in accordance with this relationship.

Different analyses of the EIT reconstruction problem for the case of a 2-dimensional circular region by both Barber and Brown (1986) and Seagar et al (1987) give the same result for the variation of spatial resolution with radial position,

$$W \propto \frac{1}{(1 - c^2)} \tag{4.10}$$

where W is a measure of spatial resolution, and c is the radial position normalised for a circular region of unit radius. The analysis of Seagar et al (1987) continues to give an expression for the variation of overall sensitivity with radial position,

$$S_{total} \propto \frac{1}{(1 - c^2)^2} \tag{4.11}$$

where S_{total} is a measure of the total overall sensitivity of the measured data set to a point change in conductivity at a normalised radius, c. Thus it would be expected that,

$$W \propto \sqrt{S_{total}} \tag{4.12}$$

In section 4.2 it was concluded, after considerable experimentation, that the overall sensitivity at any point was given simply by the sum of all the sensitivity coefficients used during backprojection. It would therefore be expected that the quantity S_{total} could be evaluated as,

$$S_{total} = \sum_{l} \sum_{m} \sum_{n} S_{l,m,n,x,y,z} \tag{4.13}$$

This sum is already evaluated as the denominator of the weighted backprojection algorithm of equation 4.2.

An investigation of the relationship between the resolution and S_{total} at various positions in the image was carried out using the data from table 4.1 together with some data from extra object positions. In each case the value of S_{total} was taken at the reconstructed position of the point object rather than at its nominal position. The results are plotted in figure 4.3 which shows a convincing linear relationship up to $x_p = 25$. The results for $x_p > 25$ do not fall on the line probably due to inaccuracies in the FWHM measurement caused by the presence of the negative overshoots and possible inaccuracies in S_{total} caused by the difficulty in evaluating sensitivity coefficients at positions close to the electrodes. It was noted that the regression line does not pass through the origin suggesting the presence of an offset on the resolution measurement. The results, however, seem convincing enough to postulate a causal relationship between the total sensitivity at a point and the achievable spatial resolution at that point, and are certainly good enough to use for the purpose of transforming the image space to the required equi-resolution space. It is useful to define a normalised total sensitivity, S_{norm}, as S_{total} normalised to a minimum value of unity i.e

$$S_{norm}(x,y) = \frac{S_{total}(x,y)}{S_{total}(x_m,y_m)} \tag{4.14}$$

where (x_m,y_m) is the position at which the minimum value of S_{total} occurs: the centre of the image for cylindrical boundary conditions. This normalisation is useful as it removes the dependence of the transformation to equi-resolution space on the actual value of S_{total} which, in the simulation, is dependent on various arbitrary constants in the sensitivity coefficient calculation process. (From the definition of the sensitivity coefficient given in equation 2.18 it can be seen, however, that if the drive current, *I*, is known, then the coefficient should be uniquely defined making this normalisation unnecessary.)

If a similarly normalised local magnification factor, $F_{eq}(x,y)$, is defined as

$$F_{eq}(x,y) = \frac{FWHM(x_m,y_m)}{FWHM(x,y)} \tag{4.15}$$

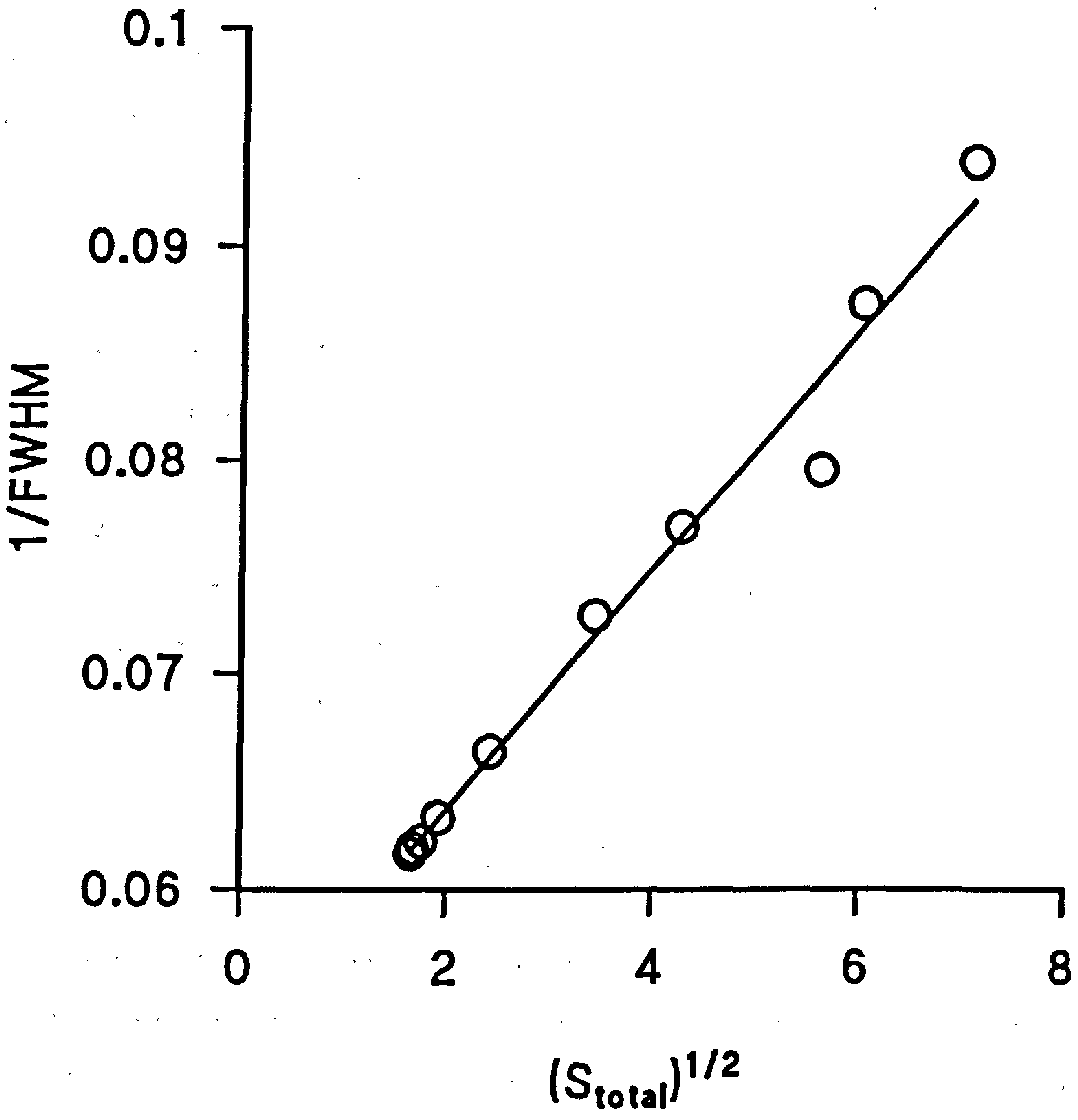

Figure 4.3

Resolution plotted against the square root of the total sensitivity, S_{total}.

then $F_{eq}(x,y)$ gives the magnification factor required at any point in the image to enlarge the FWHM of the PSF to match that at the position of minimum total sensitivity (and maximum PSF width), (x_m,y_m) and thus perform the required transformation to the equi-resolution space.

Figure 4.4 shows the results of figure 4.3 redrawn in terms of S_{norm} and normalised local magnification factor. Using the regression equation for this relationship, the magnification factor required at any point can be calculated from the corresponding value of S_{norm}.

The transformation was implemented as a radial expansion about a central origin using the fact that the transformed radial distance in equi-resolution space, r_{eq}, can be evaluated as a sum of radial increments, i, up to a radius r_{or} in the original space image array each multiplied by the appropriate magnification factor, $F_{eq}(r)$, at the radius of the current increment, r, the magnification factors being calculated from an array of S_{norm} using the relationship of figure 4.4.

$$r_{eq} = i \sum_{r=0,i,2i..}^{r_{or}} F_{eq}(r) \qquad (4.16)$$

This approach does not limit the transformation to circularly bounded images, but does require that the body shape is appropriately centred in the image field. It would, in any case, be expected that most body cross-sections would not be too far removed from cylindrical geometry. The transformation is achieved by stepping through the destination 128 x 128 equi-resolution array and for each pixel calculating the radial direction and distance from the origin. This radial direction is then stepped along in the image and S_{norm} arrays, and a running total of the image space and transformed equi-resolution space radii calculated. When the transformed radial distance is equal to the radial distance of the current pixel in equi-resolution space, the mapping between the two spaces at this position can be made. Linear interpolation in both the radial transformation calculation and between elements in the image and S_{norm} arrays was used to give an even stretching effect. A diagrammatic explanation of the transformation algorithm is given in figure 4.5.

Figure 4.6 a-h shows the images of figure 4.1 as they appear transformed into equi-resolution space. (The central 64 x 64 section of the 128 x 128 equi-resolution array is shown in each case.) Figure 4.7 shows a graph of FWHM against

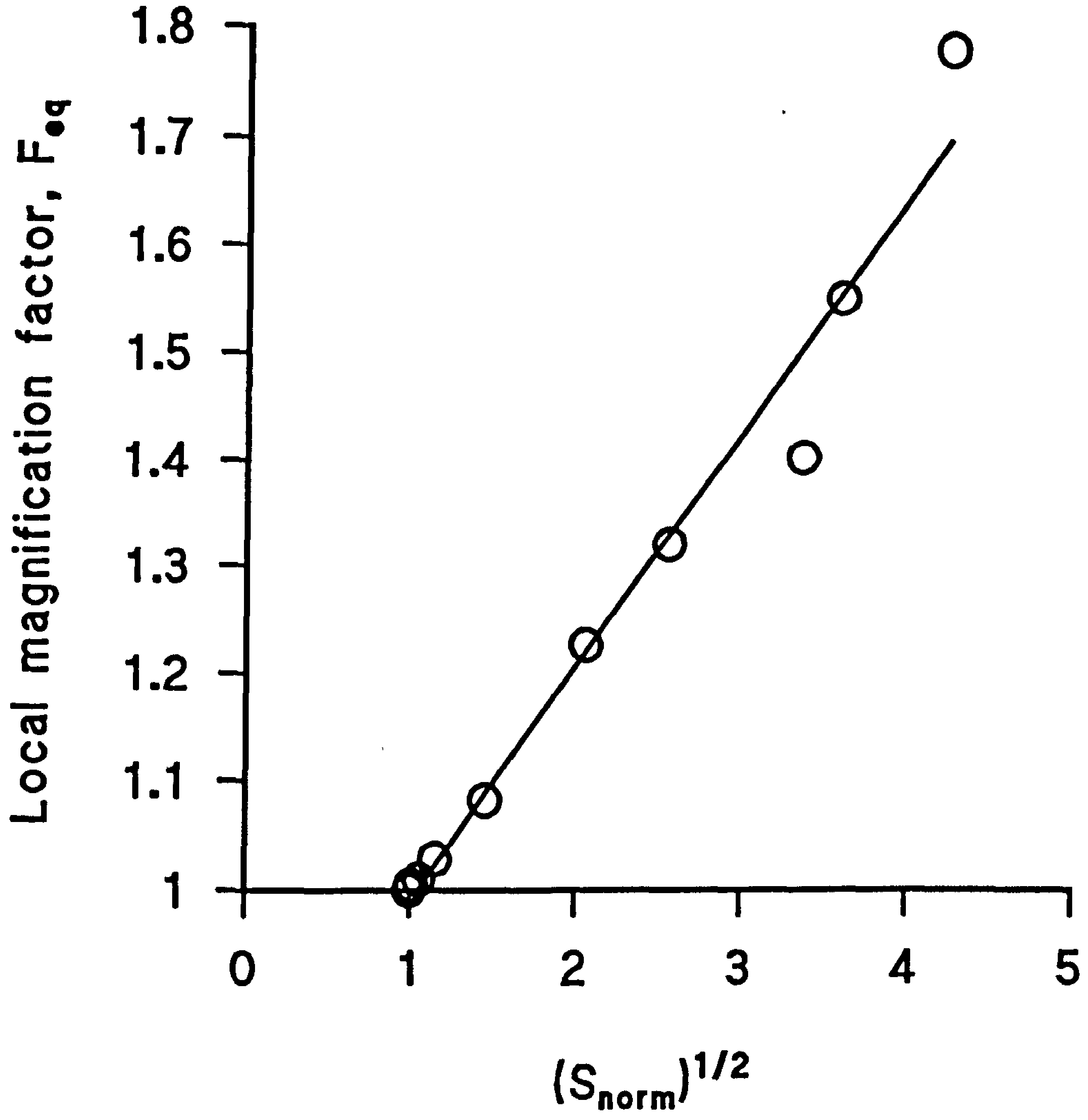

Figure 4.4

Local magnification factor for equi-resolution space transformation plotted against the square root of the normalised total sensitivity.

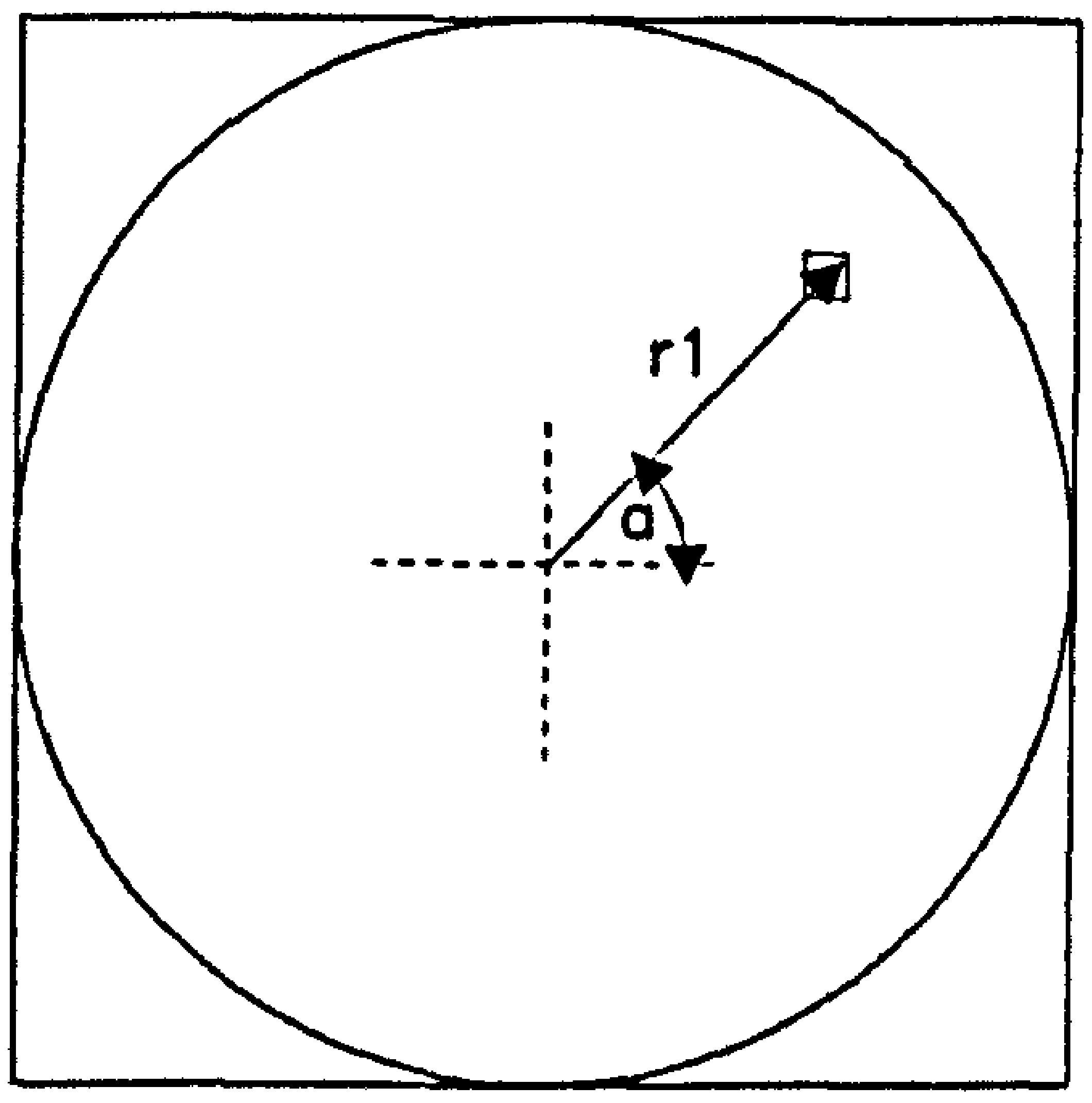

Transformed space

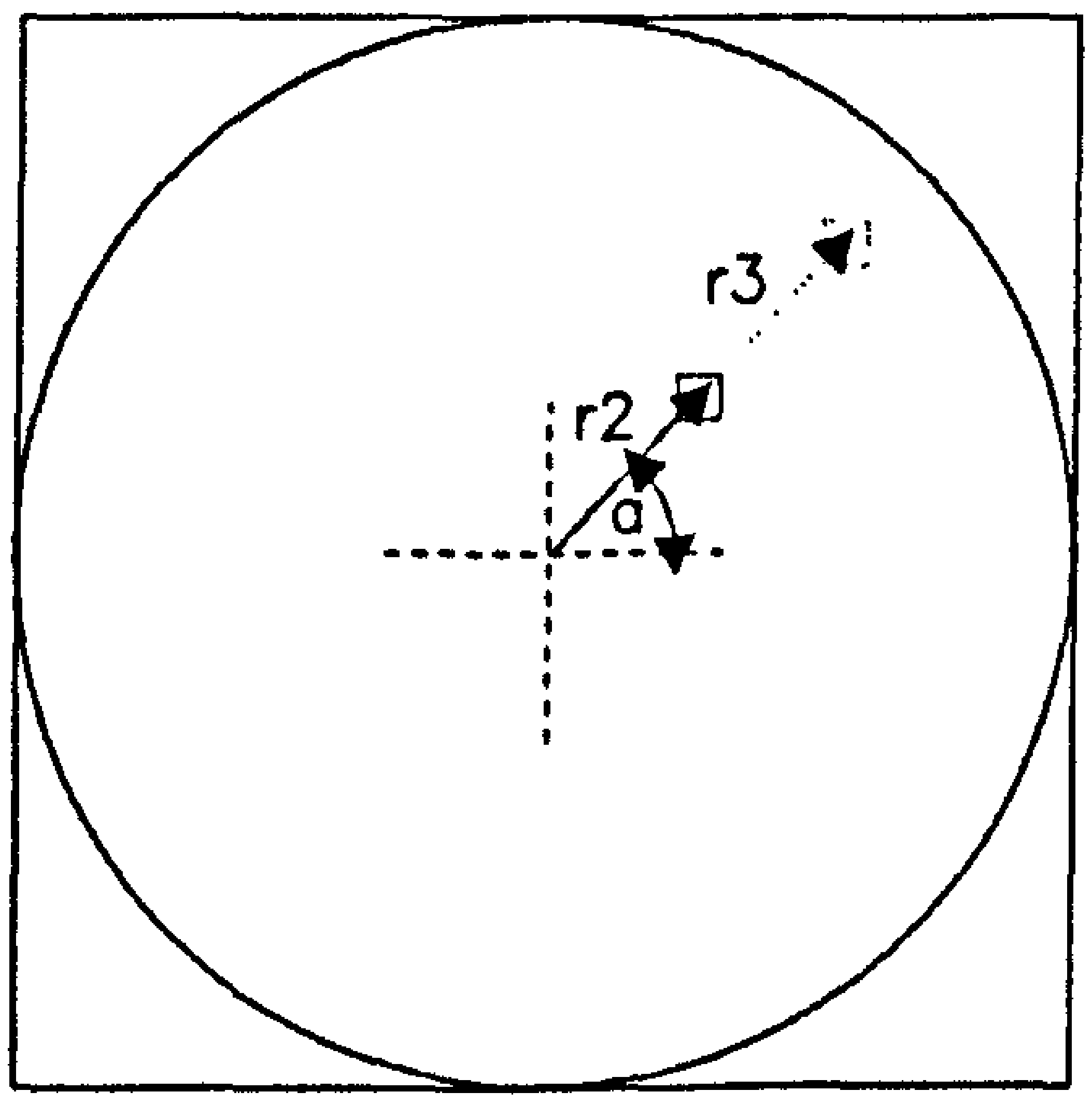

Original space

Figure 4.5

Transformation from original to equi–resolution space. The radius, r1, and angle, a, of the current pixel in the transformed space are calculated, then the radius, r2, is stepped along in the original space and the transformed radius, r3, calculated. When r3=r1, r2 points to the pixel value to be copied.

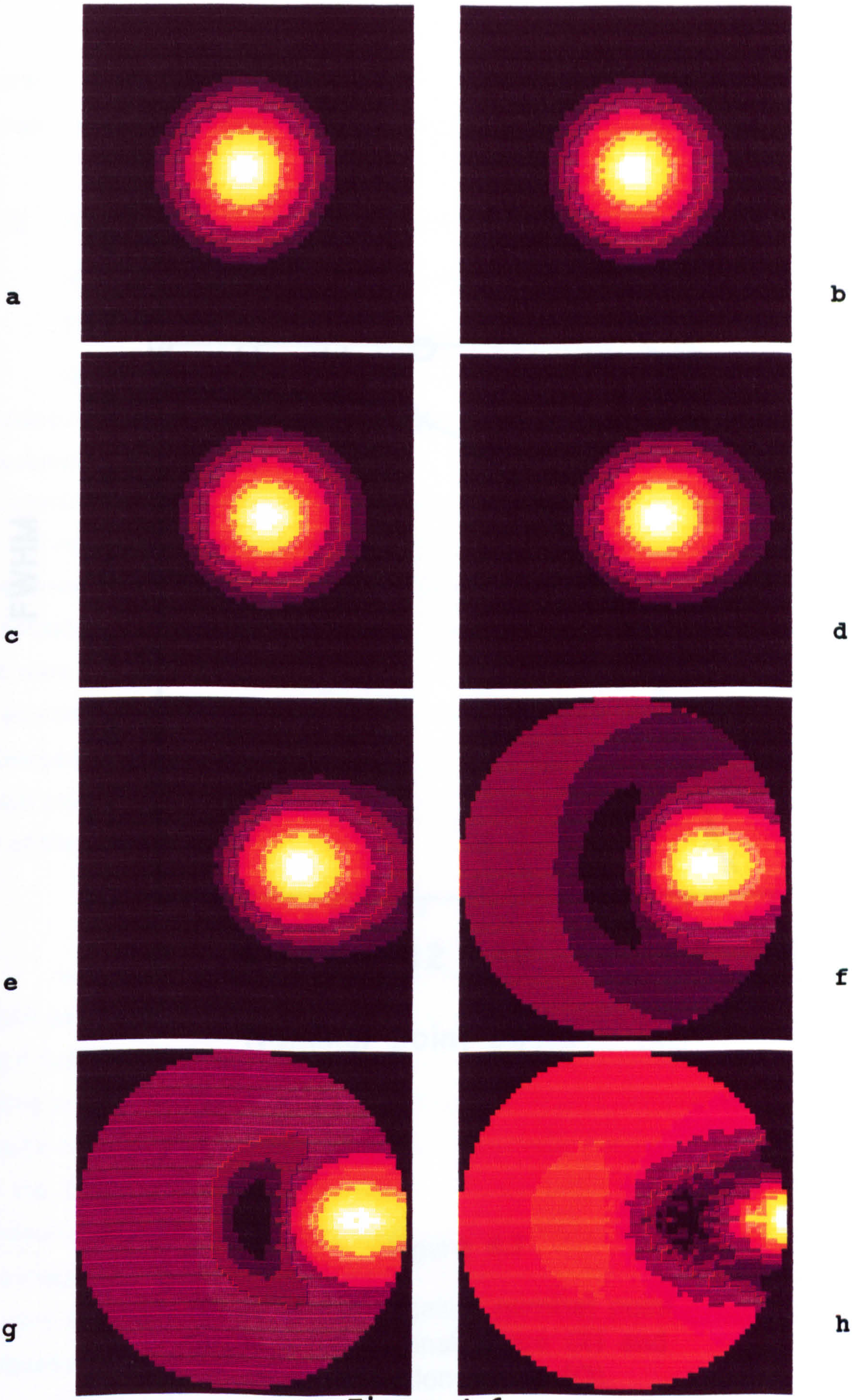

Figure 4.6

The images of figure 4.1 transformed to equi-resolution space using the transformation of equation 4.16 (and figure 4.5). The central 64 X 64 section of the 128 X 128 equi-resolution space matrix is shown.

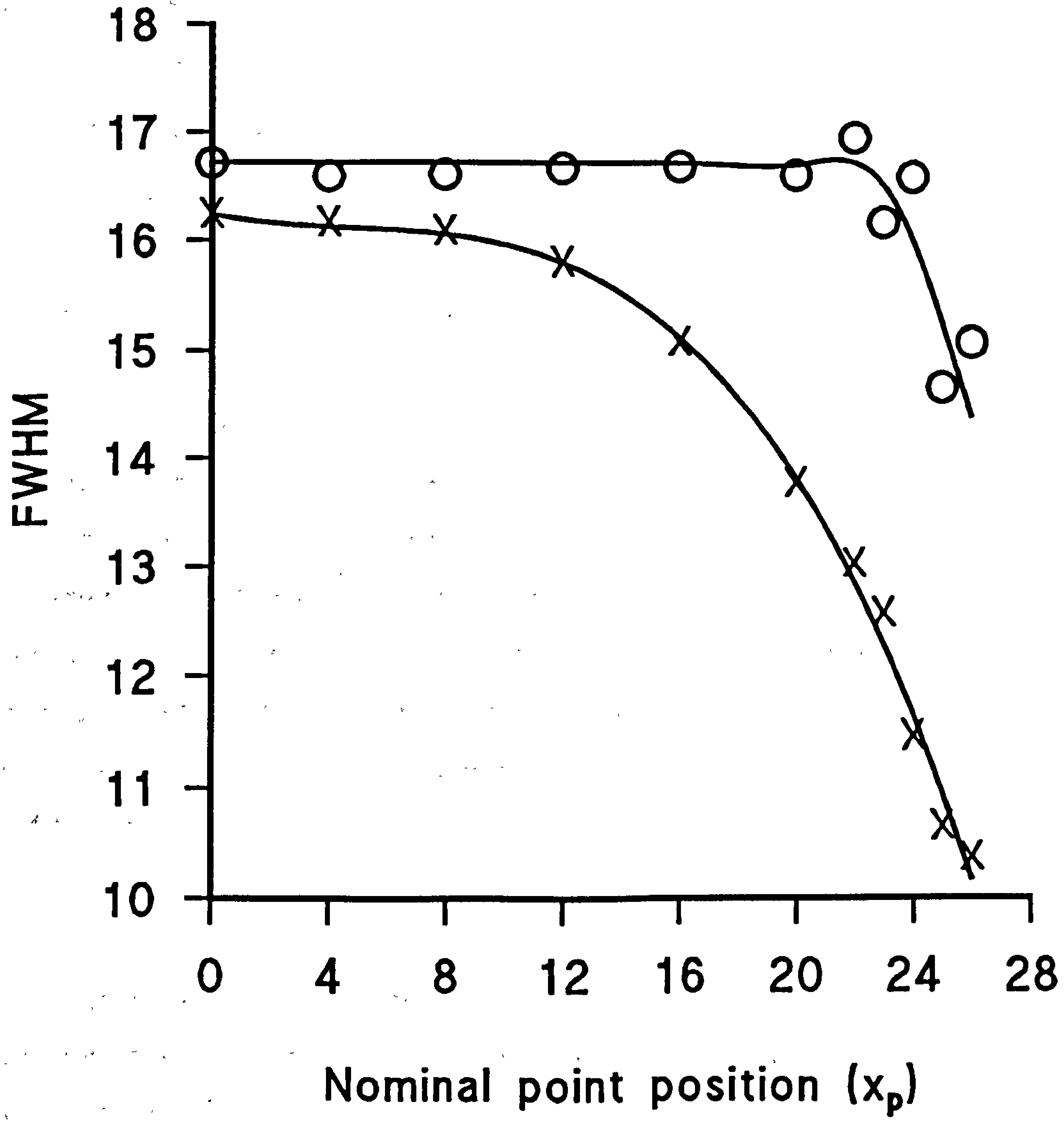

Figure 4.7

Width of PSF against nominal point position for original space (X) and equi-resolution space (O).

nominal x_p for the original and transformed images. The transformed FWHM measurements are virtually constant except for x_p positions close to the boundary.

4.5 Analysis of the point spread function and the application of spatial frequency filters using 2-dimensional Fast Fourier Transforms

Having transformed the reconstructed PSFs to a space in which the resolution is effectively constant, the form and dimensions of the PSF in equi-resolution space can now be measured. Since the transformed images are still contaminated with the negative overshoots produced as a result of the assumption of a fixed current density distribution (section 4.3) it is necessary to make these measurements at positions where this contamination is of relatively small amplitude, i.e close to the centre of the image. The PSFs for x_p = 0, 4, 8, 12 and 16 were measured assuming them to be circularly symmetrical. Figure 4.8 shows a section through the PSF at x_p = 0 plotted as data points (pixel values circularly averaged at each radial distance) against radial distance from the centre of the point object in equi-resolution space pixels. The line through the points is a curve fit of the simple Gaussian,

$$P = a\, e^{-bx^2} \tag{4.17}$$

with the amplitude parameter, a, set to the maximum pixel value and the width parameter, b, calculated using a commercial graph drawing package (Fig.P, Fig.P Software Corporation, Durham, North Carolina). The measurement and curve fitting process was repeated for the PSFs at x_p = 4, 8, 12 and 16 to give the results of table 4.4. It is clear from figure 4.8 and table 4.4 that the measured form of the PSFs corresponds very closely with the fitted Gaussian and that the measured width factors, b, are virtually constant throughout the central portion of the image. This finding of a near-Gaussian form for the PSF in equi-resolution space is very important as it makes possible the application of conventional spatial frequency filtering techniques.

The Modulation Transfer Function (MTF) of a linear system is the Fourier transform of its PSF. In the case of a Gaussian PSF, the Fourier transform and hence MTF is also Gaussian and the system suffers from loss of information at high spatial frequencies. To recover this information it is necessary to filter the image

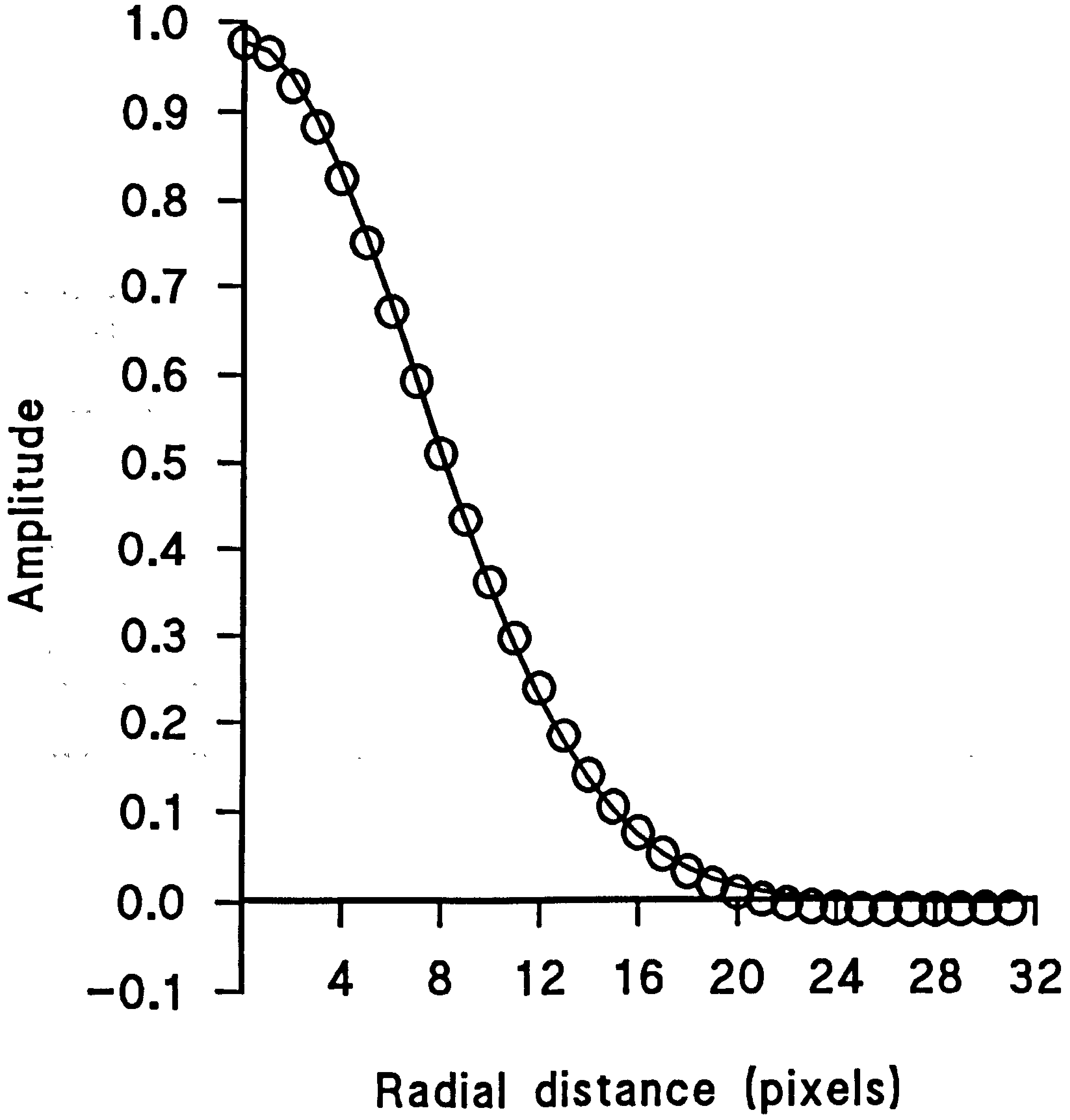

Figure 4.8

Section through PSF at $x_p = 0$
in equi-resolution space.
Line is nearest Gaussian fit.

Nominal PSF position	Amplitude parameter a	Width parameter b
0,0	0.9775	0.01004
4,0	0.9733	0.01013
8,0	0.9379	0.01011
12,0	0.8874	0.01012
16,0	0.8656	0.01033

$$P = ae^{-bx^2}$$

Table 4.4

Gaussian curve fit parameters for measured point spread functions at x_p = 0, 4, 8, 12 and 16.

so that the high frequency information is enhanced and a uniform frequency response recovered. Clearly, for any real system, there will be a cut-off frequency beyond which the amplitude of spatial frequencies in the image is genuinely zero. Enhancing spatial frequencies at or beyond this frequency limit will result in unacceptable noise amplification because it is at such high spatial frequencies that the image becomes dominated by noise. In general, the image restoration problem can be said to be ill-conditioned, in that the filtering operation required may be such that random perturbations in the original image (noise) will lead to artifactual perturbations in the filtered image which will swamp the true signal. The problem of how best to specify filters to deliver the maximum information in the presence of noise forms a large part of image processing theory (e.g Barrett and Swindell, 1981) and general signal processing theory.

A filtering strategy suitable for the EIT case is that of the Wiener filter. This filtering operation is optimised to minimise the mean-square value of an error signal defined as the difference between the filtered noisy image and the desired "perfect" image. The filter takes the form of

$$W(f) = \frac{H^*(f)}{|H(f)|^2 + \tau} \tag{4.18}$$

where W(f) is the filter in frequency space, $H^*(f)$ is the complex conjugate of the Fourier transform of the PSF, $|H(f)|^2$ is its modulus, and τ is a freely adjustable noise level parameter which controls the high frequency roll-off of the filter. A full derivation of the Wiener filter in an image processing context is given by Webb (1988).

The frequency filtering operation was implemented in frequency space using a 2-dimensional Fast Fourier Transform (FFT) algorithm (Cooley and Tukey, 1965). The FFT of a Gaussian PSF was first calculated using the mean width parameter from table 4.4 and stored. The Wiener filter was then evaluated using this data and a suitable value for τ, and the result stored. All subsequent image filtering operations were then carried out by calculating the FFT of the equi-resolution space image, multiplying by the stored filter in frequency space, and then transforming the result back to equi-resolution space using the inverse FFT. The 2-dimensional FFT program is implemented as a superposition of a number of 1-dimensional FFTs and is thus defined for a square image. To avoid the production of artifacts due to discontinuities in the data which would then be enhanced by the filtering process, it was necessary to interpolate smoothly from the boundary of the equi-resolution image to the boundaries of the 128 x 128 FFT input array, and to interpolate between opposite edges of this array. This was carried out using the FDM. Following the complete filtering operation the filtered image array was transformed from equi-resolution space back to the original image space using the inverse of the transformation described in section 4.4.

The major advantage of the Wiener filtering approach is the flexibility gained by free selection of the noise parameter, τ. Table 4.5 shows the FWHM of the PSF at $x_p = 0$ produced for various values of τ. Figure 4.9 a-h shows the corresponding images. In theory, for a perfect, noiseless Gaussian PSF sampled at single pixel intervals, the Wiener filter with τ approaching zero should be capable of reducing the PSF width to a single pixel. This would, however, imply a limiting spatial resolution much higher than that allowed by the amount of independent data from which the image was reconstructed. In the case of the simulation, where the only random noise is due to the calculation accuracy, this situation is not approached due to the presence of structure noise. This structure noise, in the form of the negative overshoots in the simulated PSFs, gives rise to the enhanced overshoots seen for small values of τ in figure 4.9. As explained in section 4.3, the origin of these overshoots lies in the assumption of unchanging current flow in the perturbed resistivity distribution. For small changes in resistivity and real noisy data it would be expected that the resolution limit for the filtering process would be set by the random noise in the image rather than the structure noise.

4.6 Transformation of the image space as a correction for spatial distortion

In section 4.1 it was noted that the image space produced as a result of the application of the weighted backprojection algorithm of equation 4.2 was distorted with respect to the original resistivity change distribution. The distortion of the image plane takes the form of drawing objects near the centre of the image further in towards the centre whilst leaving the positions of objects close to the boundary unchanged. The amount of distortion, defined as r'/r, where r is the nominal distance from the centre of the image and r' the reconstructed distance, was plotted against r' in figure 4.10 using data from table 4.1 plus additional measurements at $x_p = 22, 23, 25$ and 26. Figure 4.10 shows a good correlation

τ	Maximum pixel value	Minimum pixel value	FWHM
No filter	0.9887	-0.0131	16.22
10^{-1}	0.8128	-0.0640	14.85
10^{-2}	1.2044	-0.1067	12.47
10^{-3}	1.5725	-0.1424	10.78
10^{-4}	1.9508	-0.1785	9.51
10^{-5}	2.3960	-0.2234	8.52
10^{-6}	3.0968	-0.3011	7.44
10^{-7}	4.5739	-0.7856	6.37
10^{-8}	7.9641	-2.8755	5.64
10^{-9}	17.0868	-10.6144	5.13

Table 4.5

Widths of the point spread function at $x_p = 0$, $y_p = 0$ following Wiener filtering over a range of noise level parameter, τ.

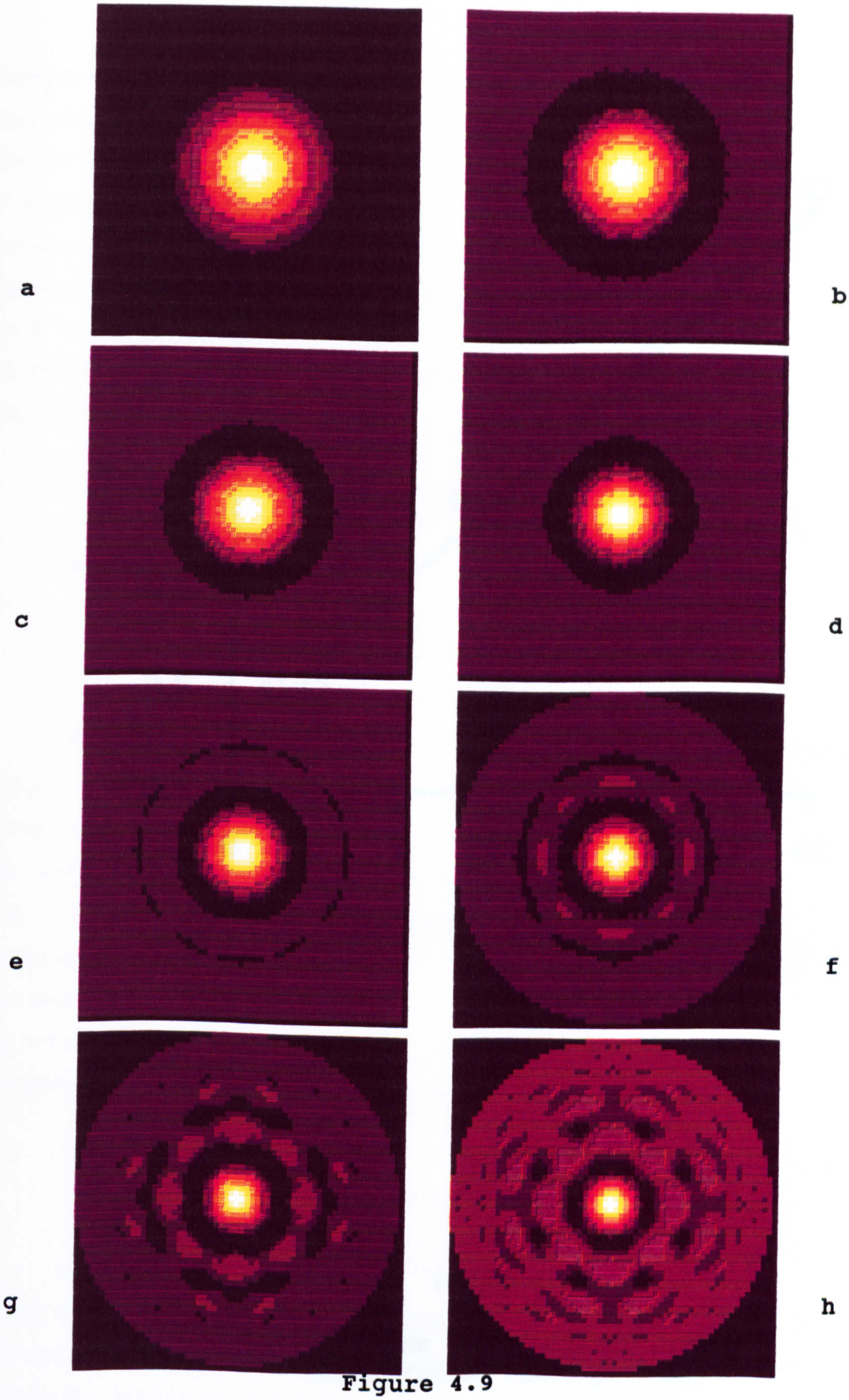

Figure 4.9

Images of a centrally placed point test object (a) with no filter and (b-h) Wiener filtered with noise level parameter, τ, 10^{-1} - 10^{-7} (see table 4.5).

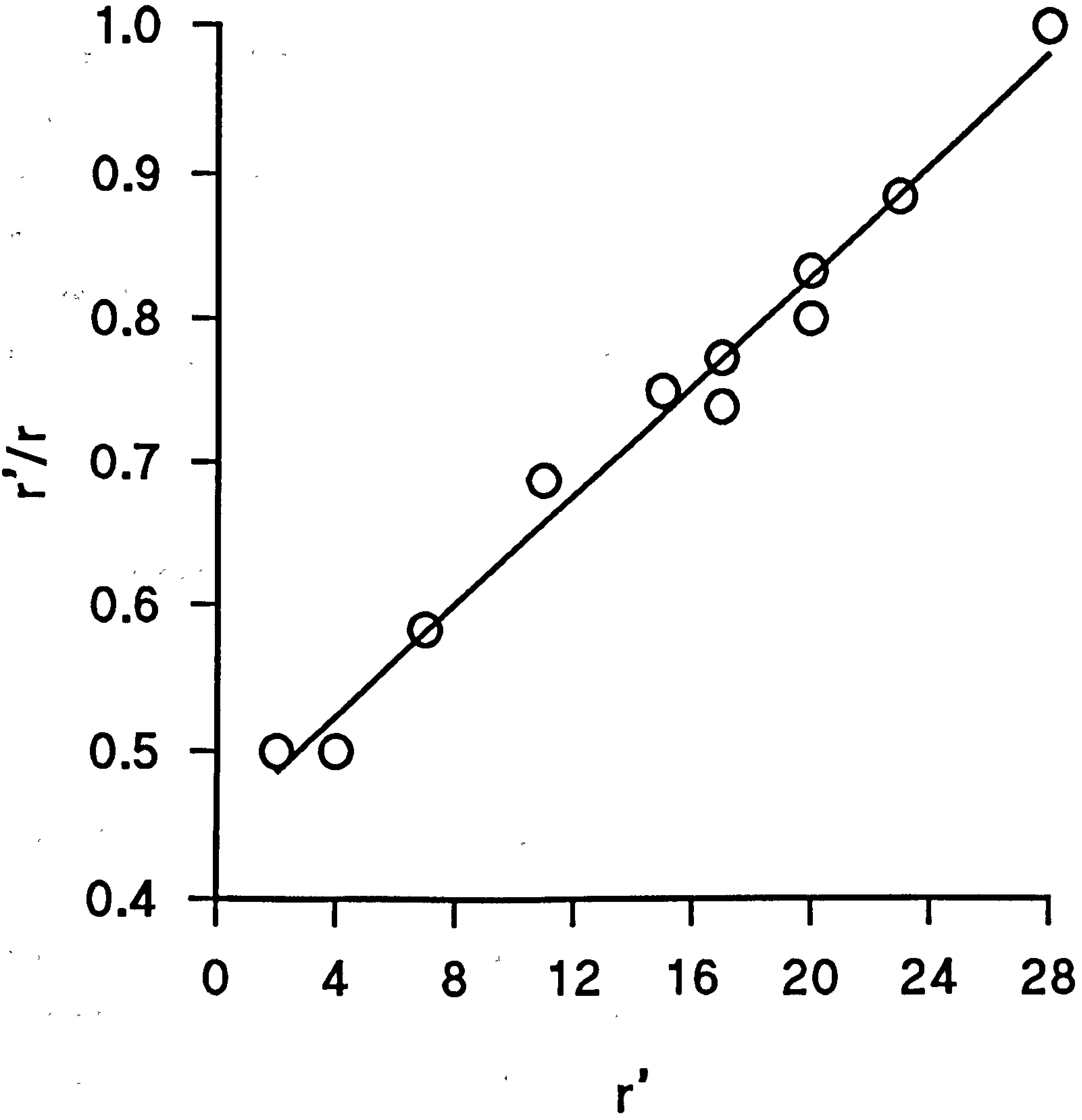

Figure 4.10

Position scale factor plotted against reconstructed radial position.

between r'/r and reconstructed position but, as in the case for the equi-resolution space transformation, the transformation to what will be termed true-position space should be independent of artificial boundary conditions. This invalidates the use of r' as an input parameter for the transformation process. Following the same line of reasoning as for the equi-resolution space transformation (section 4.4) it would seem appropriate to again base the correction on the normalised total sensitivity at each point, S_{norm}. To achieve this while at the same time retaining the useful straight line relation of figure 4.10, the relation between S_{total} and c, the normalised radial position, (equation 4.11) can be rewritten for S_{norm} (since $S_{total} \propto S_{norm}$) as

$$S_{norm} \propto \frac{1}{(1 - c^2)^2} \qquad (4.19)$$

and rearranged to give

$$c \propto \sqrt{1 - \frac{1}{\sqrt{S_{norm}}}} \qquad (4.20)$$

This relation is based on an analysis for a 2-dimensional circular region (Seagar et al, 1987) so would be expected to be only approximately true for the 3-dimensional case. Figure 4.11, however, shows a useful straight-line relation between r'/r and this function of S_{norm} for values of x_p up to $x_p = 25$. As with figure 4.3, the results for $x_p > 25$ are suspect because of the inaccuracies in S_{norm} expected close to the boundary. The quantity r'/r at each point is the reciprocal of the local scale factor required to make the transformation to true-position space, F_{tp}, which can be calculated from the array of S_{norm} values using the regression equation derived from figure 4.11 and the relationship

$$r_{tp} = i \sum_{r=0,i,2i..}^{r_{or}} F_{tp}(r) \qquad (4.21)$$

where i is again the incremental distance in the original space and r is the radius at the current increment. Although a fundamental relationship between positional inaccuracy and S_{norm} seems less likely than the theoretically supported relationship between resolution and S_{norm}, the proportionality evident in figure 4.11 is adequate to make a correction for geometrical distortion provided that the boundary geometry is not too far removed from that of cylinder, a condition which

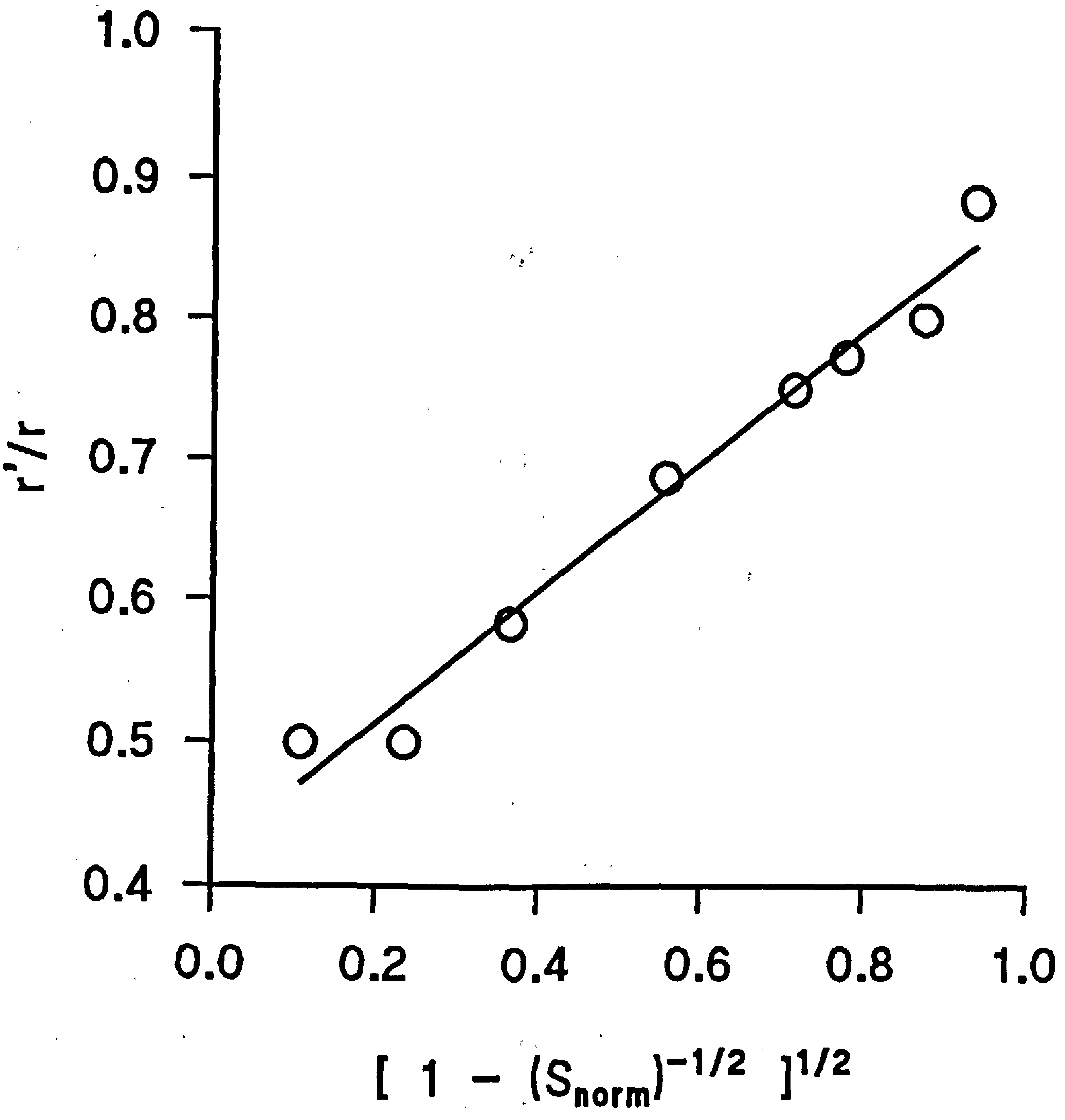

Figure 4.11

Position scale factor plotted against a function of S_{norm}.

will be met by most body cross-sections. The transformation to true-position space was implemented in a similar manner to the equi-resolution space transformation described in section 4.4.

Figure 4.12 a-h shows the images of figure 4.1 filtered with $r = 10^{-5}$ and transformed to true-position space. The image statistics are given in table 4.6.

4.7 Measurements of the axial extent of the point spread function

To investigate the effect of out-of-plane perturbations on the image reconstructed for a single plane data set, a test object consisting of a single volume element of raised resistivity was used. Images were reconstructed from one set of voltages measurements using the algorithm of equation 4.2. The plane of the electrodes was coincident with the plane of the image. Corrections for in-plane PSF and position were not applied.

The test object was positioned at $x_p = 0, 8, 16, 20,$ and 24 ($y_p = 0$) for distances from the image plane, z, of 0 to 40 in steps of 4. The reconstructed amplitude of the object is plotted against distance from the image (and electrode) plane in figure 4.13 for each of the x_p positions. A Gaussian is fitted to each set of data points. It can be seen from the figure that the axial extent of the imaged volume close to the electrodes is much smaller than that close to the centre of the image. This confirms the general shape of the imaged volume for a cylinder given by Brown et al (1985). The shapes of the axial PSFs seem to be a reasonable fit to a set of Gaussian curves. Overshoot errors due to the assumption of a fixed current flow distribution would be expected to make the data points taken close to the electrodes less accurate.

Following the approach used successfully to relate the in-plane resolution to S_{norm}, the axial resolution was similarly treated. The FWHMs of the axial direction PSFs were measured for each x_p position and the reciprocal, taken as a measure of axial resolution, calculated. This is plotted as a function of the square root of S_{norm} (at the reconstructed x_p positions) in figure 4.14. The figure demonstrates a similar proportionality between axial resolution and S_{norm} as was found for the in-plane resolution in figure 4.4. The constants of proportionality are, however, different in the axial and in-plane cases.

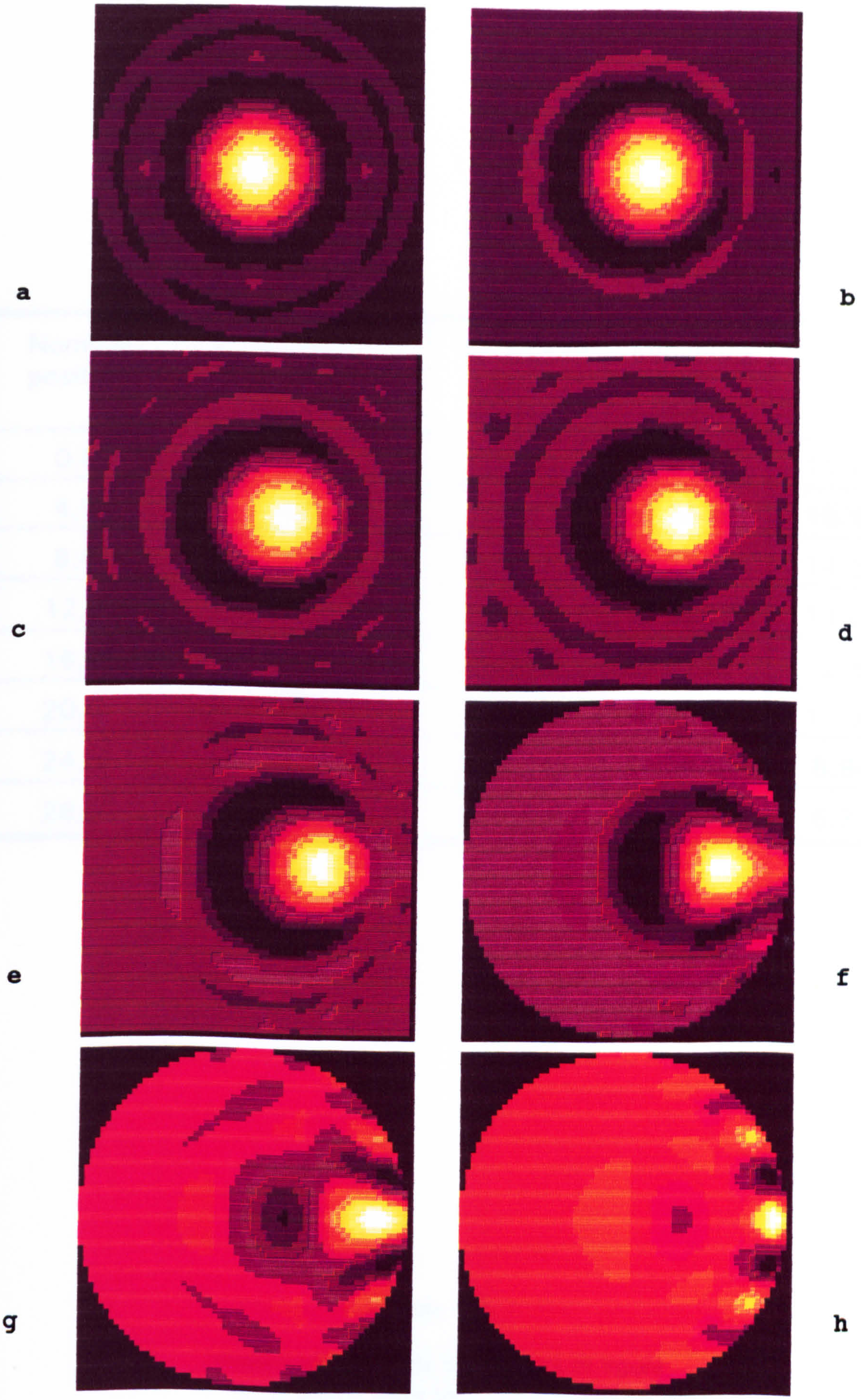

Figure 4.12

The images of figure 4.1 filtered with $\tau = 10^{-5}$ and transformed to true position space using the transformation of equation 4.21.

Nominal position	Reconstructed position	Maximum pixel value	Minimum pixel value	FWHM of PSF
0,0	0,0	2.3960	-0.2142	15.90
4,0	4,0	2.3463	-0.2535	15.51
8,0	7,0	2.2498	-0.2815	14.89
12,0	10,0	2.1025	-0.3207	14.05
16,0	14,0	2.0335	-0.3782	12.86
20,0	18,0	2.0669	-0.6087	11.79
24,0	26,0	3.0631	-1.5442	8.96
28,0	29,0	9.9258	-7.0874	6.37

Table 4.6

Image statistics for the images of figure 4.13 which were reconstructed using the algorithm of equation 4.2 together with Wiener fltering ($\tau = 10^{-5}$) and position correction.

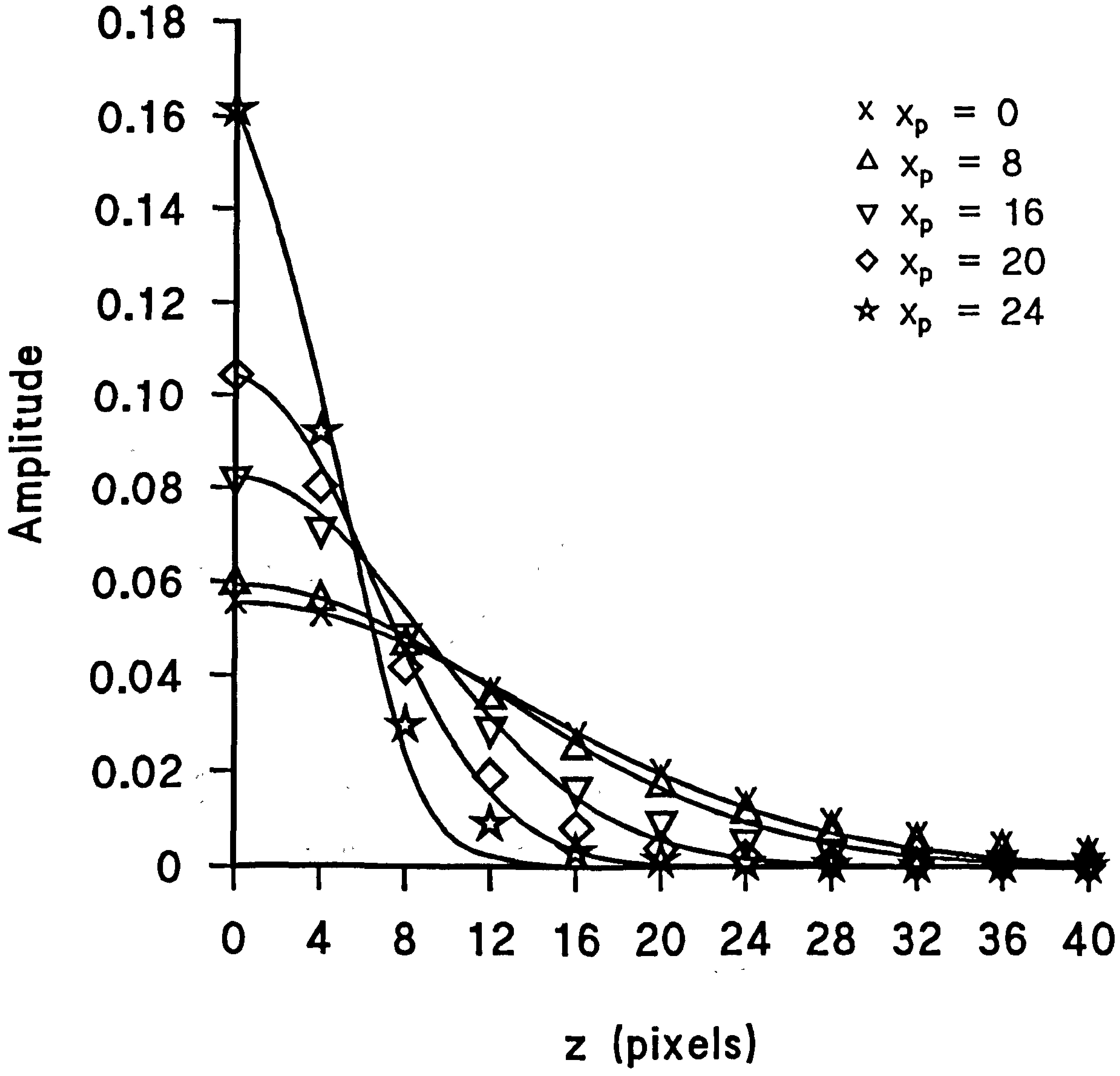

Figure 4.13

Reconstructed amplitude against distance of object from electrode plane. Lines are nearest Gaussian fits.

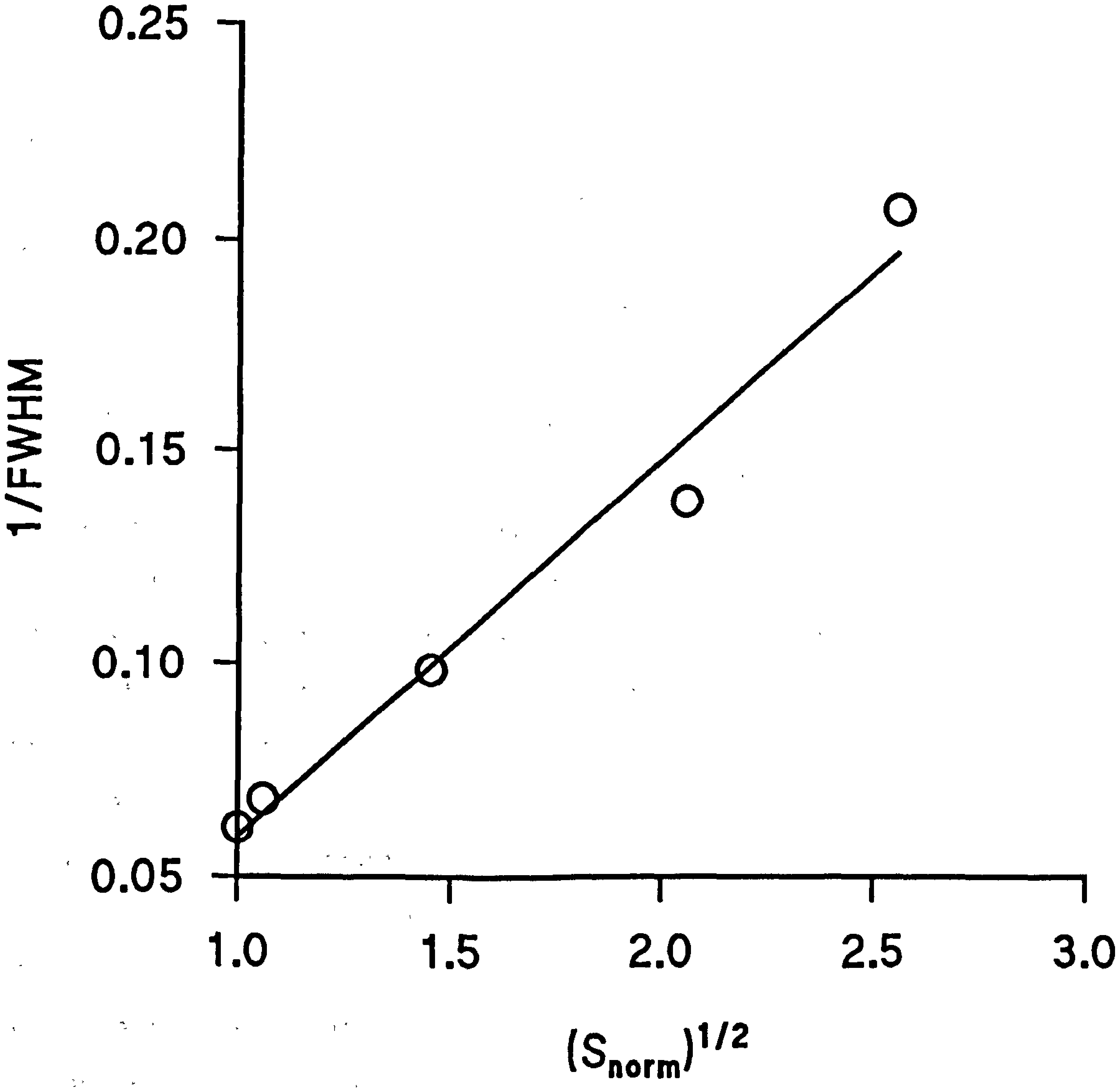

Figure 4.14

Axial direction resolution plotted against the square root of the normalised total sensitivty, S_{norm}.

4.8 Summary of chapter 4

Voltage measurement sets for extended point test objects generated by a 3-dimensional software simulation of electrical impedance tomography have been used to develop and test a sensitivity coefficient weighted backprojection algorithm. The variation in width of the point spread function (PSF) in the image plane for this algorithm has been investigated and a transformation to an image space in which the PSF is essentially stationary formulated and implemented. In this transformed space, the form of the PSF has been revealed to approach that of a Gaussian. It is suggested that degradations to this Gaussian form observed for positions close to the measurement electrodes are a result of the assumption of an unchanging current flow distribution for the perturbed and unperturbed resistivity distributions, an effect which decreases in severity as the amplitude of the resistivity perturbation is reduced. The application of an appropriate spatial frequency filter in the transformed space has been shown to reduce the width of the PSF and hence increase resolution up to a limit set, in the case of the simulation, by the degradation of the Gaussian PSF, but expected to be set by the signal-to-noise ratio of non-simulated data. A further correction for geometrical distortion of the image has been implemented although it is suspected that this correction could be less appropriate for non-cylindrical boundary conditions. Finally, the axial extent of the imaged volume has been investigated using a single volume element as the test object and the size and form of the PSF in the axial direction derived. The axial PSF has been shown also to approach a Gaussian form. This finding opens the possibility for further spatial frequency filtering in the axial direction to produce true tomographic planes from sets of overlapping volume images. The normalised total sensitivity at each point of the reconstructed image has been shown to control the reconstructed amplitude of the basic weighted backprojection, the resolution in both the image plane and in the axial direction, and to some extent the degree of geometrical distortion in the image.

Figure 4.15 shows the complete reconstruction algorithm.

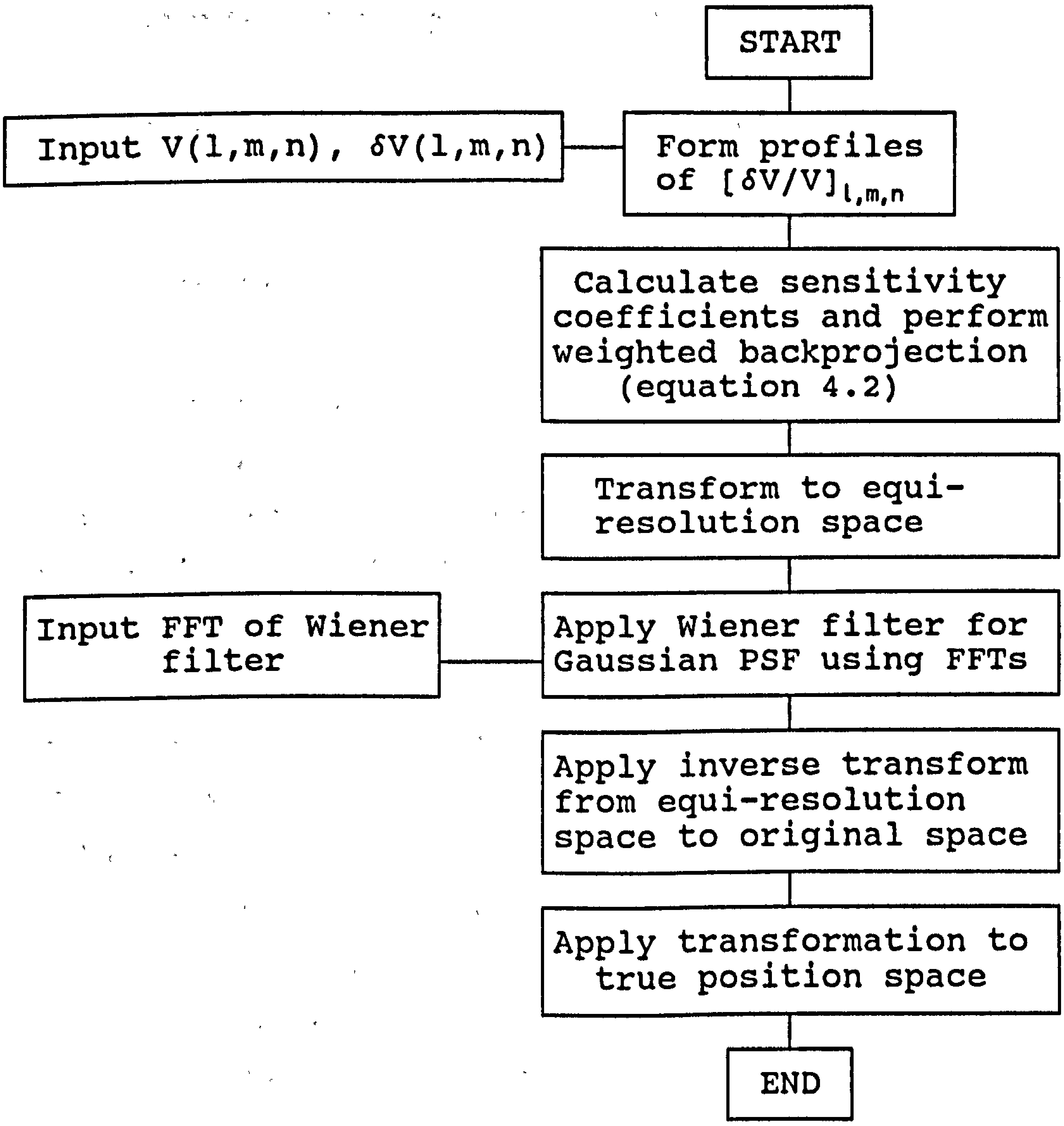

Figure 4.15

Electrical impedance tomography reconstruction algorithm for cylindrical boundary conditions.

CHAPTER 5

RECONSTRUCTIONS OF PHYSICAL PHANTOM AND IN-VIVO TEST DATA.

5.0 Introduction

In chapter 1 (section 1.2) the four-electrode method of measurement of voltage gradient data sets suitable for the reconstruction of electrical impedance tomograms was described. Real data sets differ from the idealised data sets simulated in the previous chapter not only because of their inevitable noise content, but also because of the effects of electrode impedances. To overcome these effects it is necessary to image change in impedance rather than absolute value, use a constant current signal source, and use high impedance voltage gradient measurement circuits. The voltage drop across the impedance of the current drive electrodes also renders useless the three voltage gradient measurements which include one or both of these electrodes. To make the image reconstruction algorithm developed in the previous chapter suitable for use with physical test tank data and data obtained from a human subject, it was first necessary to carry out some further simulations to establish the validity of its use with this reduced data set, to consider other current drive configurations, and to extend the use of algorithm to non-cylindrical boundary conditions.

5.1 Simulated reconstructions using 13 sample voltage profiles

The weighted back-projection algorithm of equation 4.2 was applied to an extended point test object at various distances, x_p, from the centre of the image using the simulation described in chapter 3. To clarify the effects of the use of the reduced data set, no corrections for PSF or geometrical distortion were applied initially.

The first attempt to reconstruct an image using only 13 values of $(\delta V/V)_{l,m,n}$ for each of the 16 current drive orientations was carried out by changing one of the program loop counters so that each pixel value

$$P(x,y,z) = \frac{\sum_{l}\sum_{m}\sum_{n} s_{l,m,n,x,y,z}\left(\frac{\delta V}{V}\right)_{l,m,n}}{\sum_{l}\sum_{m}\sum_{n} s_{l,m,n,x,y,z}} \tag{5.1}$$

was evaluated for n = 2 to 14 instead of from 0 to 15. This approach did not produce a recognisable image. A closer examination of the reconstruction process revealed that the array containing the denominator of equation 5.1 (S_{total}) now contained some very large and very small values which had not been present in the previous 16 sample simulations. Since S_{total} in its normalised form S_{norm} has been shown to be of fundamental importance to the operation of the complete reconstruction algorithm it is clearly vital that this parameter be evaluated correctly regardless of the number of samples in the data set. It was therefore decided to return the program to an n loop count of n = 0 to 15, but to set the values of $(\delta V/V)_{l,m,n}$ to zero for n = 0, 1 and 15. This is equivalent to the assumption that no voltage gradient change takes place adjacent to the current drive electrodes. This modification produced the images shown in figure 5.1 a-h. The image statistics are given in table 5.1.

Comparing figures 5.1 and 4.1, and tables 5.1 and 4.1, it can be seen that the images and statistics are very similar, the only significant difference being a slight increase in the degree of negative overshoot towards the periphery of the image. A qualitative explanation for the similarity is that for the cases where the voltage sense electrodes are very close to, or coincident with, the current drive electrodes, the sensitivity coefficient values close to the electrodes will be evaluated (equation 2.18) as the dot product of two particularly large field gradients and will fall off rapidly as the distance from the electrodes increases. The influence of the data samples adjacent to the current drive electrodes will thus tend to be concentrated close to the periphery of an image formed using the weighted backprojection of equation 5.1.

The close similarity between the images of figures 5.1 and 4.1 is highly convenient in that the geometrical transformation and PSF filtering steps previously derived using 16 sample voltage profiles can be applied to the 13 sample images without modification.

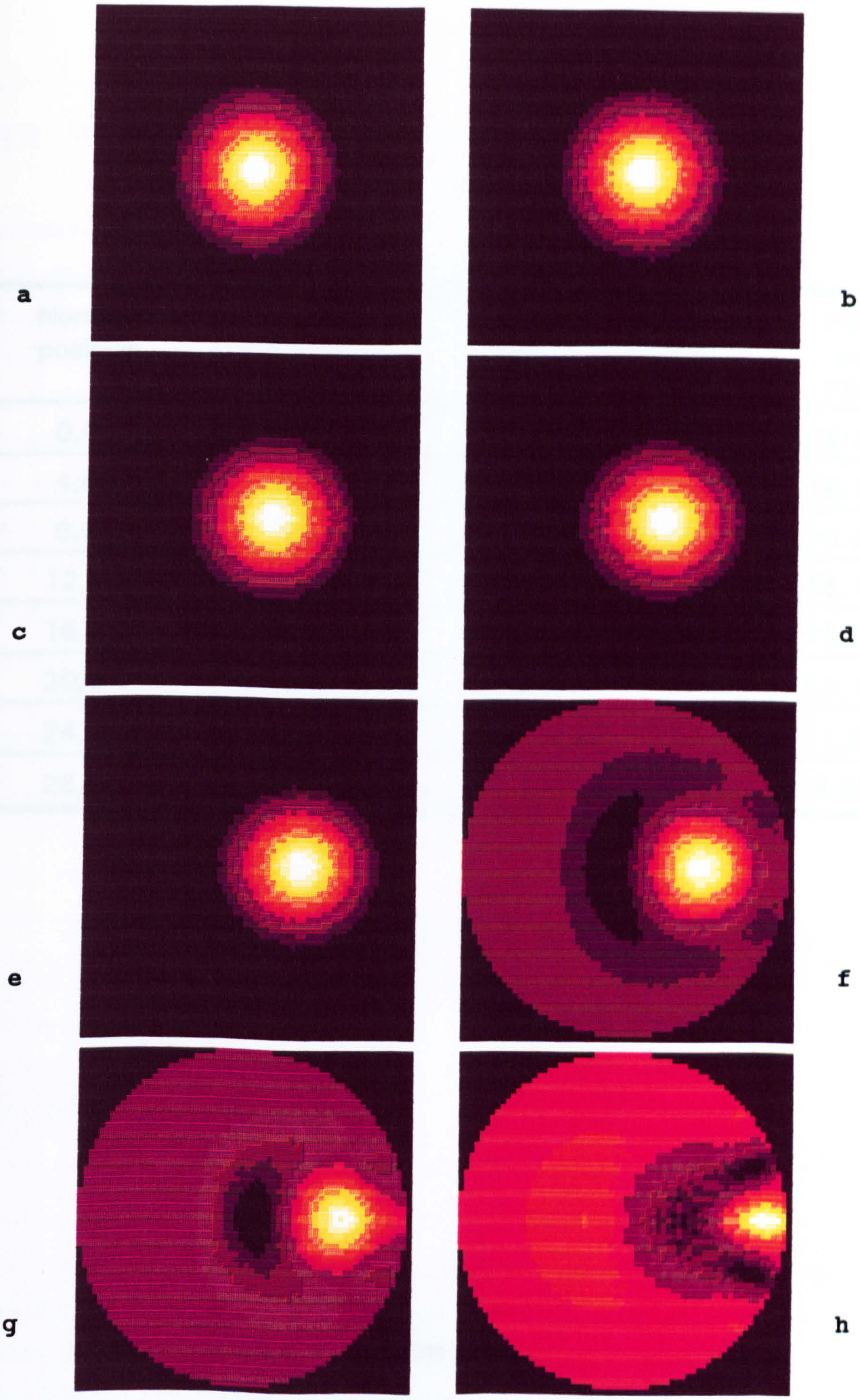

Figure 5.1
Simulated point test object at (a-h) 0, 4, 8, 12, 16, 20, 24 and 28 pixels from the axis of a 63 pixel diameter cylindrical boundary. Reconstructed using equation 5.1 with 13 samples of $(\delta V/V)$ for each current drive orientation.

Nominal position	Reconstructed position	Maximum pixel value	Minimum pixel value	FWHM of PSF
0,0	0,0	0.9886	-0.0132	16.22
4,0	2,0	0.9732	-0.0136	16.15
8,0	4,0	0.9380	-0.0153	16.06
12,0	7,0	0.8878	-0.0191	15.78
16,0	11,0	0.8648	-0.0336	15.07
20,0	15,0	0.8238	-0.1345	13.74
24,0	20,0	0.9751	-0.3599	11.38
28,0	29,0	1.3383	-0.7370	8.53

Table 5.1

Image statistics for the images of figure 5.1 which were reconstructed using the algorithm of equation 4.2 for 13 samples of $[\delta V/V]_{l,m,n}$ per current drive orientation.

5.2 Approximate potential field model

The simulations carried out in chapter 4 were all based on a cylindrical geometry with adjacent electrode current drive, and used a stored set of potential field data as the basis for the reconstruction calculation. For a reconstruction algorithm intended for use with generalised body cross-sections, a more flexible source of potential field data is required. In principle, sets of potential field data could be generated for each boundary shape encountered using the FEM or FDM, a process which would need to be repeated for each current drive configuration. In practice, without powerful computing facilities, this process would be inconveniently time consuming, especially if multi-plane data sets are being considered. A more practical alternative is to use an approximate model for the generation of potential field data whilst recognising that this will be the source of some inaccuracy in the final result.

By analogy with electrostatics (e.g Ferrari, 1975), the potential, V, at a point, P, in an infinite homogeneous conductive medium of conductivity σ is given by

$$V = \frac{I}{4\pi\sigma}\left(\frac{1}{a} - \frac{1}{b}\right) \tag{5.2}$$

where a and b are the distances from the current (I) drive electrodes to the point P. Where the current drive electrodes lie in the plane boundary of a semi-infinite conductive medium, the resistance between the electrodes will be doubled resulting (for the constant current case) in a doubling of the drive voltage. The potential will then be given by

$$V = \frac{I}{2\pi\sigma}\left(\frac{1}{a} - \frac{1}{b}\right) \tag{5.3}$$

This relationship can be used to provide a first approximation to the potential field in a general body shape by treating each current drive orientation as the semi-infinite case with the boundary plane running through the plane of the current drive electrode pair. The image boundary is now represented as an N sided polygon (where N is the number of electrodes) with an electrode at each vertex. This semi-infinite approximation would be expected to be reasonably accurate close to the current drive electrodes, where the boundary is represented, but poor close to the other boundaries which are not represented in this model.

An assumption implicit in the use of equation 5.3 is that of point electrode contact, which is somewhat unrealistic in practice. The assumption that the electrodes are small with respect to the object being imaged is, however, advantageous when considering the voltage developed across the current drive electrode pair. If the electrode contact is modelled as a hemispherical conductor buried in a semi-infinite conductor of conductivity, σ, then the contact resistance, R, is given by,

$$R = \frac{1}{2\pi d\sigma} \tag{5.4}$$

where d is the radius of the hemispherical area of contact (e.g Ferrari, 1975). For a pair of such electrodes, the overall resistance will clearly be twice this value regardless of the distance between the electrodes (provided they are not touching). As the radius, d, is reduced, the contact resistance will increase to infinity for a true point electrode. Thus for small electrodes in contact with a general large volume conductor it is reasonable to assume that the impedance presented to the current drive electronics will be relatively insensitive to variations in electrode spacing. This has the advantage that in the computer simulations, where the constant current, I, is implied by fixed voltages at the Neumann (current drive electrode) portions of the boundary rather than included explicitly, equation 5.3 can be applied to a range of drive current electrode pair spacings using an assumed constant value for I.

A previous comparison (Kotre, 1988) between potential fields generated by the semi-infinite model with 3-dimensional FDM generated fields for cylindrical boundary conditions showed that the semi-infinite model produced a good approximation to the true potential field. The success of the semi-infinite approximation in the cylindrical case can be qualitatively explained by reference to figure 5.2 which shows an image of the potential field calculated using equation 5.3 on which a cylindrical boundary has been superimposed. Current flux lines (lines orthogonal to the equipotentials) calculated from the potential field are also shown. It can be seen that the amount of distortion of the current flux lines required to make them conform to the cylindrical boundary is small, making the semi-infinite approximation quite accurate for the cylindrical case. The figure shows the case of adjacent electrode current drive for 16 electrodes, an angle of 22.5°

Figure 5.2
Image of the potential field calculated using the semi-infinite model of equation 5.3 on which a cylindrical boundary has been superimposed. Current flux lines calculated from the potential field are shown.

between the current drive electrodes. Figure 5.3 shows a comparison between the boundary potentials calculated using the three-dimensional finite differences program and those produced using the semi-infinite model for a drive current angle of 22.5°. The figure covers the range of angular boundary position from 0° to 180° only, the potentials being symmetrical but of opposite sign for the rest of the boundary. The position of the current drive electrode is indicated by a dotted line. Previous comparisons with the FDM and experimental boundary potential measurements made for angles of 45°, 90° and 180° between the current drive electrodes demonstrated the same general agreement with the semi-infinite model. This result will be used in a comparison of alternative current drive configurations in section 5.3. The semi-infinite potential field approximation will also be used in section 5.5 in the reconstruction of a set of in-vivo data.

5.3 Simulated reconstructions using alternative current drive configurations

In all the reconstruction simulations carried out so far, it has been implicitly assumed that the optimum current drive configuration for a set of equally spaced electrodes is that of adjacent electrode current drive. For systems where a constant current is injected via two electrodes only for each set of voltage gradient measurements, Seagar et al (1987) show that the maximum structural information can be recovered from a circularly bounded 2-dimensional conductivity distribution when the angular frequency components of the applied current distribution increase linearly in amplitude with frequency. Such a distribution can be obtained by applying the current as a single current dipole (Barber and Seager, 1987). In practice the closest approximation to this configuration is the use of adjacent electrodes. In a review of data collection methods, Patel (1990) concludes, however, with reference to the work of Hua et al (1987), that the use of adjacent current drive electrodes is the poorest both in terms of spatial resolution and sensitivity, and that an improvement can be gained by the use of opposite electrodes for current drive. A similar conclusion is drawn from the analysis of Cheney and Isaacson (1992). Since the main disadvantage of EIT as an imaging modality is its low spatial resolution, which is governed by the interaction between the applied current distribution and the unknown resistivity distribution, rather than overall signal-to-noise performance, which can in principle be improved by data

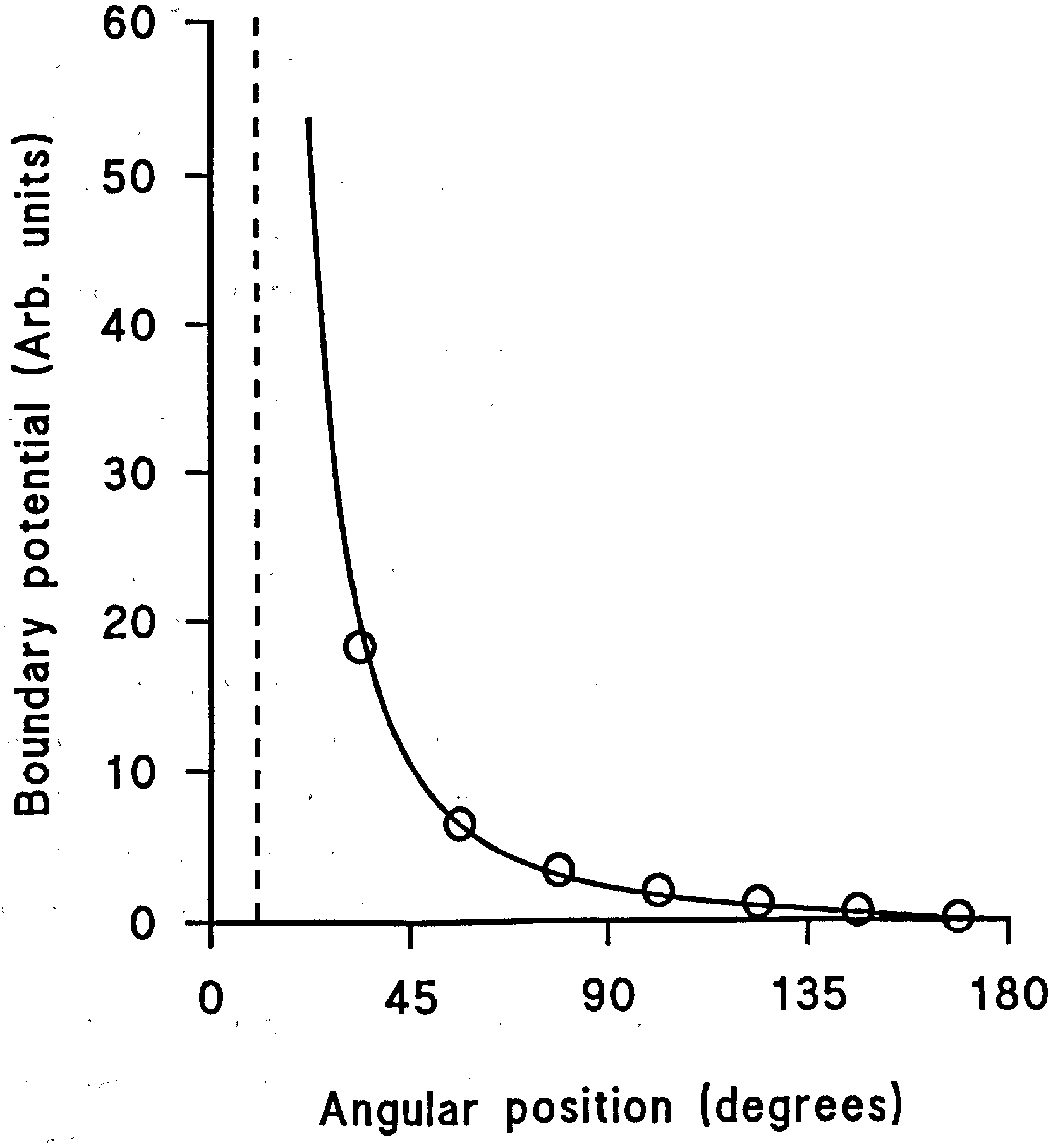

Figure 5.3

Comparison of boundary potential calculated using semi-infinite model with measured values (O) for cylinder of uniform conductivity. Dotted line marks current drive electrode position.

averaging, such a claim is worthy of experimental investigation.

Using the 3-dimensional simulation of chapter 3 in conjunction with the semi-infinite model (section 5.2) for the generation of approximations to the appropriate cylindrically bounded potential fields, reconstructions of extended point test objects were carried out for a number of current drive configurations. These corresponded to drive electrode angular spacings of 22.5°, 45°, 67.5°, 90°, 112.5°, 135°, 157.5° and 180°. The voltage sense electrode spacing was 22.5° in all cases. Reconstructions were carried out for two object positions; $x_p = 0$, $y_p = 0$ and $x_p = 20$, $y_p = 0$. Since only a relative comparison of resolution was required, the PSF and position correction steps in the algorithm of figure 4.15 were not applied and a summation over the equivalent of 9 planes of volume elements only was used to save time. Because the variation in drive current electrode angular spacing is so large in this case, it is not appropriate to apply the assumption of a semi-infinite medium, and some variation in the impedance between the drive current electrodes with angular spacing would be expected. As the spacing is constant for each reconstruction, however, any variation of this impedance (and hence the amplitude of the resulting potential field) will appear merely as a constant scaling factor on the sensitivity coefficients (equation 2.18) and will not affect the resolution.

The results are given as graphs of resolution (defined as 1/FWHM) against drive electrode angular spacing for the object at $x_p = 0$ in figure 5.4 and $x_p = 20$ in figure 5.5. Figure 5.4 shows a clear reduction in spatial resolution at the centre of the image as the drive electrode angular spacing is increased. No clear trend is apparent towards the periphery of the image (figure 5.5), with all the recorded spatial resolutions being quite similar. Some variation in the reconstructed positions of the test object was, however, seen.

If it is accepted that the spatial resolution towards the centre of the image is of the greatest importance, the results of figures 5.4 and 5.5 would seem to experimentally justify the choice of adjacent electrode current drive, at least for the noiseless case. This choice also allows data produced using the proven Sheffield acquisition system (Barber and Seagar, 1987) to be used with this algorithm. The flexibility of the algorithm with regard to current drive configuration has been demonstrated, although it should be noted that the appropriate measurements relating the spatial resolution and position correction to S_{norm} would need to be repeated if another drive current configuration was chosen.

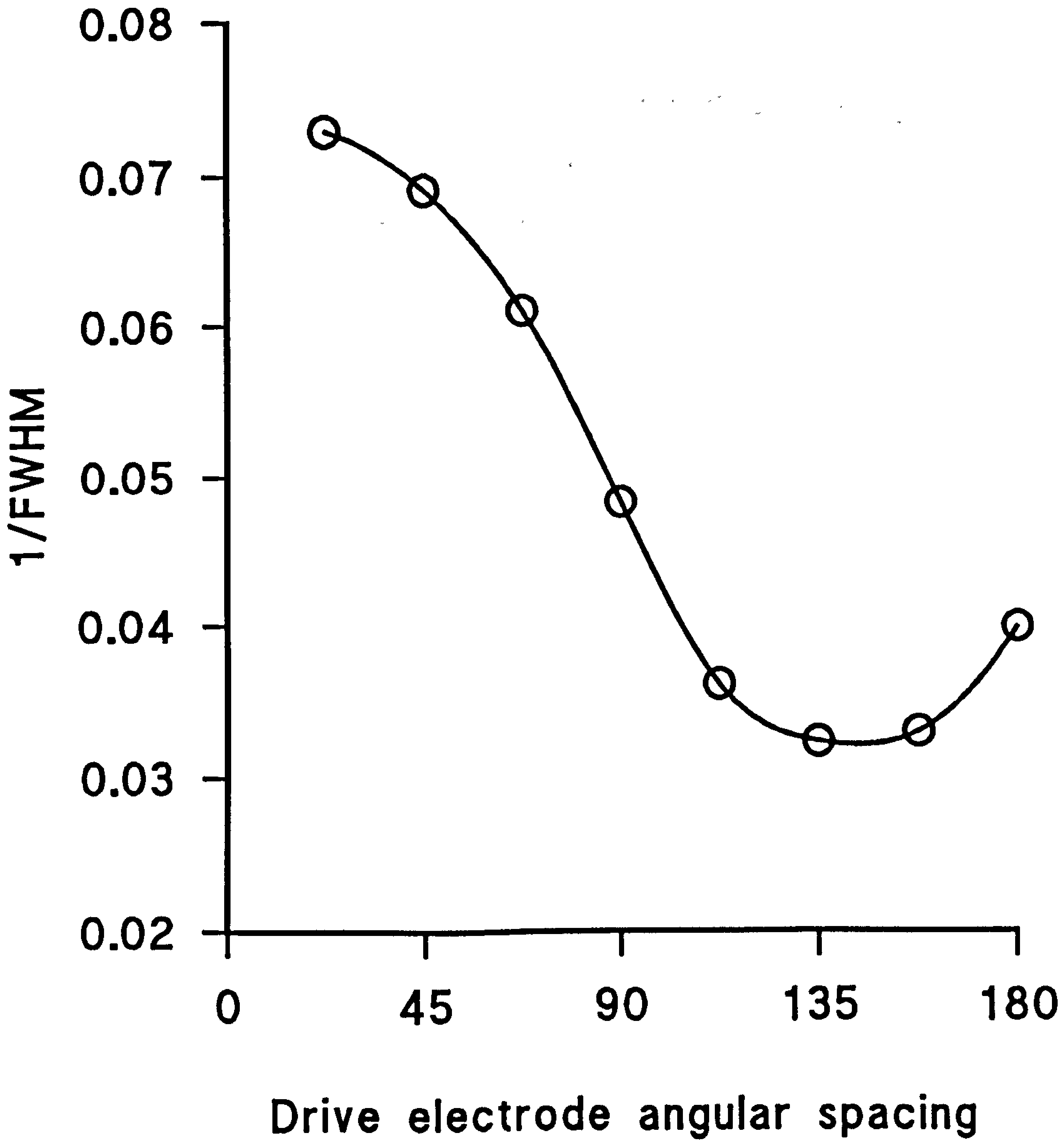

Figure 5.4

Change of resolution with current drive electrode angular spacing at centre of image.

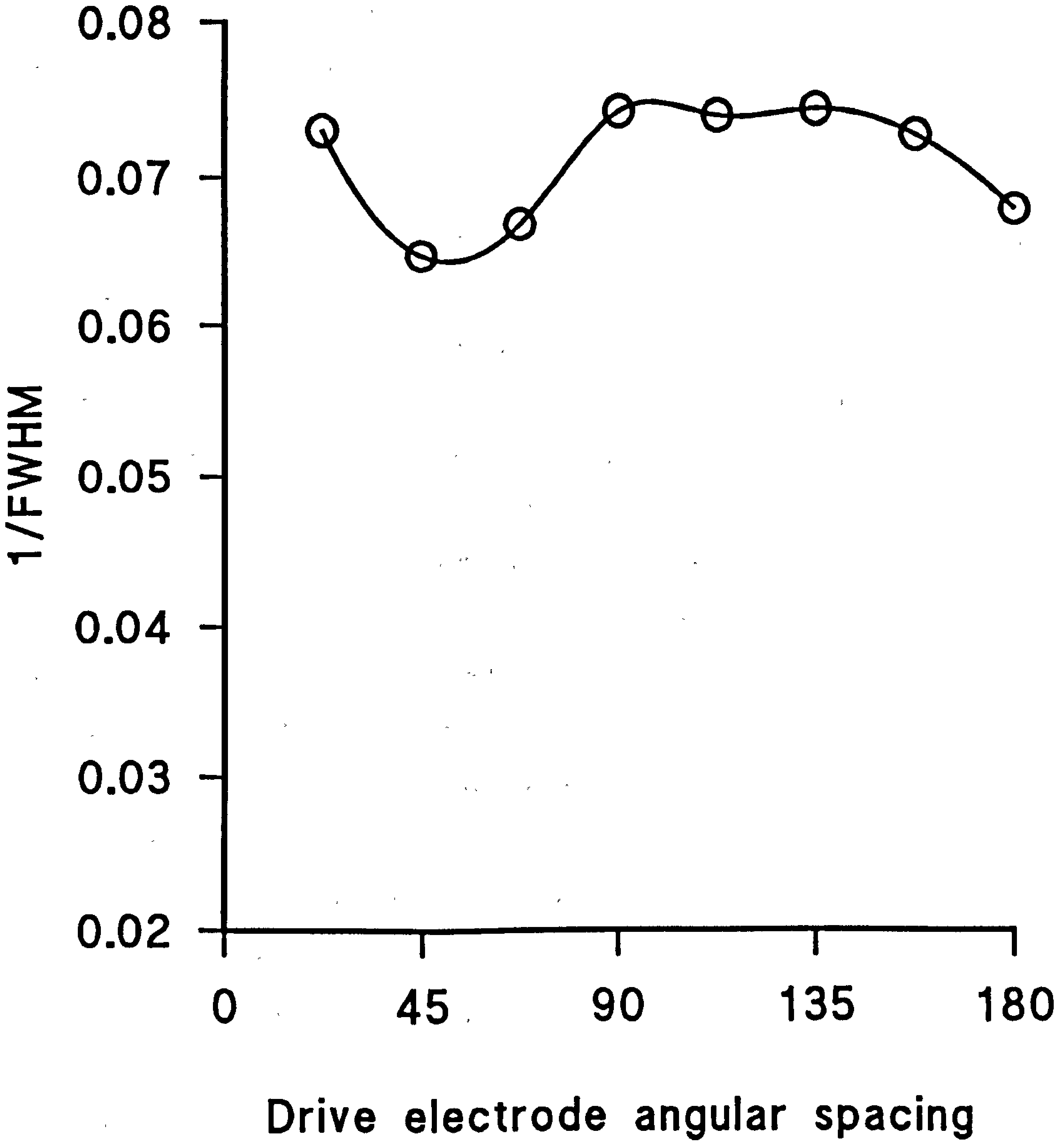

Figure 5.5

Change of resolution with current drive electrode angular spacing at periphery of image.

5.4 Reconstructions of physical phantom test data

To validate the reconstruction algorithm of figure 4.15 on real measured data sets, it was decided to use data sets which most closely matched the situation modelled in the simulations of chapter 4, i.e test objects in a cylindrical tank of saline with 16 electrodes spaced equally around the plane of the image. Appropriate sets of data were produced at the Department of Medical Physics and Clinical Engineering, Royal Hallamshire Hospital, Sheffield, UK (see Acknowledgements) using the data acquisition system developed in that department (Brown and Seagar, 1987). The test tank was 150 mm in diameter and the test object a 15 mm insulating rod placed at positions corresponding to the positions simulated in figure 4.1, i.e $y_p = 0$ with $x_p = 0, 4, 8, 12, 16, 20, 24$ and 28. The positional accuracy of the rod placement was estimated at 5% of the tank radius, corresponding to ± 1.6 pixels. A reference set of data with no test object present was also taken.

These data sets were reconstructed using the algorithm of figure 4.15 adapted for use with 13 samples of $(\delta V/V)_{l,m,n}$ for each current drive orientation as described in section 5.1. The same stored potential field data that was used in the earlier simulations was used to calculate the sensitivity coefficients. The measured reference data set was used in the evaluation of $(\delta V/V)_{l,m,n}$ in each case. Figure 5.6 a-h and table 5.2 show the results of the backprojection without PSF and position corrections which can be compared with the simulations of figure 5.1 and table 5.1. PSF and position corrections were applied with the noise level parameter, τ, set to 10^{-5}. The results are shown in figure 5.7 a-h with the image statistics given in table 5.3. When comparing these image statistics to any of those produced by the earlier simulations it should be noted that the pixel values now include various scale factors generated during the data collection and transfer processes, and that the test object is of a relatively large size, so the FWHM measurements will reflect the system PSF convolved with the real size of the object.

The results are very much in accordance with those predicted by the simulations. The degree of positive and negative overshoot at positions close to the electrodes is less severe than that produced in the simulations as predicted in section 4.3, but the positional accuracy does not appear to be quite as good towards the periphery of the image.

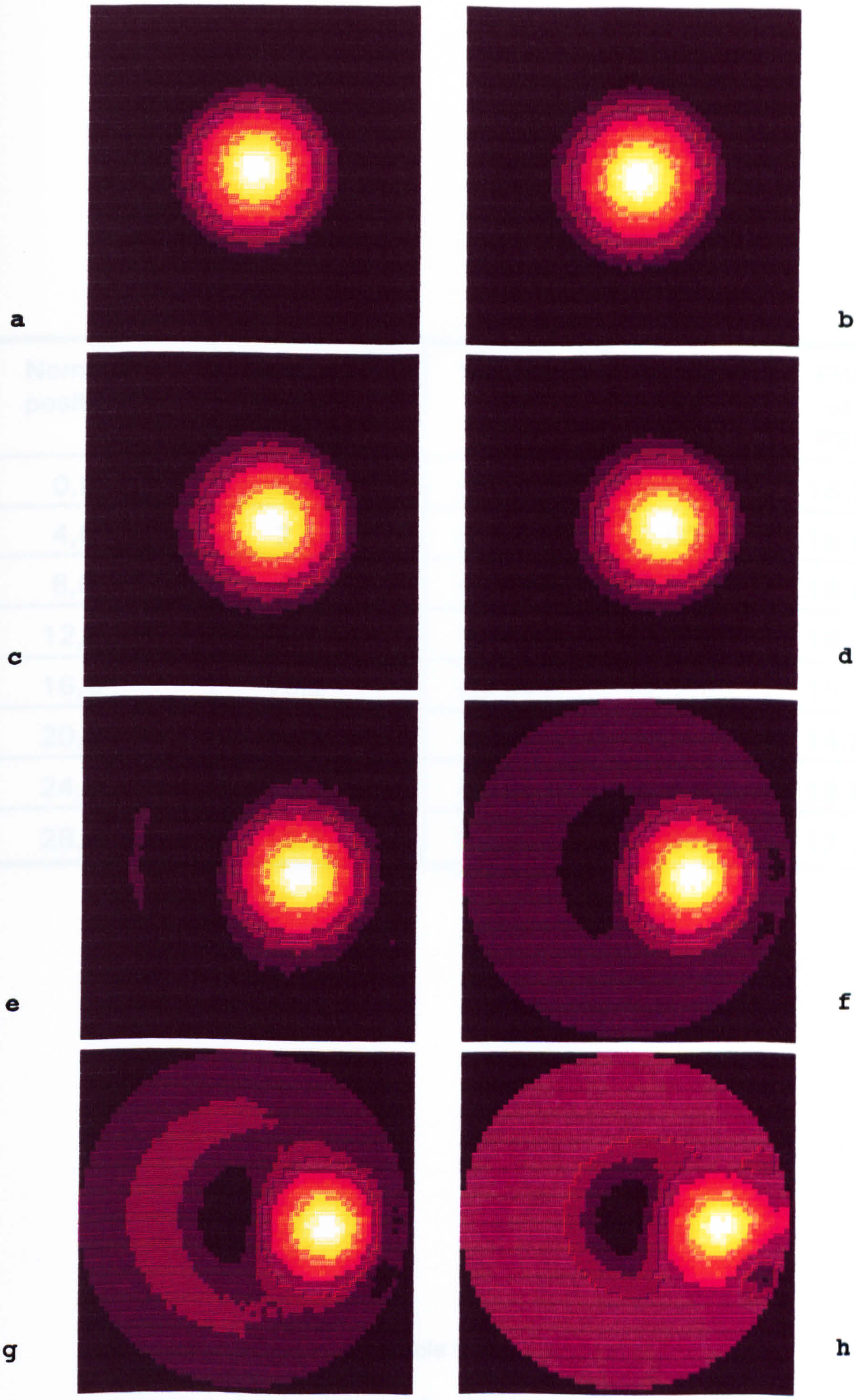

Figure 5.6

A 15mm diameter perspex rod in a 150mm cylindrical tank of saline at positions corresponding to the simulations of figure 4.1. No filtering or position corrections applied.

Nominal position	Reconstructed position	Maximum pixel value	Minimum pixel value	FWHM of PSF
0,0	0,0	0.1127	-0.0012	16.22
4,0	2,1	0.1250	-0.0011	16.61
8,0	4,1	0.1269	-0.0013	16.66
12,0	7,1	0.1310	-0.0018	16.15
16,0	10,2	0.1348	-0.0080	15.31
20,0	12,1	0.1484	-0.0136	14.85
24,0	15,1	0.1925	-0.0203	13.83
28,0	18,2	0.1939	-0.0647	12.23

Table 5.2

Image statistics for the images of an insulating rod at various radial positions in a cylindrical tank shown in figure 5.6. No corrections for PSF blur or position have been applied.

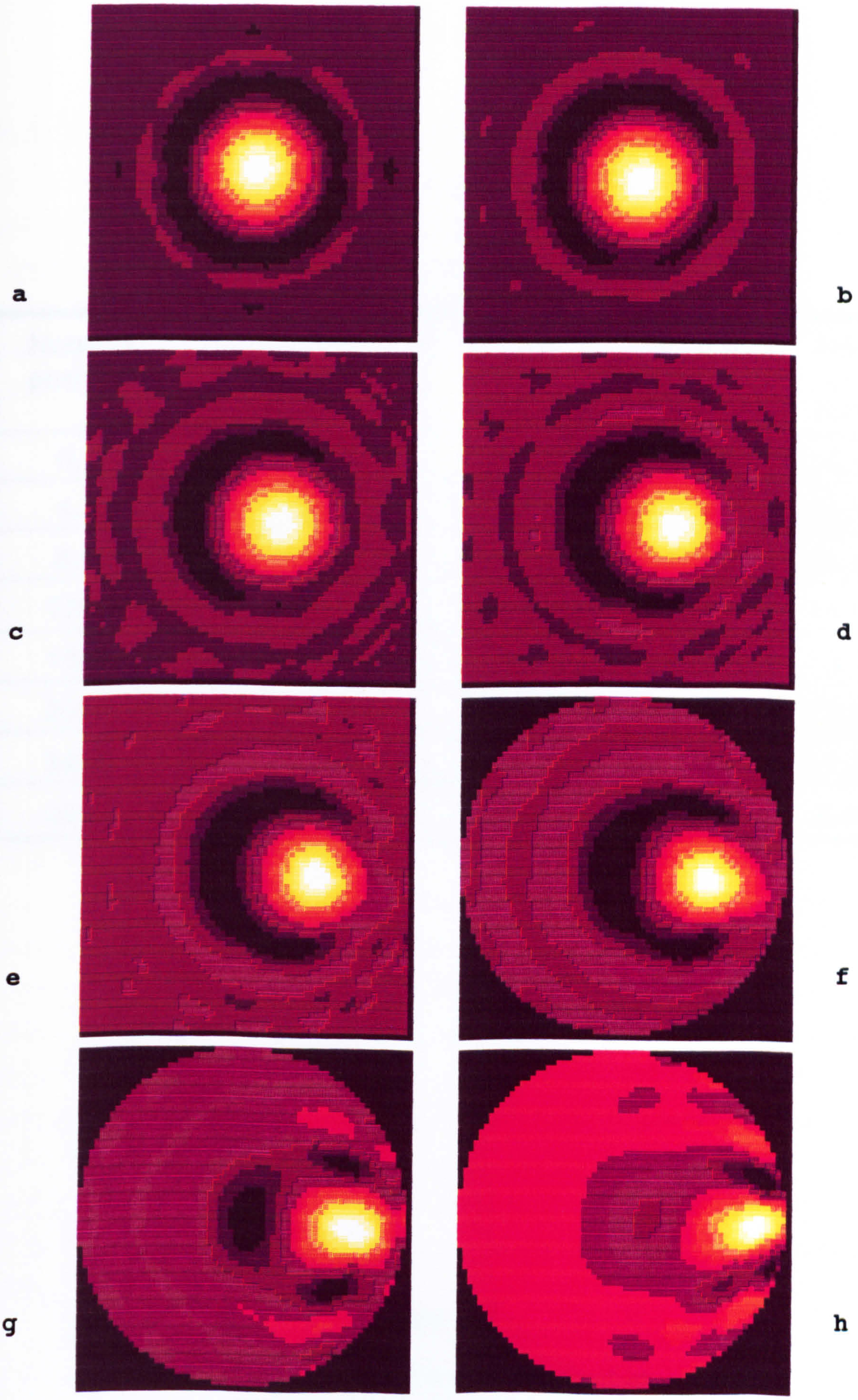

Figure 5.7

A 15mm diameter perspex rod in a 150mm cylindrical tank of saline at the same positions as figure 5.6. Wiener filtering with $\tau = 10^{-5}$ and position correction applied.

Nominal position	Reconstructed position	Maximum pixel value	Minimum pixel value	FWHM of PSF
0,0	0,0	0.2736	-0.0283	15.91
4,0	3,2	0.2847	-0.0326	15.72
8,0	7,2	0.2861	-0.0386	14.86
12,0	10,2	0.2941	-0.0469	14.04
16,0	14,2	0.3025	-0.0621	13.04
20,0	17,3	0.3169	-0.0757	12.62
24,0	21,2	0.3814	-0.1296	11.88
28,0	26,2	0.5853	-0.2951	8.62

Table 5.3

Image statistics for the images of an insulating rod at various radial positions in a cylindrical tank shown in figure 5.7. Corrections for PSF blurring ($\tau = 10^{-5}$) and position have been applied.

5.5 In-vivo chest and reference data sets

One of the requirements of the reconstruction algorithm stated in section 2.4 was that it should be capable of operating with boundary conditions corresponding to the measured external contours of the body section being imaged. To meet this criterion it has been necessary to make geometrical image transformations and PSF corrections dependent on a parameter (S_{norm}) determined by the position of the point of calculation relative to the positions in space of the electrode array rather than an artificial frame of reference. To calculate the potential fields in body section shapes the approximations of section 5.2 have been introduced. To test the validity of this approach, and to assess the performance of the reconstruction algorithm with data taken using electrodes whose size and impedance is not negligible, two sets of in-vivo data were measured by hand.

The data sets were acquired from 16 ECG electrodes encircling the chest of a volunteer male subject at approximately 2 cm below the level of the nipple. The electrodes had an active size of 2 cm x 4 cm and were mounted with their long axes in the superior-inferior direction. The positions of the electrodes in space were determined using a jig mounted in the plane to be imaged. Electrode positions were measured at full inspiration, full expiration and at mean tidal volume. A constant current drive of 1 mA at 20 kHz was multiplexed to the current drive electrodes by hand. Voltage gradient measurements, again multiplexed by hand, were taken using a high input impedance RMS averaging 4½ digit voltmeter (Fluke 8060A, John Fluke Mfg. Co. Inc, Washington, USA). Adjacent electrode current drive and voltage sense configurations were used. Measurements were taken at inspiration and expiration for each electrode combination to produce composite sets of data for inspiration and expiration. The measurement process took some five hours to complete. For comparison, equivalent data collection times for purpose designed EIT data acquisition systems as low as 39 ms have been reported (Sinton et al, 1992).

Alternative quasi-static image reference data sets were generated using the semi-infinite potential field approximation described in section 5.2 in conjunction with the electrode positions measured at inspiration and expiration.

Figure 5.8

Dynamic EIT image of a human chest. The image shows the distribution of change in logarithmic resistivity between inspiration and expiration, and is displayed using the conventional orientation used for x-ray CT i.e looking up from the feet.

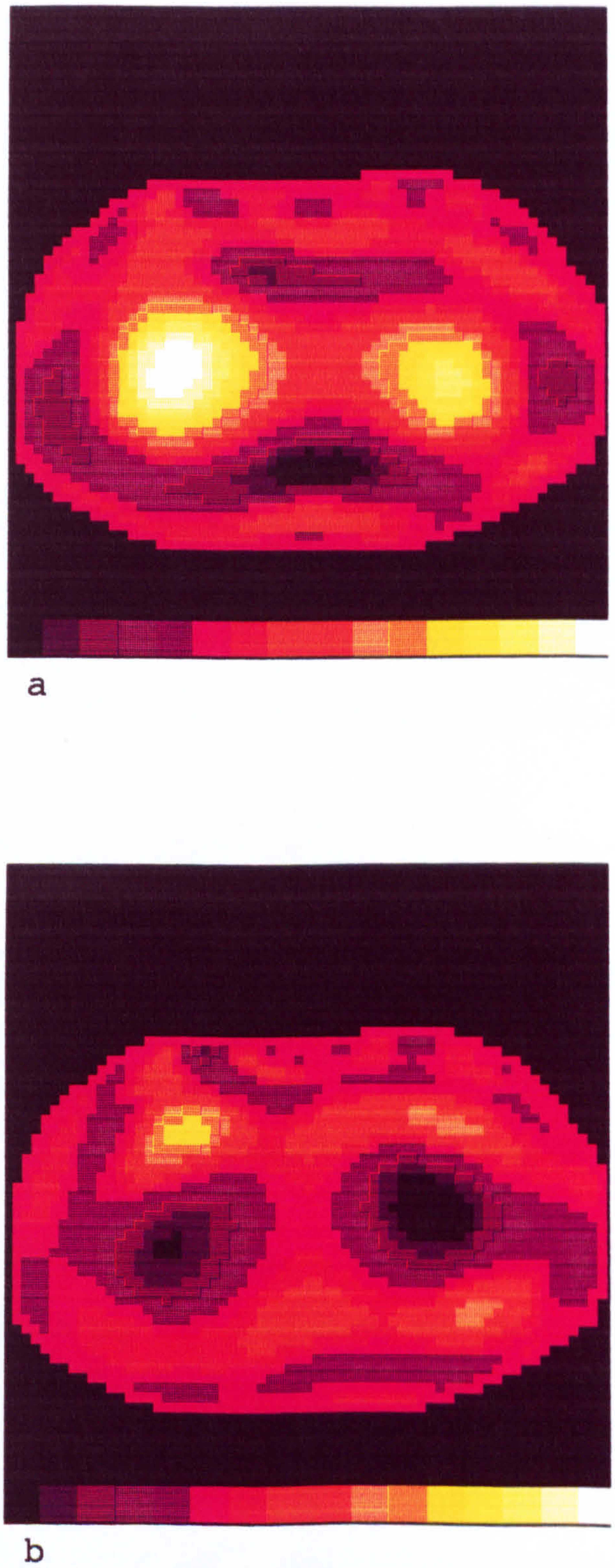

Figure 5.9

Quasi-static EIT images of a human chest at (a) full inspiration and (b) expiration. The images are referenced to a set of homogeneous body data calculated using the potential field approximation of equation 5.3 and the measured positions of the electrodes.

impedance of the lungs at full expiration would be expected to be lower than that at full inspiration, it would still be expected to be greater than that of the surrounding soft tissue. A comparison of the position of the electrode plane used in this experiment with the position of the lungs given in an anatomy text (e.g Tortora and Anagnostakos, 1987) would suggest that the plane was just above the resting level of the diaphragm. A possible explanation for the appearance of figure 5.9b is therefore intrusion into the imaged volume of the diaphragm. No artifacts at the skin surface due to the mis-match between the measured data set (which includes the effect of electrode impedance), and the calculated data set (which assumes zero electrode impedance) are evident. One of the quoted strengths of the dynamic imaging approach is that the unknown electrode impedances for the two data sets cancel out, but the results of figure 5.9 would suggest that the use of the four-electrode measurement technique (section 1.3) can reduce the effects of electrode impedance sufficiently to make feasible quasi-static imaging using calculated reference data sets.

5.8 Summary of chapter 5

In this chapter the image reconstruction algorithm derived and tested in simulation in chapter 4 has been adapted for use with measured data sets. It was found necessary to include the contribution of all sensitivity coefficients when evaluating the quantity S_{norm}, even when not all of the associated measurements are available for use.

A simple model for the approximate calculation of potential fields for body contour boundary conditions has been suggested. The model produced a good fit to FDM generated data for cylindrical boundary conditions over a range of current drive angular spacings. This property was used in a comparison of simulated reconstructions using various current drive electrode spacings. The choice of adjacent electrode current drive was experimentally confirmed as giving the maximum spatial resolution for the noiseless case, especially towards the centre of the image. The flexibility of the weighted backprojection approach with different current drive configurations was also demonstrated.

A series of images of an insulating rod at various positions in a cylindrical tank of saline were successfully reconstructed. The images confirmed the performance of the reconstruction algorithm predicted from the simulations of chapter 4.

Data sets were measured by hand at inspiration and expiration on the chest of a volunteer subject. Dynamic and quasi-static images were reconstructed from these data sets using the measured positions of the electrodes to set the boundary conditions and sensitivity coefficients calculated using the approximate potential field model. The images showed the lungs and the expected impedance changes with respiration. The quasi-static images produced using the calculated reference data sets were not excessively degraded by electrode impedance effects.

CHAPTER 6
CONCLUSIONS

6.0 Introduction

In this work, a reconstruction algorithm for electrical impedance tomography has been developed using a series of three-dimensional computer simulations, and tested on physical phantom and in-vivo data. The algorithm was designed to fulfil a set of specifications thought useful to advance the utility of EIT as a clinical imaging modality, whilst remaining practicable in terms of computational effort. The resulting algorithm is distinguished from other published approaches by its ability to meet these specifications.

6.1 Summary of key results

In section 2.4 a set of specifications for an EIT reconstruction algorithm was suggested. The performance of the reconstruction algorithm developed in this work can now be reviewed in terms of this set of specifications:

1) The algorithm should produce dynamic images. Reconstructions of simulated, physical phantom and in-vivo dynamic data sets have been carried out.

2) The algorithm should be non-iterative. This requirement was thought necessary to limit the amount of computational effort required. To operate in this manner it was necessary to make the assumption that the current density distribution within the object is the same as that for an object of the same dimensions but exhibiting a homogeneous resistivity. This assumption results in overshoot artifacts where large changes of resistivity are being imaged, but this would be expected. The present algorithm has been shown to produce useful images using a non-iterative approach.

3) The algorithm should be defined in three dimensions. The simulated, phantom and in-vivo data used during the development of the algorithm has all been produced using three-dimensional resistivity change distributions. For simplicity, the assumption of cross-sectional uniformity has been made for the most part, this assumption being used to approximate the effects of out-of-plane current flow in the in-vivo case. An experimental investigation of the out-of-plane spread function indicated that it is of a near Gaussian form and that its width can be related to the parameter S_{norm} calculated during the reconstruction.

4) **The algorithm should be capable of employing boundary conditions corresponding to measured body cross-sections.** An important finding from this work is that, not only is the point spread function in the image plane of a near Gaussian form when transformed to an equi-resolution space, but that the required geometrical transformation can be related to a parameter, S_{norm}, which is calculated during the reconstruction process. The spatial filtering step is therefore not dependent on an unrealistic fixed geometry, but can be carried out for body shaped contours also. In vivo images of a chest section have been produced using measured electrode position to provide the boundary reference points.

5) **The algorithm should be capable of employing a range of current drive configurations.** Simulated reconstructions with a range of current drive electrode spacings have been carried out using the basic backprojection algorithm. Further analysis of the point spread functions produced would be required to implement the full algorithm, including filtering, for these current drive configurations, but it would be expected that the same basic relationships with S_{norm} used for the adjacent electrode case would hold. For noiseless simulated data, adjacent electrode current drive was found to produce the best spatial resolution especially towards the centre of the image.

6) **The algorithm should be capable of operating on an image matrix containing a larger number of elements than there are independent measurements in the data set.** All the reconstructions performed have been performed on a finer matrix that would be allowed by the number of independent measurements in the data set. This approach has allowed a more accurate examination of the point spread functions than would otherwise have been possible.

The reconstruction algorithm developed requires a calculation of the three dimensional potential distributions produced by the current drive and voltage sense electrode pairs within the bounded volume defined by the electrode positions. This requirement might be expected to add significantly to the computing requirements and/or reconstruction time, however the use of a simple approximate model for the calculation of these potential distributions has been shown to produce encouraging results on a real body contour.

6.2 Directions for future development

A number of directions for future development aimed at achieving a practical implementation of the image reconstruction approach described in the present work can be identified. Improvements would seem feasible both in speed, and in the accuracy of some of the approximations used.

In general, apart from the decision to concentrate on a single-pass algorithm, no effort has been made to optimise the algorithm for speed. This could be achieved by reducing the number of pixels reconstructed in each slice and by more efficient ordering of calculations, especially in the evaluation of the sensitivity coefficients where the potential field model could be implemented as an interpolation from a stored field instead of point-by-point calculations.

A simple semi-infinite potential field model has been shown to be useful both in the calculation of the sensitivity coefficients and as a source of approximate reference data for quasi-static imaging. Further work on this model and its possible combination with the conventional finite differences approach could increase its value.

The spatial transformation required to implement the spatial filtering and position correction steps are presently based on a circular geometry with a central reference point. Further analysis of this transformation problem could lead to the development of a transformation less dependent on this geometry.

Although out-of-plane resolution has been investigated, a lack of true multi-plane data sets has prevented further progress on spatial filtering in the axial direction. The measurement of such a data set, and in general the measurement of other in-vivo data sets would be an obvious next step. A more distant goal would be the development of a clinically applicable multi-plane data acquisition system.

6.3 Conclusion

Although electrical impedance tomography has been under development for a decade, the clinical application of this new imaging modality is not widespread. No consensus on a recognised optimal reconstruction algorithm has emerged because, although the symbolic definition of the reconstruction problem can be fairly simple, the implementation of a reconstruction algorithm requires a compromise between the specification of the algorithm (and hence the number of assumptions permissable) and the computational effort required to execute it. In this work, an algorithm has been developed to a set of specifications (including three-dimensionality, the ability to handle body contour boundary shapes, and single-pass execution) which represent an extension to existing techniques, whilst remaining feasible with current technology. The algorithm has been shown to perform successfully within the limitations imposed by the assumptions on which it based. It is hoped that this work may extend the capabilities of EIT and eventually lead to its increased use in clinical diagnosis.

REFERENCES

Barber D C 1989a A review of image reconstruction techniques for electrical impedance tomography. Med. Phys. 16(2) 162-69

- 1989b A sensitivity method for electrical impedance tomography (letter). Clin. Phys. Physiol Meas. 10 368-70

- 1990 Quantitation in impedance imaging. Clin. Phys. Physiol. Meas. 11 suppl. A 1-12

Barber D C and Brown B H 1984 Applied potential tomography. (review article) J. Phys. E: Sci. Instrum. 17 723-33

- 1986 Recent developments in applied potential tomography. Information Processing in Medical Imaging. ed. S Bacharach (Dordrecht: Nartinus Nijhoff) pp 106-21

- 1988 Errors in reconstruction of resistivity images using a linear reconstruction technique Clin. Phys. Physiol. Meas. 9 suppl. A 101-4

- 1990 Reconstruction of impedance images using filtered backprojection. Proc. 3rd European Community Workshop on Electrical Impedance Tomography pp 1-8

Barber D C, Brown B H and Freeston I L 1983 Imaging spatial distributions of resistivity using applied potential tomography. Electron. Lett. 19 933-35

Barber D C and Seagar A D 1987 Fast reconstruction of resistance images. Clin. Phys. Physiol. Meas. 8 suppl. A 47-54

Barrett H H and Swindell W 1981 Radiological imaging. (Academic Press, London)

Bates R H T, McKinnon G C and Seagar A D 1980 A limitation on systems for imaging electrical conductivity distributions. IEEE Trans. Biomed. Eng. 27 418-20

Breckon W R and Pidcock M K Mathematical aspects of impedance imaging. Clin. Phys. Physiol. Meas. 8 suppl. A 77-84

British Standards Institution 1989. BS5724 Part 1 Medical electrical equipment. (British Standards Institution, London)

Brown B H 1990 Overview of clinical applications. Proc. 3rd European Community Workshop on Electrical Impedance Tomography pp 29-35

Brown B H, Barber D C and Seagar A D 1985 Applied potential tomography: possible clinical applications. Clin. Phys. Physiol. Meas. 6 109-21

Brown B H and Seagar A D 1987 The Sheffield data collection system. Clin. Phys. Physiol. Meas. 8 suppl. A 91-7

Brown B H, Leathard A, Sinton A, McArdle F J, Smith R W M and Barber D C 1992 Blood flow imaging using electrical impedance tomography. Clin. Phys. Physiol. Meas. 13 suppl. A 175-9

Cheney M and Isaacson D 1992 Distinguishability in impedance imaging. IEEE Trans. Biomed. Eng. BME-39 852-60

Conway J 1987 Electrical impedance tomography for thermal monitoring of hyperthermia treatment: an assessment using in vitro and in vivo measurements. Clin. Phys. Physiol. Meas. 8 suppl. A 141-6

Conway J, Hawley M, Mangnall Y, Amasha H and van Rhoon G C 1992 Experimental assessment of electrical impedance imaging for hyperthermia monitoring. Clin. Phys. Physiol. Meas. 13 suppl. A 185-9

Cooley J W and Tukey J N 1965 An algorithm for the machine calculation of complex Fourier series. Math. Comput. 19 297-301

Dines K A and Lytle R J 1981 Analysis of electrical conductivity imaging. Geophysics 46 1025-36

Evans D F and Wright J W 1990 Is acid suppression neccessary when measuring gastric empying using applied potential tomography? Proc. 3rd European Community Workshop on Electrical Impedance Tomography pp 249-55

Eyuboglu B M, Brown B H, Barber D C and Seagar A D 1987 Localisation of cardiac related impedance changes in the thorax. Clin. Phys. Physiol. Meas. 8 suppl. A 167-73

Eyuboglu B M and Brown B H 1988 Methods of cardiac gating applied potential tomography. Clin Phys Physiol. Meas. 9 suppl. A 43-8

Ferrari R L 1975 An introduction to electromagnetic fields. (Van Nostrand Reinhold, Wokingham, Berks.)

Frewer R 1972 The effect of frequency changes on the electrical conductance of moving and stationary blood. Med. & Biol. Eng. 10 734-41

Fricke H and Morse S 1926 The electric capacity of tumours of the breast. J. Cancer. Res. 10 340-76

Fujita S, Udea T and Yagi M 1972 Detection of experimental and clinical brain edema using an electrical impedance method. J. Neurosurg. 37 156-63

Gadd R, Record P and Rolfe P 1992. A sensitivity region reconstruction algorithm using adjacent drive current injection strategy. Clin. Phys. Physiol. Meas. 13 suppl. A 101-5

Geddes L and Baker L E 1967 The specific resistance of biological material - a compendium of data for the biomedical engineer and physiologist. Med. Bio. Eng. 5 271-93

Geddes L and Baker L E 1975 Principles of Applied Biomedical Instrumentation, 2nd edition (Wiley-Interscience)

Gençer N G, İder Y Z and Kuzuoğlu 1992 Electrical impedance tomography using induced and injected currents Clin. Phys. Physiol. Meas. 13 suppl. A 95-9

Gershing E, Preusse C J, Gebhard M M, Ulbricht L J and Bretschneider H J 1983 The electric impedance as indicator of myocardial ischemeic stress. Proc. 6th Int. Conf. on Electrical Bio-impedance (ICEBI), Zadar, Yugoslavia

Geselowitz D B 1971 An application of electrocardiographic lead theory to impedance plethysmography. IEEE Trans. Biomed. Eng. BME-18 38-41

Ghahary A 1990 Electrical safety. In: Electrical Impedance Tomography. ed. Webster J G. (Adam Hilger, Bristol) pp 58-69

Gisser D G, Isaacson D and Newell J C 1987 Current topics in impedance imaging. Clin. Phys. Physiol. Meas. 8 suppl. A 39-46

-1988 Theory and performance of an adaptive current tomography system Clin. Phys. Physiol. Meas. 9 suppl. A 35-41

Griffiths H Ahmed A 1987 Applied potential tomography for non-invasive temperature mapping in hyperthermia. Clin. Phys. Physiol. Meas. 8 suppl. A 147-53

Harris N D, Suggett A J, Barber D C and Brown B H 1987 Applications of applied potential tomography (APT) in respiratory medicine. Clin. Phys. Pysiol. Meas. 8 suppl. A 155-65

Henderson R P and Webster J G 1978 An impedance camera for spatially specific measurements of the thorax. IEEE Trans. Biomed. Eng. BME-27 250-4

Hill D W and Thompson F D 1975 The effect of haematocrit on the resistivity of human blood at 37°c and 100kHz. Med. Biol. Eng. 13 182-6

Holder D S and Gardner-Medwin A R 1988 Some possible neurological applications of applied potential tomography. Clin. Phys. Physiol. Meas. 9 suppl. A 111-9

Hounsfield G N 1973 Computerised transverse axial scanning (tomography) Part 1: Description of system. Brit. J. Radiol. 46 1016-22

Hua P, Webster J G and Tomkins W J 1987 Effect of the measurement method on noise handling and image quality of EIT imaging. Proc. Annual Int. Conf. IEEE Engineering in Medicine Society 9 1429-30

Hua P and Woo E J 1990 Reconstruction algorithms. In: Electrical Impedance Tomography. ed. Webster J G. (Adam Hilger, Bristol) pp 97-137

Isaacson D, Cheney M and Newell J C 1990 Comments on reconstruction algorithms. Clin Phys. Physiol. Meas. 13 suppl. A 83-9

Jossinet J and Kardous G 1987 Physical study of the sensitivity distribution in multi-electrode systems. Clin. Phys. Physiol. Meas. 8 suppl. A 33-7

Jossinet J 1988 A hardware design for imaging the electrical impedance of the breast Clin. Phys. Physiol. Meas. 9 suppl. A 25-8

Jossinet J, Forcade C and Schmitt M 1981 A study for breast imaging with a circular array of impedance electrodes. Proc. 5th Int. Conf. on Electrical Bioimpedance (ICEBI), Tokyo, pp 83-6

Kiber M A, Barber D C and Brown B H 1990 Estimation of object boundary shape from the voltage gradient measurements. Proc. 3rd European Community Workshop on Electrical Impedance Tomography pp 52-7

Kim Y, Tompkins W J and Webster J G 1983 Electrical impedance imaging of the body with non-linear reconstruction. Proc. Society of Photo-Optical Instrumentation Engineers (SPIE), Atlanta, Georgia pp 289-96

Kim Y and Woo H W 1987 A prototype system and reconstruction algorithms for electrical impedance technique in medical body imaging. Clin. Phys. Physiol. Meas. 8 suppl. A 63-70

Kotre C J 1988 A fast approximation for the calculation of potential distributions in electrical impedance tomography. Clin. Phys. Physiol. Meas. 9 353-61

-1989a A sensitivity coefficient method for the reconstruction of electrical impedance tomograms. Clin. Phys. Physiol. Meas. 10 275-81

-1989b Comment on the alternative reconstruction algorithm for electrical impedance tomography (letter). Clin. Phys. Physiol. Meas. 10 370-71

Kulkarni V, Hutchison J M S, Ritchie I K and Mallard J R 1990 Impedance imaging in upper arm fractures. J Biomed. Eng. 12 219-27

Lamont G L, Wright J W, Evans D F and Kapila L 1988 An evaluation of applied potential tomography in the diagnosis of infantile hypertrophic pyloric stenosis. Clin. Phys. Physiol. Meas. 9 suppl. A 65-9

Lauterbur P C 1973 Image formation by induced local interactions: examples employing nuclear magnetic resonance. Nature 242 190-1

Lehr J 1972 A vector derivation useful in impedance plethysmography field calculations. IEEE Trans. Biomed. Eng. BME-19 156-7

Lindley E J, Brown B H, Barber D C, Grundy D, Knowles R, McArdle F J and Wilson A J 1992 Monitoring body fluid distribution in microgravity using impedance tomography (APT) Clin. Phys. Physiol. Meas. 13 suppl. A 181-4

Liu P, Griffiths H, Wiles C M, Nathadwarawala K M and Stewart W 1992 Measurement of pharyngeal transit time by electrical impedance tomography Clin. Phys. Physiol. Meas. 13 suppl. A 197-200

Liu W P, Hau P and Webster J G 1988 Three-dimensional reconstruction in electrical impedance tomography. Clin. Phys. Physiol. Meas. 9 suppl. A 131-5

McArdle F J, Suggett A J, Brown B H and Barber D C 1988 An assessment of dynamic images by applied potential tomography for monitoring pulmonary perfusion Clin. Phys. Physiol. Meas. 9 suppl. A 87-91

McCleod C N, Breckon W R and Murphy D 1990 OXPACT- The development of an adaptive current tomograph. Proc. 3rd European Community Workshop on Electrical Impedance Tomography pp 191-5

Man B, Sollish B D, Moshitzky M, Choukron Y and Frei E H 1979 Results of preclinical tests for breast cancer detection by dielectric measurements. Proc. XII Int. Conf. on Medical & Biological Engineering, Jerusalem, Israel 30.4

Mangnall Y F, Baxter A J, Avill R, Bird N C, Brown B H, Barber D C, Seagar A D, Johnson A G and Read N W 1987 Applied potential tomography: a new non-invasive technique for assessing gastric function. Clin. Phys. Physiol. Meas. 8 suppl. A 119-29

Mangnall Y F, Barnish C, Brown B H, Barber D C, Johnson A G and Read N W 1988 Comparison of applied potential tomography and impedance epigastrography as methods of measuring gastric emptying. Clin. Phys. Physiol. Meas. 9 249-54

Murai T and Kagawa Y 1985 Electrical impedance computed tomography based on a finite element model. IEEE Trans. Biomed. Eng. BME-32 177-84

Murphy D, Burton P, Coombs R, Tarassenko L and Rolfe P 1987 Impedance imaging in the newborn. Clin. Phys. Pysiol. Meas. 8 suppl. A 131-40

Murphy D and Rolfe P 1988 Aspects of instrumentation design for impedance imaging. Clin. Phys. Physiol. Meas. 9 suppl. A 5-14

Nakayama K, Yagi W and Yagi S 1981 Fundamental study on electrical impedance CT algorithm utilizing sensitivity theorem on impedance plethysmography. Proc. 5th Int. Conf. on Electrical Bio-impedance (ICEBI) Tokyo pp 99-102

Patel A 1990 Data collection methods. In: Electrical Impedance Tomography. ed. Webster J G. (Adam Hilger, Bristol) pp 75-86

Persson B R R, Blad B and Weber L 1990 The use of electrical impedance tomography for non-invasive temperature monitoring in hyperthermia treatment of cancer. Proc. 3rd European Community Workshop on Electrical Impedance Tomography pp 263-9

Pethig R 1984 Dielectric properties of biological materials: biophysical and medical applications. IEEE Trans. Electr. Insul. 19 453-74

Price L R 1979a Electrical impedance computed tomography (ICT): a new imaging technique. IEEE Trans. Nucl. Sci. NS-26 2736-9

\- 1979b Imaging of the electrical conductivity and permittivity inside a patient: a new computed tomography (CT) technique. Proceedings of the Society of Photo-optical Engineers SPIE Vol. 206 Recent and Future Developments in Medical Imaging II 115-9

Purvis W R, Tozer R C and Freeston I L Impedance imaging using induced currents. Proc. Annual Conf. IEEE Engineering in Medicine & Biology Society 12 114-5

Rabbat A 1990 Tissue resistivity In: Electrical Impedance Tomography. ed. Webster J G. (Adam Hilger, Bristol) pp 8-20

Rabbani K S and Kabir A M B H 1991 Studies on the effect of the third dimension on a two-dimensional electrical impedance tomography system. Clin. Phys. Physiol. Meas. 12 393-402

Ritchie I K and Kulkarni V 1990 Impedance osteography: clinical applications of a new method of imaging fractures. J. Biomed. Eng. 12 369-74

Rush S, Abildskov J A and McFee R 1963 Resistivity of body tissues at low frequencies. Circ. Res. 12 40-50

Sakamoto K and Kanai H 1983 A fundamental study of an electrical impedance CT algorithm. Proc. 6th Int. Conf. on Electrical Bio-impedance (ICEBI), Zadar, Yugoslavia pp 349-52

Sakamoto K Yorkey T J and Webster J G 1987 Some physical results from an impedance camera. Clin. Phys. Physiol. Meas. 8 suppl. A 71-6

Scaife J M, Tozer R C and Freeston I L 1990. Real and imaginary impedance imaging using induced currents. Proc. Annual Conf. IEEE Engineering in Medicine & Biology Society 12 116-7

Schwan H P 1957 Electrical properties of tissue and cell suspensions. Adv. Biol. Med. Phys. 5 147-209

Seagar A D, Barber D C and Brown B H 1987a Theoretical limits to sensitivity and resolution in impedance imaging. Clin. Phys. Physiol. Meas. 8 suppl. A 13-31

\- 1987b Electrical impedance imaging. IEE Proc. Pt. A 134 201-10

Silva F, Rosell J and Pallàs F 1990 Averaging method for cardiac gated images using transthoracic impedance. Proc. 3rd European Community Workshop on Electrical Impedance Tomography pp 60-70

Singh B, Smith C W and Hughes R 1979 In vivo dielectric spectrometer. Med. & Biol. Eng. & Comput. 45-60

Sinton A M, Brown B H, Barber D C, McArdle F J and Leathard A D 1992 Noise and spatial resolution of a real-time electrical impedance tomograph. Clin. Phys. Physiol. Meas. 13 suppl. A 25-30

Skidmore R, Evans J M, Jenkins D and Wells P N T 1987 Data collection for impedance measurements from the human breast. Clin. Phys. Physiol. Meas. 8 suppl. A 99-102

Smith D N 1985 Determination of impedances using numerous simultaneous currents (DINSC) - system design and practical applications. Proc. IEE Int. Conf. on Electric and Magnetic Fields in Medicine and Biology, London pp 69-73

Smith R W M, Brown B H, Freeston I L and McArdle F J 1990 Real time electrical impedance tomography. Proc. 3rd European Community Workshop on Electrical Impedance Tomography pp 212-6

Sollish B D, Drier Y, Hammerman E, Moshitzky M, Frei E H and Man B 1979 A dielectric breast scanner. Proc. XII Int. Conf. on Medical & Biological Engineering, Jerusalem, Israel 30.3

Sollish B D, Frei E H, Hammerman E, Lang S B and Moshitzky M 1981 Microprocessor assisted screening techniques. Isr. J. Med. Sci. 17 859-64

Surowiec A, Stuchly S S and Swarup A, 1985 Radiofrequency dielectric properties of animal tissues as a function of time following death. Phys. Med. Biol. 30 1131-41

Tarassenko L and Rolfe P 1984 Imaging spatial distributions of resistivity - an alternative approach. Electron. Lett. 20 574-6

Tarassenko L, Pidcock M K, Murphy D F and Rolfe P 1985 The development of impedance imaging techniques for use in the newborn at risk of intraventricular haemorrhage. IEE Int. Conf. on Electric and Magnetic Fields in Medicine and Biology, London pp 83-7

Thomas D C, McArdle F J, Rogers V E, Beard R W and Brown B H 1991 Local blood volume changes in women with pelvic conjestion measured by applied potential tomography. Clin. Sci. 81 401-4

Tortura G J and Anagnostakos N P 1987 Principles of anatomy and physiology, 5th edn. (Harper & Row, New York)

Webb S 1988 The physics of medical imaging. (Adam Hilger, Bristol)

Wexler A 1988 Electrical impedance imaging in two and three dimensions. Clin. Phys. Physiol. Meas. 9 suppl. A 29-33

Witsoe D A and Kinnen E 1967 Electrical resistivity of lung at 100 kHz. Med. Biol. Eng. 5 239-48

Woo J W 1990 Computational complexity In: Electrical Impedance Tomography. ed. Webster J G. (Adam Hilger, Bristol) pp 138-57

Wright J W and Evans D F 1990 Applied potential tomography (APT): A non-invasive method of detecting the migrating motor complex (MMC). Proc. 3rd European Community Workshop on Electrical Impedance Tomography pp 270-5

Yorkey T J , Webster J G and Tompkins W J 1986 An optimal impedance tomographic reconstruction algorithm. Proc. 8th Annual Conf. IEEE Eng. Biol. Soc. 339-42

Yorkey T J and Webster J G 1987 A comparison of impedance tomography reconstruction algorithms. Clin. Phys. Pysiol. Meas. 8 suppl. A 55-62

Zadehkoochak M, Hames T K, Blott B H and George R F 1990. A transputer implemented algorithm for electrical impedance tomography. Clin. Phys. Physiol. Meas. 11 223-30

Zadehkoochak M, Blott B H, Hames T H and George R F 1992 Pulmonary perfusion and ventricular ejection imaging by frequency domain filtering of EIT images. Clin. Phys. Physiol. Meas. 13 suppl. A 191-6

Zhang Z and Griffiths H 1990 Dual-frequency electrical impedance tomography of the forearm. Proc. 3rd European Community Workshop on Electrical Impedance Tomography pp 256-62

Zheng E, Shau S and Webster J G 1984 Impedance of skeletal muscle from 1 Hz to 1 MHz. IEEE Trans. Biomed. Eng. BME-31 477-81